FABRICATION, CHARACTERIZATION AND MODELING OF K_{31} PIEZOELECTRIC MICROMACHINED ULTRASONIC TRANSDUCERS (pMUTs)

By

HONGSOO CHOI

A dissertation submitted in partial fulfillment of
the requirements for the degree of

DOCTOR OF PHILOSOPHY

WASHINGTON STATE UNIVERSITY
School of Mechanical and Materials Engineering

DECEMBER 2007

To the Faculty of Washington State University:

The members of the Committee appointed to examine the dissertation of HONGSOO CHOI find it satisfactory and recommend that it be accepted.

Co-Chair

Co-Chair

ACKNOWLEDGEMENT

I would like to sincerely and gratefully thank my committee for their guidance, encouragement, patience, and generous advice based on their areas of expertise during my graduate work. Special thanks to my co-advisors, Dr. Jow-Lian Ding and Dr. Amit Bandyopadhyay. Dr. Ding's guidance encouraged me to accomplish the modeling and theoretical parts of my graduate work. I still remember how much I struggled to develop the Finite Element code, and I appreciate his patience and incitation. Dr. Bandyopadhyay always inspired me in my graduate work, and his financial support is gratefully appreciated. His critical view of my work made it possible to overcome many obstacles in my experimental work, and it would have taken much more time to accomplish my work without his perspective. I am grateful for having both of them as my co-advisors because I learned not only the scholarly work but also the way of life. I hope they will be my lifetime advisors, and their impact during my graduate work will positively affect my life.

I would like to thank Dr. Susmita Bose for her invaluable support and continuous suggestions for fabrication. Her guidance and training were very effective and made it possible to move my research from chemical synthesis to sample fabrication. Dr. Bose gave me tremendous motivation and ideas whenever I struggled with my experiment, and I learned how to be an engineer who can effectively approach and solve complex engineering challenges.

I would also like to thank Dr. Michael Anderson, at the University of Idaho, for sharing his extensive knowledge on acoustics and ultrasound transducers. He especially inspired me in the development of analytical solutions for micro-ultrasound transducers. His helpful comments and valuable suggestions delighted me many times and made me think creatively.

I thank Dr. John Fraser at Philips Medical Systems for his generous and extensive guidance. Much of my inspiration came from the technical discussions with Dr. Fraser by phone or email. I appreciate the professors and staff in the School of Mechanical and Materials Engineering at Washington State University. They made it possible to finish my graduate work here in Pullman. I thank my group members for their sincere help and friendship. I also thank all my friends I made at Washington State University for their warm friendship. I am fortunate; I have too many friends to list all their names.

I especially thank my parents, Mr. Yonghwan Choi (in heaven) and Ms. Jumsun Kim for their endless love, patience, encouragement. Without their blessings and sacrifices, I would not have made it to this stage. My gratitude goes to Dr. Eunjung Kim, a woman who has unlimited love and patience for me. Without her endless support and love, my life in Pullman would not have been as smooth as it was. There are no words that can express my appreciation for my daughter, Sophia Choi. Sophia brought us infinite happiness and made us smile even when both of us were busy with our graduate work. I would also like to thank my brother, sisters, brothers-in-law, sister-in-law, nephews, and nieces for their emotional support.

FABRICATION, CHARACTERIZATION AND MODELING OF K_{31} PIEZOELECTRIC MICROCACHINED ULTRASONIC TRANSDUCERS (pMUTs)

Abstract

by Hongsoo Choi, Ph.D.
Washington State University
December 2007

Co-Chairs: Jow-Lian Ding and Amit Bandyopadhyay

Piezoelectric Micromachined Ultrasonic Transducers (pMUTs) offer a new approach for developing two dimensional array type ultrasonic transducers for real-time, three dimensional medical imaging. The studies reported in this dissertation represent part of the efforts towards this goal and consists four major tasks, namely, fabrication, characterization, analyzing and modeling of single element transducers, and development of a prototype of 2D array type transducer. The transducer belongs to K_{31} type in which a flexural vibration of the membrane is excited by a voltage applied in a direction that is normal to the surface of the membrane. The specific objectives of this study are to develop the fabrication technology for pMUTs and understand their behavior and performance through both experimental characterization and analytical and numerical modeling.

The pMUTs were fabricated using MEMS technology. There characteristics were measured by impedance measurement combined with equivalent circuit analysis. For the analytical prediction of pMUT performance, a one dimensional composite beam and a two dimensional composite plate model were developed. For the numerical prediction, a finite

element code based on a combination of the equivalent single-layer theory and the classical laminated plate theory (CLPT) using a rectangular conforming plate element.

The majority of the pMUTs fabricated in this study has a large length to width aspect ratio. For this type of pMUTs, it was found that the resonant frequencies decreased from 2MHz to 600KHz as the widths of the membrane increased from 90μm to 180μm, but showed no appreciable length dependence. Effective coupling coefficients (k_{eff}^2) was found to increase with width up to 150μm and then decrease. The peak value of k_{eff}^2 was found to be around 0.826%.

The measured resonance frequencies matched quite well with finite element calculations and analytical models. Based on the prediction of the 2D composite plate model, both the membrane size and electrode coverage have significant influence on k_{eff}^2 . The maximum predicted k_{eff}^2 was 2.908% which occurred when the electrode covered about 48.9% in both x and y directions for a square membrane, or about 23.9% of the membrane area covered from the center of the membrane.

Table of Contents

ACKNOWLEDGEMENT ... iii
Abstract ... v
List of Figures ... x
List of Tables ... xiii
List of Symbols and Abbreviations ... xiv
1 Introduction ... 1
  1.1 Medical Imaging Systems ... 1
  1.2 Medical Imaging Using Ultrasound ... 2
  1.3 Ultrasound Transducers ... 8
  1.4 Motivations ... 14
  1.5 Research Objectives ... 16
2 PZT Based MEMS Devices ... 18
  2.1 Piezoelectricity ... 18
    2.1.1 PZT Thin Film Deposition ... 20
    2.1.2 Sol-Gel Method ... 21
  2.2 Micromachined Ultrasonic Transducers ... 22
    2.2.1 Microelectromechanical Systems (MEMS) ... 24
    2.2.2 Capacitive Micromachined Ultrasonic Transducers ... 26
    2.2.3 Piezoelectric Micromachined Ultrasonic Transducers ... 28
  2.3 Numerical Tools for MEMS ... 30
3 Fabrication of pMUTs ... 31
  3.1 Silicon Wafer as a MEMS Substrate ... 31
  3.2 Furnace Processes ... 33
    3.2.1 High Temperature Oxidation ... 33
    3.2.2 Boron Diffusion ... 33
    3.2.3 Low Temperature Oxidation ... 34
  3.3 Membrane Fabrication ... 35
    3.3.1 Backside Mask Design and Photolithography ... 35
    3.3.2 Anisotropic Silicon Etching ... 36

3.4 Thin Film Deposition 38
3.4.1 Sputtering for Bottom Electrode 38
3.4.2 PZT Thin Film Deposition 39
3.4.3 Sputtering for Top Electrode 40
3.5 Patterning Top Electrode and PZT film 41
4 Characterization of pMUTs 43
4.1 Ferroelectric Measurement 43
4.2 Electrical Impedance Measurement 46
4.2.1 Impedance Measurement and Equivalent Circuit Analysis 46
4.2.2 Fabricated pMUTs Samples 51
4.2.3 Results 53
4.3 Characterization of Array Type pMUTs 61
4.4 Conclusions 65
5 Finite Element Method for pMUTs 67
5.1 Introduction 67
5.2 Finite Element Formulation for Laminated Composite Plate 68
5.3 Validation of FE Model 76
5.4 Comparison of FEA and Experimental Results 78
5.5 Discussion 82
5.6 Conclusions 84
6 One Dimensional Analytical Solution for pMUTs 86
6.1 Introduction 86
6.2 1D Composite Beam Model and Its Correlation with the Equivalent Circuit 87
6.3 First Order Analysis Based on the One-Dimensional Model 96
6.4 Quantitative Prediction of pMUT Performance Based on the Beam Model 98
6.5 Effects of Residual Stress 106
6.6 Discussion 109
6.7 Conclusions 110
7 Two Dimensional Analytical Solution for pMUTs 111
7.1 Introduction 111
7.2 2D Composite Plate Model 111
7.3 Prediction of pMUTs Performance Based on 2D Plate Model 119

7.4 Optimization of Design Parameters Using Two-Dimensional Model 124
7.5 Development of Graphical User Interface 128
7.6 Conclusions 130
8 Conclusions and Recommendations 132
8.1 Conclusions 132
8.2 Recommendations 133
8.2.1 Recommendations for Experimental Work 133
8.2.2 Recommendations for Modeling Work 136
References 138

List of Figures

Figure 1-1: 2D (left) and 3D (right) ultrasound images of a third-trimester fetus [8]. 4
Figure 1-2: Axial slice of 3D ultrasound (left) and corresponding MRI (right) images of infant heart [9]. 5
Figure 1-3: Three cross sectional images (a) from a volumetric 3D image of abdomen of a seven month fetus [10]. 7
Figure 1-4: A piston type single element ultrasonic transducer [15]. 9
Figure 1-5: Frequency VS. amplitude for a typical resonant system. 11
Figure 1-6: Reflected and transmitted waves of normal incident wave at an interface between two materials [14]. 13
Figure 1-7: Beam profile of a single element piston transducer [3]. 14
Figure 2-1: Piezoelectric elementary cell; (a): before poling, (b): after poling [36]. 19
Figure 2-2: Electric dipoles in Weiss domains; (a) unpoled ferroelectric ceramic, (b) during and (c) after poling [36]. 20
Figure 2-3: 2-2 piezo-ceramic composite structure: (a) an electron micrograph and (b) schematic view [3]. 22
Figure 2-4: Array ultrasonic transducers: (a) linear array and (b) annular array [3]. 23
Figure 2-5: Scale of things, in meters [50]. 24
Figure 2-6: Cross-sectional schematic drawing of cMUT [20]. 27
Figure 2-7: Schematic diagram of single pMUT. 29
Figure 3-1: Primary and secondary flats on silicon wafers [74]. 32
Figure 3-2: Schematic view of SOI wafer. 32
Figure 3-3: Silicon wafer after BOE. 33
Figure 3-4: Silicon wafer after boron diffusion and BOE. 34
Figure 3-5: Silicon wafer after pattern etch mask for EDP etching. 35
Figure 3-6: Schematic view of a fabricated membrane after EDP etching. 36
Figure 3-7: SEM image of membrane arrays after EDP. 37
Figure 3-8: A schematic view after sputtering Pt layer. 39
Figure 3-9: A schematic view of a membrane after PZT deposition. 40
Figure 3-10: A schematic view of a membrane after top electrode sputtering. 41
Figure 4-1: Polarization behavior of the 52/48 PZT thin film. 44
Figure 4-2: Schematic details of design with respective variables. 45
Figure 4-3: Measured impedance magnitude and impedance phase angle. 47
Figure 4-4: Equivalent circuit of electromechanical transducers. 48
Figure 4-5: Measured (solid lines) and fitted (symbols) impedance magnitude (a) and impedance phase angle (b). 50
Figure 4-6: Top view of the pMUT membrane structure; (a) small membrane, (b) large membrane. 52
Figure 4-7: Impedance magnitude for each membrane length when the membrane width is 120μm. 53
Figure 4-8: Motional inductance (L_1) as a function of membrane dimensions. 54
Figure 4-9: Motional capacitance (C_1) as a function of membrane dimensions. See Figure 4-8 for the legends. 55

Figure 4-10: Parallel capacitance (C_0) as a function of membrane dimensions before considering parasitic capacitance. See Figure 4-8 for the legends. 56
Figure 4-11: Parallel capacitance (C_0) as a function of membrane dimensions after considering parasitic capacitance. See Figure 4-8 for the legends. 57
Figure 4-12: Motional resistance (R_1) as a function of membrane dimensions. See Figure 4-8 for the legends. 58
Figure 4-13: Resonance frequency (f_s) as a function of membrane dimensions. See Figure 4-8 for the legends. 59
Figure 4-14: Effective coupling coefficient (k_{eff}^2) as a function of membrane dimensions before considering parasitic capacitance. See Figure 4-8 for the legends. 60
Figure 4-15: Effective coupling coefficient (k_{eff}^2) as a function of membrane dimensions after considering parasitic capacitance. See Figure 4-8 for the legends. 60
Figure 4-16: Quality factor (Qu) as a function of membrane dimensions. See Figure 4-8 for the legends. 61
Figure 4-17: Array type pMUTs with five 5 by 10 elements (total 250 elements). 62
Figure 4-18: An array type pMUTs connected with wires. 63
Figure 4-19: Impedance measurements of 5 by 10 array type pMUTs. 64
Figure 5-1: Coordinate system used to model the laminated composite plate. 69
Figure 5-2: Node numbering and the natural coordinate system for the conforming rectangular element. 73
Figure 5-3: Experimental data and FEA results for the thin film membrane structures. 79
Figure 5-4: Fundamental mode shape for a square membrane. 81
Figure 5-5: Simulated effects of thickness of Si and PZT layers on the fundamental frequencies of the membrane structure. The membrane size is 180µm by 860µm. The material properties and the rest of dimensions are kept the same as those shown in Table 5-5. 82
Figure 6-1: One-dimensional composite beam model. 88
Figure 6-2: Fundamental mode shape calculated by ANSYS; (a) aspect ratio = 23:1 (b) aspect ratio = 5:1. 90
Figure 6-3: 1D approximation of the mode shape. 90
Figure 6-4: Motional inductance (L1) as a function of membrane dimensions. Dash-dot and dashed lines represent the calculated results based on the composite beam model for the membranes with the largest (L=2060µm) and the smallest length (L=860µm), respectively. 99
Figure 6-5: Motional capacitance (C_1) as a function of membrane dimensions. See Figure 6-4 for the legends. 100
Figure 6-6: Parallel capacitance (C_0) as a function of membrane dimensions after considering parasitic capacitance. See Figure 6-4 for the legends. 101
Figure 6-7: Resonance frequency (f_s) as a function of membrane dimensions. See Figure 6-4 for the legends. 102
Figure 6-8: Effective coupling coefficient (k_{eff}^2) as a function of membrane dimensions after considering parasitic capacitance. See Figure 6-4 for the legends. 102
Figure 6-9: Motional inductance (L_1) as a function of membrane dimensions. Dash-dot and dashed lines represent the calculated results based on the composite beam model for

the membranes with the smallest (W = 90µm) and the largest width (W = 180µm), respectively. 105
Figure 6-10: Motional capacitance (C_1) as a function of membrane dimensions. See Figure 6-9 for the legends.. 105
Figure 6-11: Parallel capacitance (C_0) as a function of membrane dimensions before (a) and after (b) considering parasitic capacitance. See Figure 6-9 for the legends. 106
Figure 6-12: Parametric study of the residual stress effect on resonance frequencies. (a) T = 100 N/m; (b) T = 200 N/m. See Figure 6-7 for the case where T = 0........................... 108
Figure 6-13: Parametric study of the residual stress effect of residual stress on the coupling coefficients. (a) T = 100 N/m; (b) T = 200 N/m. See Figure 6-8 for the case where T = 0. 109
Figure 7-1: Two dimensional composite plate model.. 112
Figure 7-2: Motional inductance (L_1) as a function of membrane dimensions. Dash-dot and dashed lines represent the calculated results based on the 2D composite plate model for the membranes with the largest (L = 2060µm) and the smallest length (L = 860µm), respectively. 121
Figure 7-3: Motional capacitance (C_1) as a function of membrane dimensions. See Figure 7-2 for the legends. 122
Figure 7-4: Parallel capacitance (C_0) as a function of membrane dimensions after considering parasitic capacitance. See Figure 7-2 for the legends... 122
Figure 7-5: Resonance frequency (f_s) as a function of membrane dimensions. Figure 7-2 for the legends. 123
Figure 7-6: Effective coupling coefficient (k_{eff}^2) as a function of membrane dimensions after considering parasitic capacitance. Figure 7-2 for the legends. 124
Figure 7-7: Calculated frequency (f_s) while membrane size was varied.................................... 126
Figure 7-8: Calculated effective coupling coefficient (k_{eff}^2) while membrane size was varied. 126
Figure 7-9: Calculated effective coupling coefficient (k_{eff}^2) as a function of electrode coverage for both 100µm by 100µm and 500µm by 500µm membranes.............................. 128
Figure 7-10: GUI to help the optimization of pMUTs design. 130
Figure 8-1: Schematic views of acoustic test setups.. 134
Figure 8-2: Schematic view of transducer housing.. 135

List of Tables

Table 4-1: Saturation polarization, remnant polarization, and coercive field for 120µm by 1200µm membranes. 46

Table 4-2: Saturation polarization, remnant polarization, and coercive field for 90µm by 1000µm membranes. 46

Table 4-3: Saturation polarization, remnant polarization, and coercive field for 60µm by 1000µm membranes. 46

Table 5-1: Nondimensionalized maximum deflections ($\bar{w}$) of simply supported laminated plates. $\bar{w} = w_0 \left(\frac{E_2 h^3}{a^4 q_0} \right) * 100$, where a is the length of the square plate, h is the thickness of a square plate, and q_0 is the distributed load. $a/h = 10$, $E_1/E_2 = 25$, $G_{12} = E_2/2$, $\nu_{12} = 0.25$. 77

Table 5-2: Fundamental frequencies ($\varpi = \omega \left(\frac{a^2}{h} \right) \sqrt{\frac{\rho}{E_2}}$) of simply supported $(-45/45)_2$ angle-ply and $(0/90)_4$ cross-ply ($a/h = 10$, $E_1/E_2 = 40$, $G_{12} = 0.6E_2$, $\nu_{12} = 0.25$). 77

Table 5-3: Fundamental frequencies ($\varpi = \omega \left(\frac{a^2}{h} \right) \sqrt{\frac{\rho}{E_1}}$) of angle-plies under clamped boundary condition ($a/h = 16.67$, $E_1 = 60.7GPa$, $E_2 = 24.8GPa$, $G_{12}=12.0GPa$, $\nu_{12} = 0.23$). 78

Table 5-4: Sizes and numbers of elements used for the FE analysis of large membranes. 80

Table 5-5: Material properties used in the FE calculations. 80

Table 6-1: Material properties and layer thicknesses used for the analytic solutions of pMUTs. 98

List of Symbols and Abbreviations

2-MOE	2-MethOxy Ethanol
AC	Alternating Current
BEM	Boundary Element Method
BOE	Buffered Oxide Etchant
CLPT	Classical Laminated Plate Theory
cMUTs	Capacitive Micromachined Ultrasonic Transducers
DC	Direct Current
DI	Deionized
DRIE	Deep Reactive Ion Etching
Ec	Coercive Field
EDP	Ethylene Diamine Pyrochatechol
FDM	Finite Difference Method
FEM	Finite Element Method
FVM	Finite Volume Method
GUI	Graphical User Interface
HMDS	Hexamethyldisilazane
HTO	High Temperature Oxidation
IC	Integrated Circuit
IPA	IsoPropyl Alcohol
LPCVD	Low-Pressure Chemical Vapor Deposition
LTO	Low Temperature Oxidation
MEMS	Microelectromechanical Systems
MOCVD	MetalOrganic Chemical Vapor Deposition
MUTs	Micromachined Ultrasonic Transducers
PECVD	Plasma-Enhanced Chemical Vapor Deposition
PLD	Pulsed Laser Deposition
pMUTs	Piezoelectric Micromachined Ultrasonic Transducers
Pr	Remnant Polarization
Ps	Saturation Polarization
PVD	Physical Vapor Deposition
PZT	Lead (P) Zirconate Titanate
Q	Quality factor
RF	Radio Frequency
RIE	Reactive Ion Etching
rpm	Revolutions Per Minute
RTA	Rapid Thermal Annealer
SEM	Scanning Electron Microscope
SNR	Signal-to-Noise Ratio
SOI	Silicon-On-Insulator
Sol-Gel	Solution-Gelation
TEC	Thermal Expansion Coefficient
UV	Ultraviolet

Z	Acoustic Impedance

CAHPTER 1

1 Introduction

1.1 Medical Imaging Systems

Medical imaging is a field of study for scanning and visualizing human body for diagnosis. Imaging technology was used mainly for the defense and the space science communities in the past but its application has been expanded to medical field by the advent of powerful and less-expensive computers [1]. The examples of medical imaging systems are x-ray, computed tomography (CT), magnetic resonance imaging (MRI), ultrasonic imaging, positron emission tomography (PET), nuclear medicine, magnetic resonance microscopy (MR microscopy), and electrical impedance tomography, etc.

Each imaging system has pros and cons. For example, x-ray system is the most famous medical imaging modality. The equipment is less expensive compared to other medical imaging systems such as CT, MRI, and PET. The system is also fast to get the result and the diagnostic procedures are simple [1]. However, x-ray systems cannot be used for a pregnant woman and the image from x-ray system is only black and white. CT and MRI became available in the 1970s and 1980s, respectively, for advanced medical imaging. Physicians can obtain high-quality tomographic images of internal structure of the body and images with exceptional contrast for soft tissues from CT and MRI, respectively [1]. However, they both have some limitations. For example, CT cannot be used for a pregnant woman and MRI is not acceptable to a patient with metallic implant.

Ultrasonic imaging is the safest medical imaging system among the aforementioned medical imaging systems. It is also very cost effective compared to CT, MRI, nuclear imaging and PET [2]. With curtailing health care costs being a national agenda, this offers a unique advantage. It also has some other advantages such as real time imaging, higher resolution which may achieved by higher operating frequency, and the portability of the equipment [3]. One major disadvantage is that the areas that can be scanned by ultrasound are still quite limited at this time. For example, it cannot be used to scan organs which contain gases. The quality of ultrasonic imaging also depends on the operator's skill.

1.2 Medical Imaging Using Ultrasound

This research is focused on ultrasonic medical imaging. The history of ultrasound as an imaging modality dated back to late 1940s as part of the sonar and radar technology developed during World War II [3]. It has evolved into a major diagnostic tool in medicine since early 1970's. The primary form of ultrasonic imaging is pulse-echo mode, and pulsed Doppler ultrasound devices also became available for measuring blood flow [3]. Currently, ultrasonic imaging is the second most utilized diagnostic imaging system after x-ray [3]. Even though ultrasonic imaging is a fairly mature tool in the areas of obstetrics, cardiology, and gynecology, its applications are still rapidly expanding with the newly developed technologies. Harmonic imaging, flow and tissue displacement imaging and multidimensional imaging are the results of advanced ultrasonic transducers [3]. Intravascular imaging with probes mounted on catheter tips at frequencies higher than 20MHz, endoscopic imaging with tip-mounted probes at frequencies from 5 to 20MHZ, and ophthalmological and dermatological imaging at frequencies higher than

50MHz are few examples of the results of the technologies for operating ultrasound at higher frequencies [2].

The images generated by the current ultrasound technology are mostly two dimensional (2D) obtained by 1D array transducers combined with computed tomography [4-7, 11]. However, any 3D reconstruction based on 2D images inherently reduces the available information because only the surface is shown or some depth related integral is performed [4]. A summary of the limitations of 2D images follows.

- Volumetric information cannot be accurately determined. In 2D ultrasonic images, the volume is assumed to be approximately axisymmetric and 2D view is used as the basis for obtaining 3D images through extrapolation [4]. Thus, the calculated volumetric information based on 2D images is not as accurate as the information based on directly measured 3D ultrasonic images.
- The analysis of 2D ultrasound images is subjective because it relies on the experience and knowledge of the diagnostician for manipulating the ultrasound transducer, mentally transforming the 2D images into a 3D structure and making the diagnosis or performing in interventional procedure [5].
- In quantitative perspective, 2D ultrasonic images are poor imaging modality because it is difficult to localize the thin 2D ultrasound image plane in the organ and hard to reproduce a particular image location at a later time [5].
- Since the location and orientation of 2D images are controlled by ultrasound transducer, sometimes particular views can not be obtained because of the restrictions imposed by the patient’s anatomy or position [6].

The limitations summarized above are expected to be overcome by 3D volumetric scan. Specifically a real-time 3D ultrasound imaging offers the following unique advantages.

- 3D ultrasound images give more clear information about the scanned organ or tissue structure. Quantitative evaluation of 3D ultrasound images also reduces the subjectivity in the analysis of images and the results are less relevant to the diagnostician's experience [7]. Two ultrasound images are provided in Figure 1-1 to show the advantages of 3D ultrasound image compared to 2D image [8]. It is obvious that much more information can be retrieved from the 3D ultrasound image.
- Real-time 3D ultrasound imaging does not require any form of post image manipulation on a computer to reconstruct 3D images from 2D images and it provides real volumetric images to allow 3D visualization of anatomy, the assessment of cardiac anatomy, and function during a single cardiac cycle [5-7].

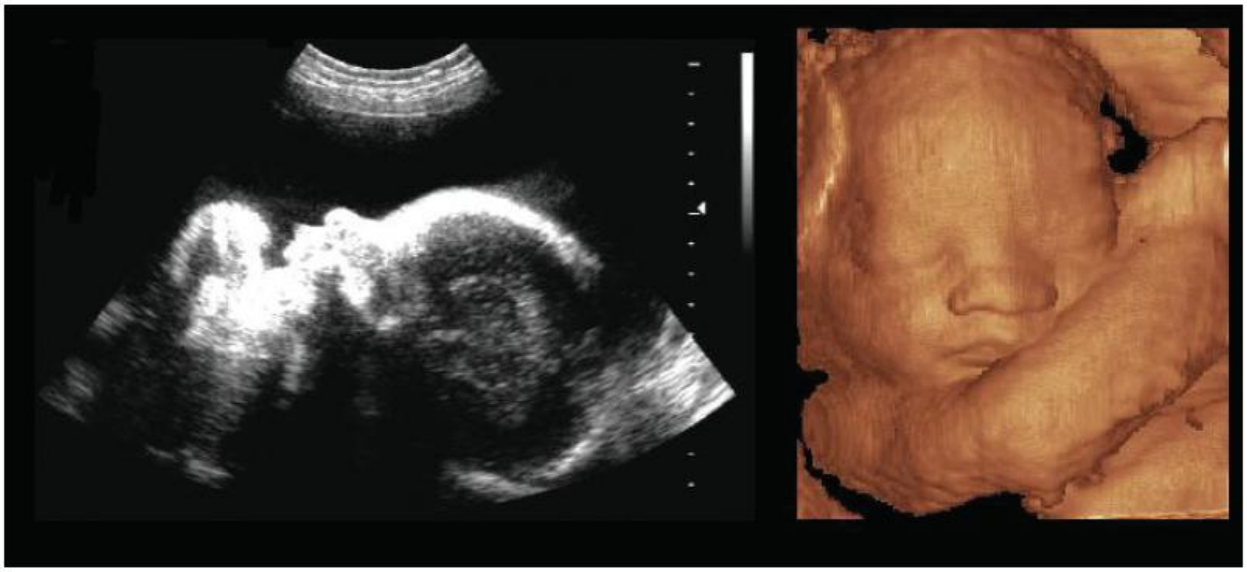

Figure 1-1: 2D (left) and 3D (right) ultrasound images of a third-trimester fetus [8].

- Ultrasound provides high frame rate (10 to 60 images per second) topographic images and the orientation of the images is flexible because they are not necessarily acquired as a stack of planes [5, 6]. The frame rate for CT and MRI is usually much slower compared to the frame rate of ultrasound and the orientation is fixed for CT and MRI [5, 6]. The high frame rate of image acquisition and the flexibility of the ultrasound provide the potential possibility in extending ultrasound imaging from its 2D to 3D and dynamic 3D (4D, real-time 3D) visualization [6]. Figure 1-2 shows the comparison between an axial slice of 3D ultrasound and MRI images of infant heart [9]. As can be seen in Figure 1-2, 3D ultrasound and MRI provide similar information about ventricle size and structure at this level [9].

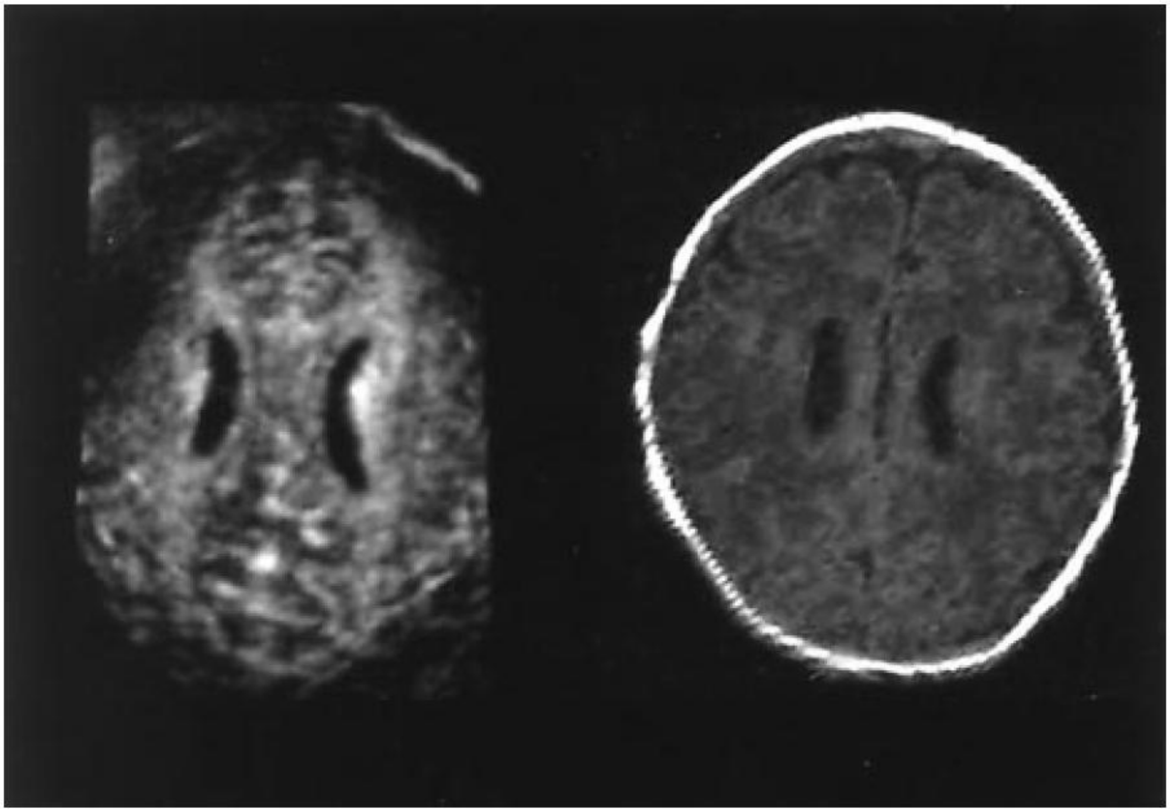

Figure 1-2: Axial slice of 3D ultrasound (left) and corresponding MRI (right) images of infant heart [9].

- 3D imaging also minimizes the probability to rescan the patient. Obtaining a single 3D scan of the entire region of interest will take less time than scanning the patient in real-time to search, record, and find the optimal 2D views [4].
- Once 3D image is generated and saved, 2D cross-sectional image can be obtained in any orientation without restriction [6]. Examples of cross-sectional images from a volumetric 3D image are given in Figure 1-3 [10].

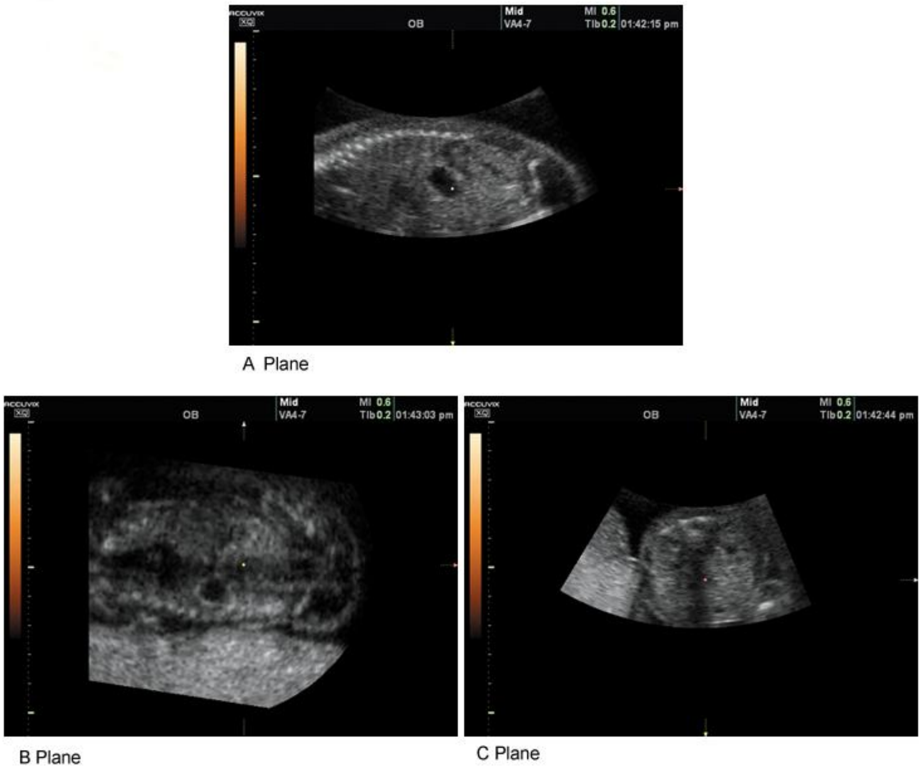

(a)

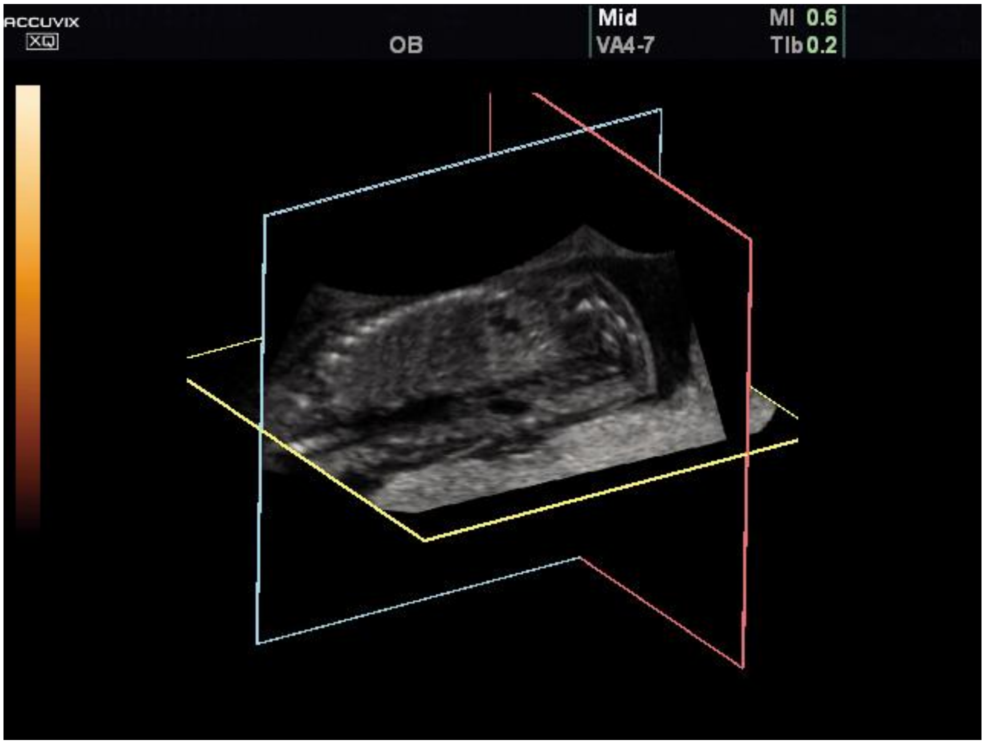

(b)

Figure 1-3: Three cross sectional images (a) from a volumetric 3D image of abdomen of a seven month fetus [10].

The real-time 3D images can be obtained by 2D arrays ultrasonic transducers [12, 13]. The main bottleneck of 2D array ultrasonic transducers for 3D imaging is the availability of transducers/arrays offering better resolution, sensitivity and its fabrication technique [2]. This research is mainly focused on the development of micron-size ultrasound transducers using MEMS technology and novel array ultrasonic transducers for 3D real-time ultrasound imaging.

1.3 Ultrasound Transducers

Transducers are devices which transform one form of energy into another form. For example, an ultrasonic transducer transforms electrical input energy into acoustic energy for actuating part, and vice versa for sensing part. Ultrasound is a sound wave which has frequency range above 20 KHz. We call ‘ultrasound’ because human cannot hear sound wave above 20 KHz. There are several methods for generating and sensing ultrasound waves such as piezoelectric, electromagnetic, acoustic, and laser methods [14]. Among those methods, piezoelectric method is the most common technique in the medical imaging field. The working mechanism of piezoelectric transducers will be explained in Chapter 2.

The simplest piezoelectric transducer is a piston type transducer as shown in Figure 1-4 [15]. The surface of the transducer is ‘wear plate’ which will contact to the patient and it will be grounded for the safety of the patient. It also protects the active element of transducer and may act as an acoustic lens to help beam forming [1]. The layer on the wear plate (in red) is the piezoelectric material called ‘active element’. Active element is the most important component of an ultrasound transducer. A number of factors need to be considered in choosing a proper piezoelectric material for transmitting and/or receiving the ultrasonic wave [3]. A matching layer is quite often laid between the active element and the wear plate to match the acoustic impedance of ultrasound transducer to the load medium. The materials for matching layer are usually epoxy or glass in traditional ultrasound transducers [1]. The material properties of backing material are important for better bandwidth and sensitivity. Epoxy composite materials are the common selections of backing material. An acoustic isolating material is used between the housing and the active element to prevent ringing of the housing that follows the vibration of the piezoelectric element [3]. The material for housing is usually metal or plastic pipes and it is commonly used as ground if a metallic housing is used.

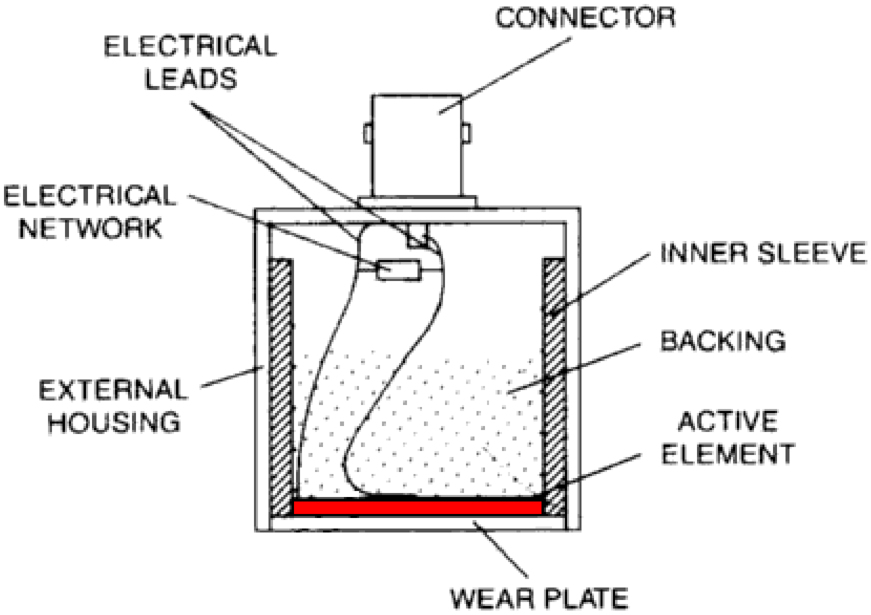

Figure 1-4: A piston type single element ultrasonic transducer [15].

The characteristics of ultrasonic transducers are natural resonant frequency, wave length, period, electromechanical coupling coefficient, quality factor, acoustic impedance, electrical impedance, beam profile, signal-to-noise ratio (SNR), etc. These characteristics of ultrasonic transducers are mostly controlled by the size and material properties of active element, matching layer, wear plate and backing material. A Brief introduction of the characteristics of ultrasonic transducers follows

Ultrasonic transducers have the maximum deformation at their first resonant frequencies. They are usually designed to vibrate at the first resonant frequencies to generate strong ultrasonic waves. In conventional ultrasonic transducers, the resonance frequency is controlled by the thickness of the active element that is a thin cylindrical disk. In this case, resonant frequency can be calculated as

$$f = \frac{c}{2d} \tag{1-1}$$

where c is the speed of sound in the active element and d is its thickness. The wavelength (λ) and period (T) have the following relations with resonant frequency.

$$T = \frac{1}{f} \tag{1-2}$$

$$\lambda = \frac{c}{f} \tag{1-3}$$

Electromechanical coupling coefficient presents the ability of a material to convert one form of energy into another and it is defined as follows [3, 16].

$$\begin{aligned} &k^2 = (\text{stored mechanical energy/supplied electrical energy}) \\ &or\ k^2 = (\text{stored electrical energy/supplied mechanical energy}) \end{aligned} \tag{1-4}$$

It should be kept in mind that coupling effective coefficient is different from efficiency of a transducer. For a lossless ultrasound transducer, its efficiency is 100% but its electromechanical coupling coefficient is not necessarily 100% because only the stored mechanical energy is useful for energy transduction [3]. For example, if 50% of input energy is stored as mechanical energy and rest of 50% of input energy stored dielectrically in the form of electrical potential energy, the electromechanical coupling coefficient is 50% while the efficiency of the transducer is 100%.

Amplitude of a vibrating object is maximized at its resonant frequency. The amplitude will be limited by the damping effects acting on the system and the level of damping can be expressed by its quality factor (Qu). Qu is defined as a ratio of the total energy stored in the system (E_M) to the energy lost per cycle (E_C) in the energy concept and it is also formulated in terms of frequencies as

$$Q = 2\pi\left(\frac{E_M}{E_c}\right) = \frac{f_0}{f_2 - f_1} \tag{1-5}$$

where f_0 is the resonant frequency at the maximum amplitude, f_1 and f_2 are the frequencies corresponds to amplitudes of vibration 6 dB lower than the maximum amplitude as shown in Figure 1-5 [17, 18]. High Q value means the system is well isolated from external forces which may cause damping effect. Therefore, the system requires less energy to continue its resonance vibration with the maximum amplitude.

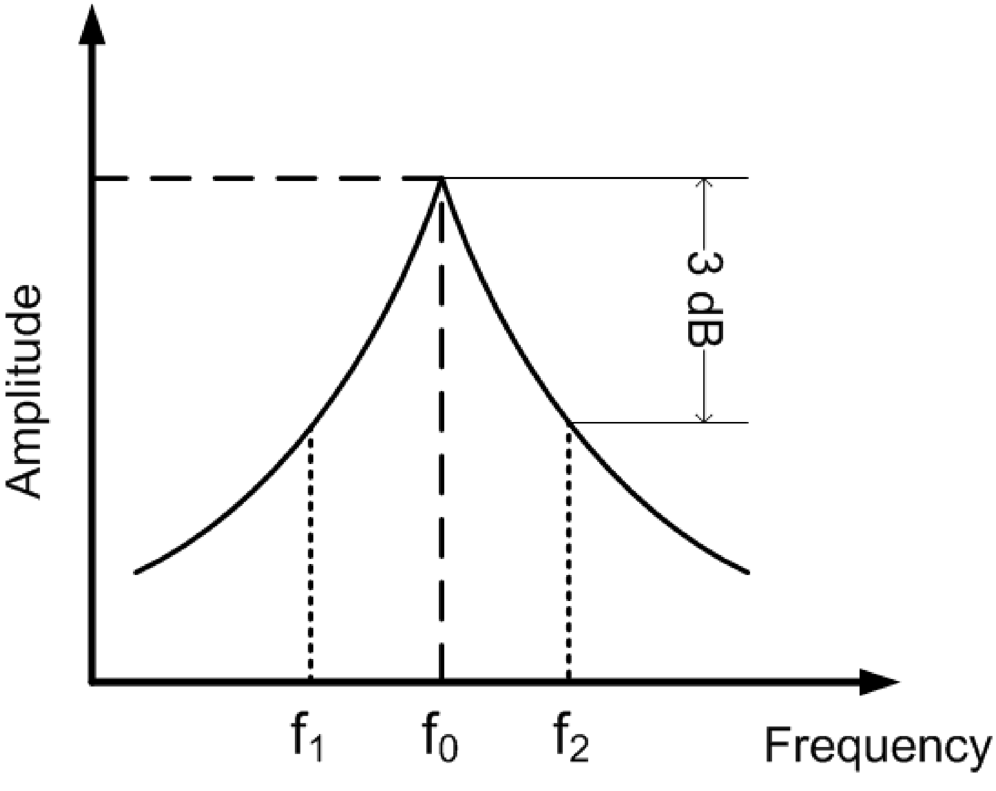

Figure 1-5: Frequency VS. amplitude for a typical resonant system.

Acoustic impedance (Z) of a material is defined as

$$Z = \rho c \tag{1-6}$$

where ρ is the density and c is the speed of sound in the material. Its units are $\left[kg/\left(m^2 \sec\right)\right]$ or Rayls. Acoustic impedance is important in designing ultrasonic transducers because it determines the amount of reflected or transmitted acoustic energy at the contact surface of two different materials which have different acoustic impedances. For example, acoustic impedance of lead zirconate titanate (PZT) 5H, which is one of the most famous commercially available PZT, is 34.3 Mrayl in plate mode and the acoustic impedances of fat and liver are 1.38 Mrayl and 1.65 Mrayl, respectively [3]. Because of the acoustic impedance mismatch, most of the input acoustic wave will be reflected if plane mode PZT-5H is directly used to a human body. To solve this problem, matching layer is introduced between the active element and wear plate. Sometimes, gel type coupling substances are applied between a ultrasonic transducer and patient's body to improve the acoustic energy transmission. The reflection and transmission coefficients are defined as

$$reflection\ coefficient = \frac{Z_2 - Z_1}{Z_2 + Z_1} \tag{1-7}$$

$$transmission\ coefficient = \frac{2Z_2}{Z_2 + Z_1} \tag{1-8}$$

where Z_1 and Z_2 are the acoustic impedances in materials 1 and 2 as shown in Figure 1-6 [14].

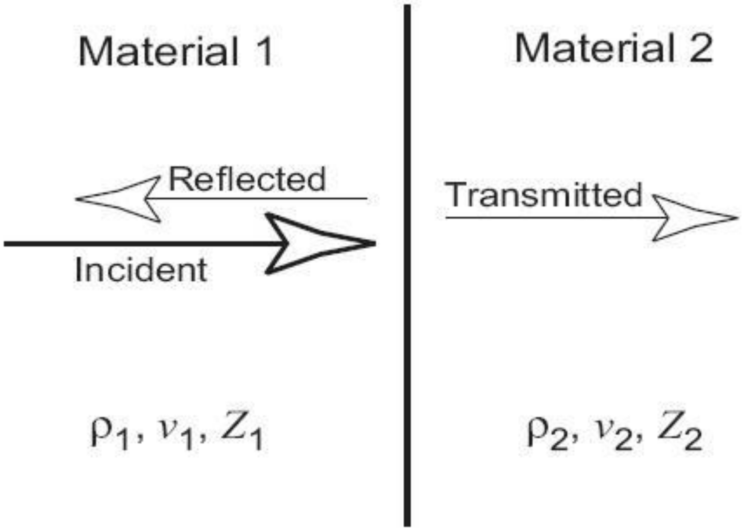

Figure 1-6: Reflected and transmitted waves of normal incident wave at an interface between two materials [14].

Electrical impedance matching is importance for signal-to-noise ratio (SNR) of an ultrasonic transducer. SNR and bandwidth are improved by matching the electrical impedance of a transducer to the transmit circuitry [1]. When the impedance of transmitter is Z_0 and the real impedance of transducer is Z_t, the power efficiency is given as

$$\frac{P_{out}}{P_{in}} = \frac{4Z_0Z_t}{(Z_0 + Z_t)^2} \tag{1-9}$$

where P_{out} and P_{in} are the power output and the power input from the transmitter, respectively [1]. The maximum power output is possible when $Z_0 = Z_t$ which means the electrical impedances are the same.

Beam profile of an ultrasonic transducer should be calculated to characterize the transducer. There are near filed and far field in ultrasonic beam as shown in Figure 1-7 [3]. Near field is the region where the series of minima and maxima amplitudes exist until at the last maximum axial pressure (Z_0) and far field is the zone after near field and the axial pressure decreases approximately according to $1/z$ at the far field [3, 19]. Focusing of ultrasonic beam is important to get better axial resolution and it can be done by using lens, proper wear plate, and focused element.

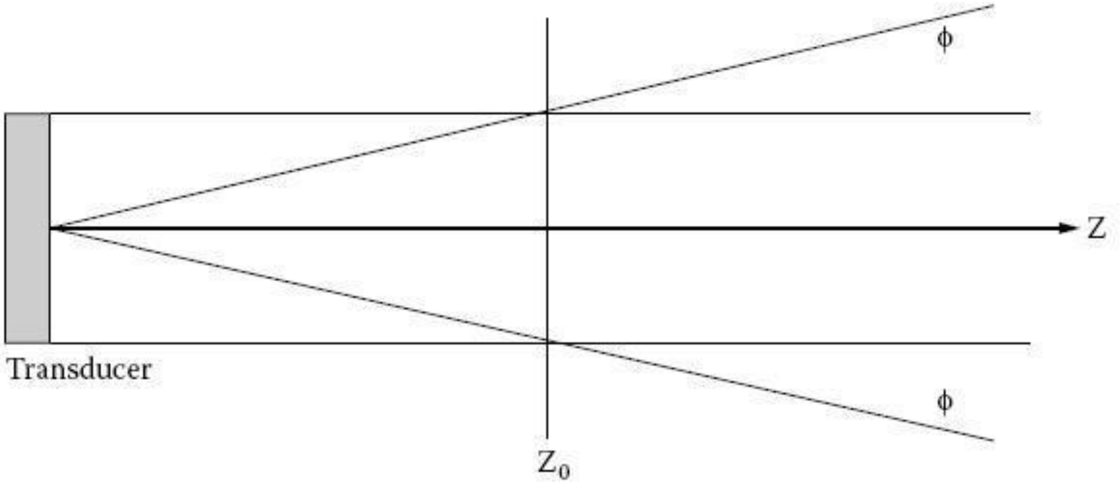

Figure 1-7: Beam profile of a single element piston transducer [3].

1.4 Motivations

The majority of conventional ultrasonic imaging systems are equipped with a variety of probes with conventional piezoelectric transducers that have a linear array of different frequencies. These arrays typically have been fabricated with the dice and fill technology, which is rather expensive and time-consuming [2]. Recently, due to the matured silicon micromachining technology, fabrication of micron size devices that are working at ultrasonic frequency range is possible [20]. Micromachined ultrasonic transducers (MUTs) are one application where MEMS miniaturization is expected to offer significant advantages over the current bulk piezoelectric transducers. Capacitive micromachined ultrasonic transducers (cMUTs) and piezoelectric micromachined ultrasonic transducers (pMUTs) that use MEMS technology have been introduced for array type transducer fabrication to subdue the limitations of conventional bulk piezoelectric transducers [21, 22]. Since their advent, these two approaches have been the major working principles for developing novel transducers for ultrasound medical imaging applications. Compared to the traditional bulk PZT ceramic based ultrasonic transducers whose operating characteristics are controlled by the dimension and properties of the bulk PZT ceramic, the composite structures of cMUT and pMUT offer a much more flexible approach to the development of advanced micron size ultrasonic transducers. The performance of these miniaturized transducers has shown the strong possibility to replace the conventional ultrasonic transducers.

Real-time 3D ultrasound images promise many advantages compared to 2D ultrasound images as explained in Section 1.2. To get real-time 3D ultrasound images, 2D arrays of ultrasound transducers are necessary. Unfortunately, fabricating 2D array transducers by conventional dice and fill technology is almost impossible because of the enormous number of cables to be connected and the possible minimum transducer size. However, this restriction can be overcome by integrating MEMS technology into the array design and the fabrication of micron size ultrasound transducers. With the MEMS technology, those miniaturized transducers can be formed into a 2D array, which should be capable of producing real-time 3D images [2].

Fabrication of thin film structures is both a time-consuming and costly process. As the design flexibility increases, so does the demand for a new design methodology. A typical design methodology consists of both analytical study and numerical simulation. Examples of the analytical models can be found in the works by Smits *et al* [23], DeVoe *et al.* [24], and Weinberg [25] for piezoelectric cantilever actuators/sensors; Percin *et al.* [26, 27] for circular piezoelectrically actuated ultrasound transducers; and Cho *et al.* [28] for a MEMS device designed for energy harvesting purpose. An adequate analytical model may be needed to be developed to help the development of pMUTs. There are also some commercial software available for numerical simulations such as the ANSYS used in [29] and the PZFlex used in [30, 31]. However, as common to most of the commercial software, they in general lack the flexibility to address many specific issues that may be encountered in the development of new devices. Thus, it is advantageous and sometimes necessary to develop a special-purpose code or software as part of the design tool for product development.

1.5 Research Objectives

The ultimate goal of this research is to make commercially viable 2D arrays of ultrasonic transducers using MEMS technology for real-time 3D imaging and for futuristic therapeutic applications. This research has the potential to open up other possibilities such as combined endoscopes and catheter mounted probes which could be inserted into the human body for imaging as well as therapeutic needs. Though the need for such devices has long been proven, no such devices are commercially available even today. The methodology that will be used would be a hybrid experimental-numerical approach.

The research work for this dissertation is focused on the design, fabrication, characterization and modeling of pMUTs. Design and fabrication of single element pMUTs are the starting point for the fabrication of array pMUTs. Prior to optimizing array pMUTs, single element pMUTs must be characterized and optimized. Characterization of single element pMUTs can be done by electrical impedance measurement using an impedance analyzer or pulse-echo test using pulser-receiver or microphone. The results will be then used for new designs to find optimal design parameters and they will be the benchmark to develop modeling tools for pMUTs. The optimized design parameters of single element pMUT will be used for designing array type pMUTs.

For the modeling aspect of this research, analytical models and a finite element code will be developed to predict and optimize the electromechanical performance of pMUTs. Modeling of pMUTs is an essential part for the characterization and optimization of single element pMUTs. The analytical models provide rapid and rational insights, while the FE model renders a detailed analysis of the response of the structures. Once the models are developed, the model predictions will be compared with the experimental results. The analytical models will be developed by modeling pMUT as a coupled electromechanical composite beam (1D) or plate (2D) using MATLAB. FORTRAN will be used for the FE model, which will be based on a combination of classical laminated plate theory and equivalent single plate theory. Conforming rectangular element is used as the element in the FEM code. The optimization is focused on the resonance frequency and the effective coupling coefficient of pMUTs.

CHAPTER 2

2 PZT Based MEMS Devices

2.1 Piezoelectricity

The piezoelectric effect was discovered in 1880 by Pierre and Jacques Curie and it is an interaction between electrical and mechanical systems [16]. There are two piezoelectric effects; direct and converse piezoelectric effects. For direct piezoelectric effect, piezoelectric material becomes electrically charged when subjected to a mechanical stress. A device using direct piezoelectric effect can be used to detect strain, movement, force, pressure or vibration by developing appropriate electrical responses, as in the case of force and acoustic sensors [32]. Converse piezoelectric effect occurred by the piezoelectric material becomes strained when placed in an electric field. Devices using converse piezoelectric effect can be used to generate strain, movement, force, pressure, or vibration through the application of suitable electric field [32]. Piezoelectric materials thus have a link between mechanical and electrical properties. This character is defined by effective coupling coefficient (k_{eff}^2) which is defined as the transduced electrical or mechanical energy over the total input energy to the system [33].

Piezoelectric effect arises because of asymmetries in the crystal structure that creates an electric dipole moment in the crystal lattice which is sensitive to both elastic strain and applied electric field. Of the thirty-two crystal classes, twenty have the type of asymmetry that can give an elastic-electrical interaction, and ten of them exhibit spontaneous and reversible polarization. They are said to be ferroelectric materials [34, 35].

The most commonly used ferroelectric materials are the members of the perovskite family of ferroelectric ceramics, which includes barium titanate ($BaTiO_3$), lead titanate ($PbTiO_3$) and many alloys in the PZT system; lead zirconate-lead titanate ($PbZr_xTi_{(1-x)}O_3$) [35]. These groups of ceramics are perovskite type because their crystal structures are similar to that of the mineral perovskite ($CaTiO_3$). Piezoelectric effect arises due to the ability of the center ions to "wobble" in the unit cell in response to an applied stress or electric field [36]. Figure 2-1 shows the unit cell of PZT which is one of the most common piezoelectric materials for MEMS applications. The crystal structure is centro-symmetric cubic (isotropic) before poling and it is tetragonal symmetry (anisotropic) after poling below the Curie temperature. Piezoelectric crystals lose piezoelectric properties above this temperature. Unsymmetrical crystal structure between the positive and negative ions is the reason why piezoelectric materials have dipoles.

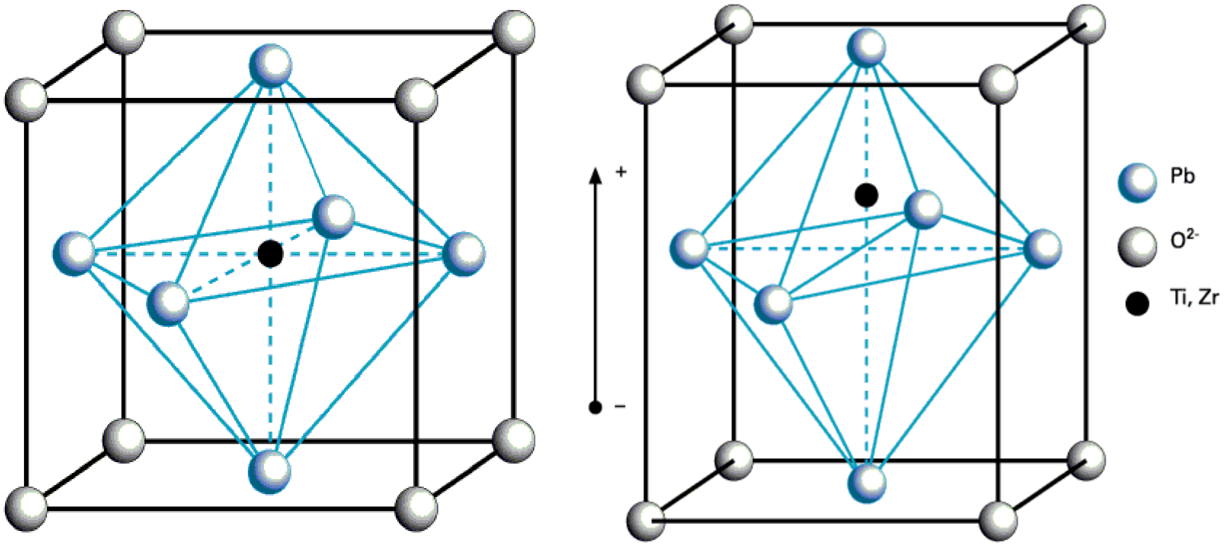

(a) (b)

Figure 2-1: Piezoelectric elementary cell; (a): before poling, (b): after poling [36].

Groups of dipoles with parallel orientation are called Weiss domain and the dipoles are randomly oriented before the material is poled by an electric field as shown in Figure 2-2(a) [36]. When the electric field is applied to a Weiss domain, it expands along the axis of the applied electric field and shrinks in perpendicular direction as shown in Figure 2-2(b). When the electric field is not applied after poling, dipoles do not align as during poling but they are still aligned in one direction as shown in Figure 2-2(c) and this is called remnant polarization (P_r).

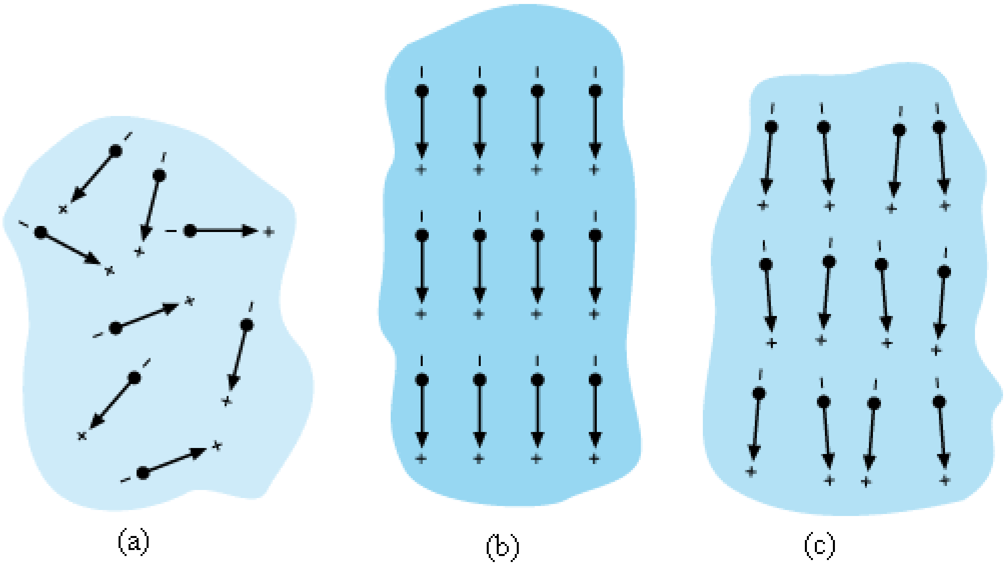

Figure 2-2: Electric dipoles in Weiss domains; (a) unpoled ferroelectric ceramic, (b) during and (c) after poling [36].

2.1.1 PZT Thin Film Deposition

PZT thin film is often used as the actuating/sensing component in MEMS devices due to its excellent polarization values, dielectric constant, and piezoelectric constant. PZT thin film is advantageous compared to the bulk PZT ceramic for MEMS applications because of its miniature size, lower operating voltage, geometrical flexibility and easy integration to various devices. Another major advantage of PZT thin film is the drastic reduction of sintering temperature as opposed to the bulk PZT ceramic. The sintering temperature for PZT thin film can be as low as 500^{o}C and the required temperature exceeds 1200^{o}C for bulk PZT ceramic [37]. Therefore, the substrate does not need to go through severally high temperature for crystallization of the PZT thin film.

Deposition of PZT thin film is one of the most critical processes for the fabrication of piezoelectric MEMS devices. Several different techniques have been introduced such as metalorganic chemical vapor deposition (MOCVD) [38, 39], ion-beam deposition [40], magnetron and RF sputtering [41-43], solution-gelation (Sol-Gel) method [44, 45] and pulsed laser deposition (PLD) [46]. Ion-beam deposition, magnetron sputtering, RF sputtering and PLD are included in physical vapor deposition (PVD). PVD vaporizes a solid or powder targets using ion-beam, plasma, heat or laser and the target materials are then sputtered onto the substrate [41, 47]. MOCVD uses heat energy to activate the chemical reaction using precursor gases. By MOCVD, stoichiometry can be precisely controlled by adjusting the flows of the gaseous precursors, thus making it a suitable candidate for the preparation of PZT thin film for MEMS applications [47]. For sol-gel method, a precursor solution is synthesized by a series of distillation and refluxing steps to generate a mixture of metalorganic compounds [37]. It is a convenient and cost effective technique for fabrication of PZT thin films.

2.1.2 Sol-Gel Method

Among these different deposition methods, sol-gel is the most common and oldest method due to ease of stoichiometric control, ease of fabrication, low cost and superior piezoelectric properties [37, 45]. Sol-gel method can also accommodate dopants to modify the properties or viscosity of piezoelectric precursor solution so that rates up to 2μm thickness per layer have been reported when additives were used [44, 48]. Deposition of the PZT solution is usually done by spin coating following pyrolysis and crystallization of the film. Multiple layers can be deposited to increase the thickness of the PZT thin film. Crystallization is done using either conventional furnace or rapid thermal annealer (RTA) at 650 or 700°C [44, 45].

2.2 Micromachined Ultrasonic Transducers

Ultrasound has been used as a major medical imaging tool since the early 1970’s. The majority of conventional ultrasonic imaging systems are equipped with a variety of probes with conventional piezoelectric transducers that have a linear array of different frequencies. These arrays typically have been fabricated with the dice and fill technology as shown in Figure 2-3 [2, 3], which is rather expensive and time consuming. Schematic views of linear and annular arrays of ultrasonic transducers are presented in Figure 2-4.

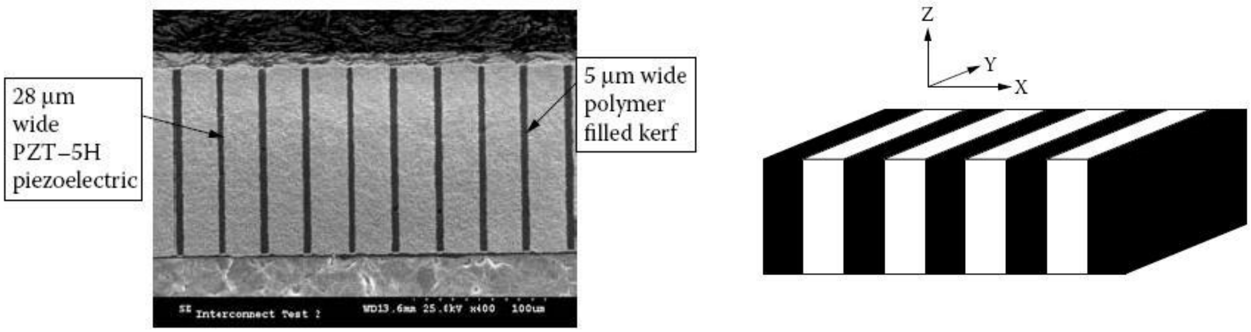

(a) (b)

Figure 2-3: 2-2 piezo-ceramic composite structure: (a) an electron micrograph and (b) schematic view [3].

Micromachined ultrasonic transducers (MUTs) are one of the applications where MEMS miniaturization is expected to offer significant advantages over the current bulk PZT transducers. Recently, to alleviate the problems of conventional ultrasonic transducers, capacitive micromachined ultrasonic transducers (cMUTs) and piezoelectric micromachined ultrasonic transducers (pMUTs) that use MEMS technology have been introduced for array type transducer fabrication [21, 22]. Miniaturizing capability of the silicon micromachining process has made the fabrication of devices possible to work at ultrasonic frequencies [20]. Since their advent, these two working principles have been competing with each other for high frequency, 3D real-time imaging and low cost applications [49]. The performance of these miniaturized ultrasonic transducers has shown the strong possibility to replace the conventional ultrasonic transducers. With the MEMS technology, those miniaturized transducers can be formed into a 2D array, which should be capable of producing real-time images in 3D [2].

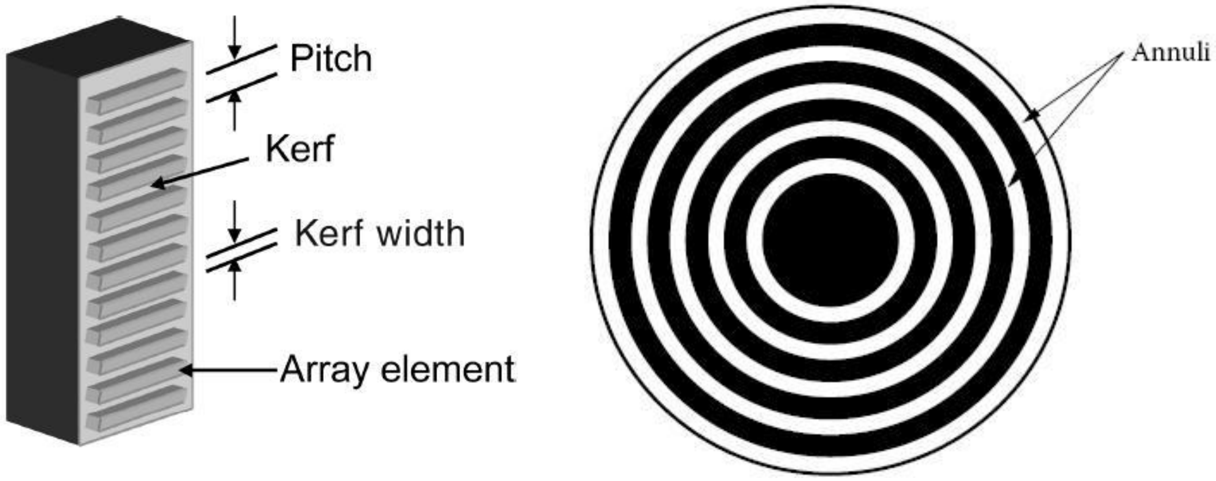

(a) (b)

Figure 2-4: Array ultrasonic transducers: (a) linear array and (b) annular array [3].

2.2.1 Microelectromechanical Systems (MEMS)

Microelectromechanical systems (MEMS) is defined as devices that are fabricated using integrated circuit batch-processing technologies, and they have the characteristic length of less than 1mm but more than 1micron in terms of the size, and perform coupled electromechanical functions [50]. Figure 2-5 compares the size of MEMS devices relative to other objects in the world. The motivation for MEMS research results from the needs of producing devices in micron size, that have the same or better performance compared to the conventional devices and can be produced at a lower cost by using matured batch fabrication techniques of the semiconductor industry.

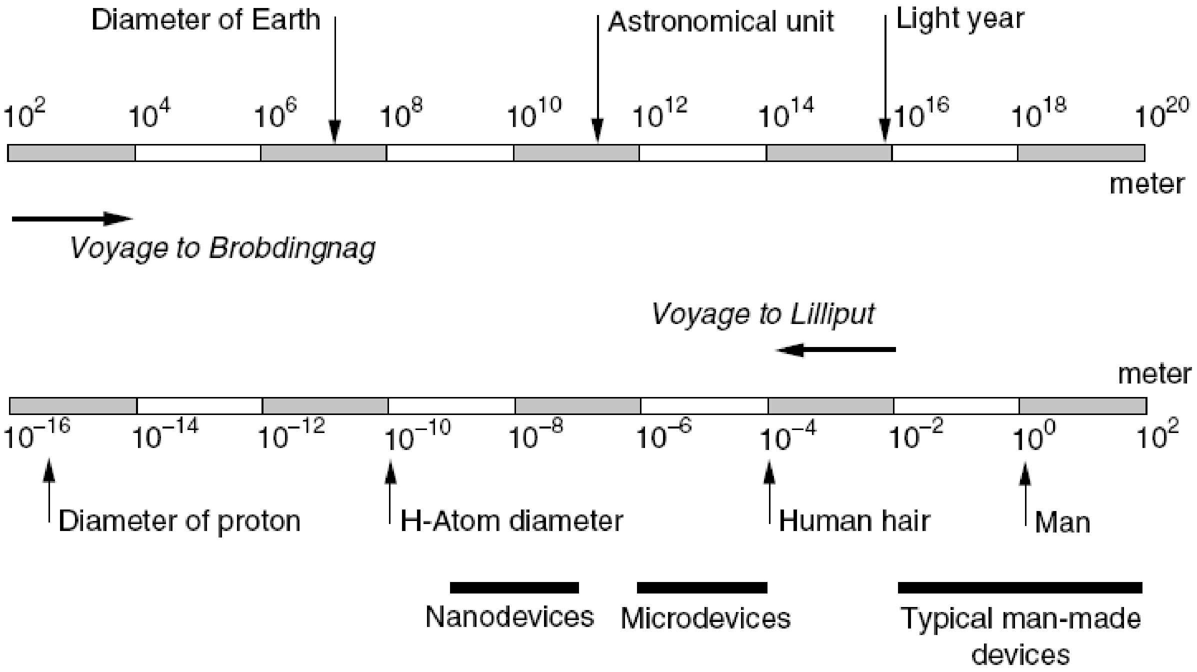

Figure 2-5: Scale of things, in meters [50].

The concept of MEMS originated from the famed physicist Richard P. Feynman in his lecture titled '*There's Plenty of Room at the Bottom*' at the annual meeting of the American

Physical Society at the California Institute of Technology in 1959. Fortunately, this lecture is available as a manuscript in Ref. [51]. In his lecture, Feynman suggested miniaturization of devices including computer and the advantages of miniaturized devices. In his other lecture titled '*Infinitesimal Machinery*' at the Jet Propulsion Laboratory in 1983, he said '*There is no use for these machines, so I still don't understand why I'm fascinated by the question of making small machines with movable and controllable parts*' [52]. In this talk, he explained how to fabricate three-dimensional pattern using silicon, how to make mobile micro-robots, how to control small machines, what are the problems of small object, and new computing method with atoms. Even though Feynman said that there is no use for small machines in 1983, MEMS devices were commercialized around 1990s and there are too many applications and commercial products to mention at this moment [53].

The major commercial markets for MEMS products are computer storage systems and automobiles industries [54]. A few other applications of MEMS devices include keyless entry systems, dense arrays of micromirrors for high-definition optical displays, scanning electron microscope tips to image single atoms, disposable blood pressure transducers, inertial sensors, micro valves/pumps, and micro heat exchangers [50, 53-55]. Global funding for micro/nano technology research was \$2.2 billion in 2002 which was \$432 million in 1997 [50]. Therefore, the commercial markets for MEMS products are rapidly growing.

Silicon is the most common material for MEMS application. Kurt Peterson introduced the excellent mechanical properties of single crystal silicon for inexpensive, batch-fabricated and high-performance MEMS devices [56]. Fabrication techniques for MEMS can be categorized into two methods; surface micromachining and bulk micromachining. Surface micromachining is done by depositing, patterning and etching a sequence of thin films [53]. In bulk micromachining, features are patterned and shaped to form an important functional component of the resulting device by orientation-dependent (anisotropic) and/or by orientation-independent (isotropic) fabrication methods such as wet etching, deep reactive ion etching/reactive ion etching (DRIE/RIE), micromolding, etc [53, 57].

Many of the microfabrication techniques are borrowed from the matured IC industry such as photolithography, thermal oxidation, dopant diffusion, ion implantation, DC/RF sputtering, RIE, low-pressure chemical vapor deposition (LPCVD), plasma-enhanced chemical vapor deposition (PECVD), etc [53, 55]. Silicon, silicon dioxide, silicon nitride and aluminum are the materials borrowed from the IC industry for MEMS fabrication [53, 55]. There are additional processes and materials commonly used for MEMS technology, such as the anisotropic wet etching, DRIE, x-ray lithography, thick film resist, spin coating and micromolding for the process, and piezoelectric film, magnetic film, high-temperature materials, aluminum alloys and platinum for the materials.

2.2.2 Capacitive Micromachined Ultrasonic Transducers

Capacitive Micromachined Ultrasonic Transducers (cMUTs) are made of thin silicon-nitride membranes, which are essentially parallel plate capacitors with a gap between two plates. Figure 2-6 is a schematic drawing of the cross section of a cMUT [20, 21]. When a voltage is applied across the aluminum top electrode and silicon substrate which is the bottom electrode, electrostatic forces attract upper side of the membrane toward the silicone substrate and the generated stress within the membrane drives the structure to resist the attraction. If the membrane is driven by an alternating current at its mechanical resonance frequency, large displacements and consequently significant sound generation will result. Conversely, if the membrane is biased appropriately and subjected to ultrasonic waves at resonant frequencies, significant detection currents will be generated on the electrodes [58]. The frequency of the membrane in vibration is twice the applied AC voltage frequency because electrostatic force is unipolar. Therefore, a DC bias voltage, which is larger than the AC voltage amplitude, is required for proper operation of cMUTs [20]. A DC voltage is required to detect the harmonic vibration of the membranes by an incident acoustic wave. Under the constant bias voltage supplied, the capacitance variations result in a current flow in the external electric circuit, which is amplified for further processing [20]. In this way, cMUTs can detect the reflected acoustic wave from an object.

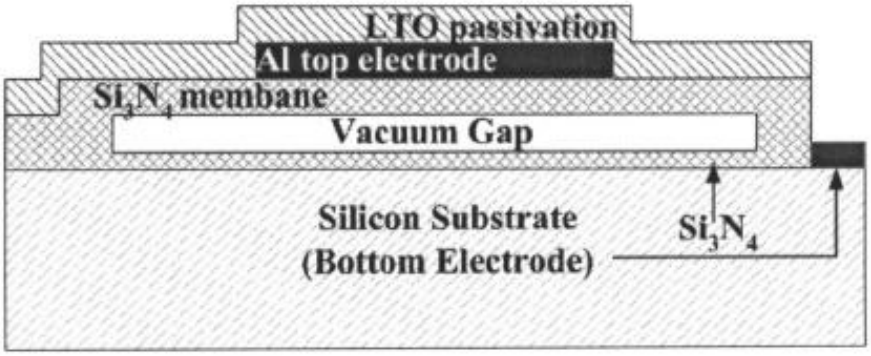

Figure 2-6: Cross-sectional schematic drawing of cMUT [20].

Phased subarray imaging may be introduced to overcome the poor image quality of a classical synthetic aperture [59, 60]. Forward-viewing annular array is fabricated which could replace a catheter probe that is side-viewing array [61]. Previous works on cMUTs showed the advantages of cMUTs compared to conventional piezoelectric transducers [20, 21, 58]; the possibility of making 2D arrays of ultrasonic transducers for 3D imaging [59, 60, 62] and making forward-viewing endoscope [61]. However, there are practical limitations for operation and fabrication of cMUTs. It seems difficult to secure an intended safety margin to avoid collapse on all the array elements due to the bias voltage [30]. It is also difficult to get the theoretical coupling coefficient in reality because the bias voltage must be close to the collapse voltage of the cMUT [63] to achieve the theoretical coupling coefficient. Because of the current level of manufacturing control in microfabrication over the device dimensions and residual stress, it is difficult to secure an intended safety margin on the bias voltage to avoid collapse on all the array elements [30]. Another limitation is the requirement of two different designs of cMUTs to transmit and receive signals [59-61, 63, 64]. To increase the sensitivity for a receiving element, the gap in the membrane should be small, while the gap in the membrane for a transmitting element should be big enough to allow large deflection that generates strong sound wave [30]. This can cause complexity in the fabrication on cMUTs on the same wafer so that the low tolerance of the device fabrication could induce high manufacturing cost.

2.2.3 Piezoelectric Micromachined Ultrasonic Transducers

Piezoelectric thin film structures have found a wide variety of applications in emerging technologies. For electromechanical applications, lead zirconate titanate (PZT) film is commonly used as the actuating or sensing component in these structures due to its high piezoelectric constant, high energy density, and large electrical-mechanical coupling coefficient [65]. The integration of PZT thin films on silicon substrates is an important task. pMUT uses a micromachined multilayered membrane resonator, typically on the order of 10's of micrometers as a sound radiating element [29-31, 66] as shown in Figure 2-7. Unlike the traditional PZT ceramic based ultrasonic transducers, whose operating frequencies are controlled by the dimensions and properties of the PZT ceramic, the PZT thin film in pMUT is mainly used as a component to drive the membranes into vibration while the dimensions and properties of the membrane mainly control the operating frequencies. Thus, pMUTs offer a more flexible and innovative approach to the development of advanced ultrasonic transducers compared to the conventional ultrasonic transducers. Improvement in pMUTs performance can be achieved through optimization in material and design variables. Research work focusing on material optimization [67] and FEA analysis [30, 31] was reported previously.

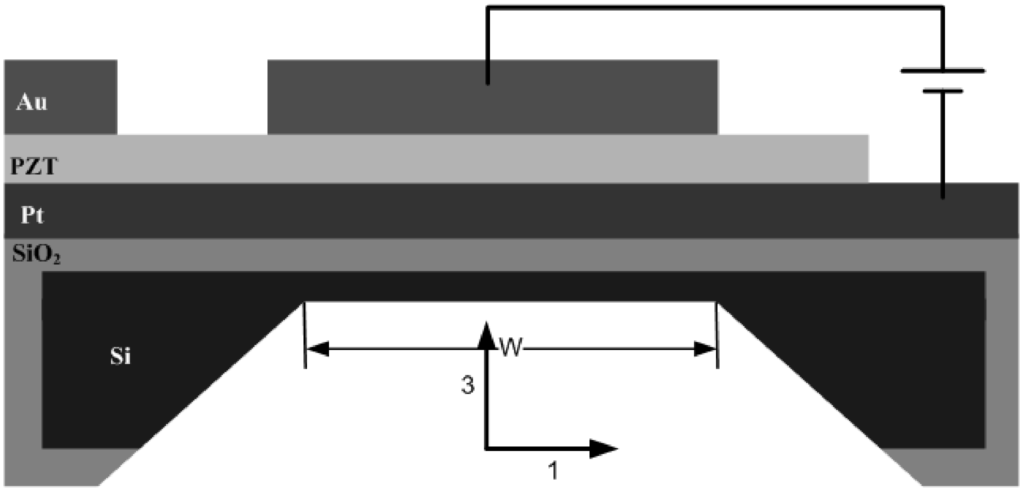

Figure 2-7: Schematic diagram of single pMUT.

pMUTs have the benefits of cMUTs such as integration of micro-fabrication technology, easy fabrication of array type transducers, and application to forward viewing endoscope. In addition to the advantages related to micromachining, pMUTs have other advantages compared to cMUTs. They have a higher capacitance so that the effect of parasitic capacitance on the coupling coefficient and sensitivity is less significant compared to cMUTs [30, 31]. They are not as sensitive as cMUTs to the fabrication accuracy and inconsistencies among the array elements. Because of these inherent advantages, pMUTs can overcome the limitations of conventional piezoelectric transducers.

2.3 Numerical Tools for MEMS

As MEMS market is rapidly expanding and MEMS research is being performed by many research groups, a design methodology for modeling and predicting the performance of MEMS devices is critically needed. The methodology can be in the form of analytical model or software. The former provides a simpler and quicker way to gain some insights into the performance of pMUTs while the latter can be used to study the details of the devices. Since late 1990s, there has been commercial software developed towards the MEMS applications. Examples are ANSYS [68], FEMLAB [69], ABAQUS [70], IntelliSuite [71], CFD-ACE+ [72], MEMulator [73], etc. As common to most of the commercial tools, they in general lack the flexibility to address many specific issues that may be encountered in the development of new devices. Thus there is still a need for continuous development of design methodology along with the development of hardware.

CHAPTER 3

3 Fabrication of pMUTs

3.1 Silicon Wafer as a MEMS Substrate

Single-crystal silicon wafers are widely used as substrate materials in MEMS fabrication because of their excellent mechanical and thermal properties. In addition to the material properties, MEMS structure can be integrated into electronic circuit on the same silicon wafer. Young's modulus of silicon is similar to Young's modulus of steel, which is about 2×10^5 MPa and silicon is as light as aluminum [54]. Silicon also has lower thermal expansion coefficient (TEC) and higher melting point compared to other structural materials.

The mechanical properties of silicon wafers are orientation-dependent [55]. This orientation-dependency affects the micromachining of silicon substrate and the wafers have indications of their crystal structure by flats as shown in Figure 3-1. In our applications, we use (100) silicon wafer because Ethylene Diamine Pyrochatechol (EDP) is used for anisotropic wet etching to fabricate membranes on the silicon wafer.

Recently, silicon-on-insulator (SOI) wafers have been extensively used in MEMS and they were introduced to reduce the conductivity of silicon wafer even at a temperature above 125^{o}C at the first time. The schematic view of SOI wafer is shown in Figure 3-2. SOI wafers have other advantages in micromachining as listed here. No additional etch stop is required since SiO_2 layer is buried in the wafer. During anisotropic wet etching using silicon wafers, the thickness of membranes is controlled by the diffusion time for etch stop such as boron.

However, it is easier to control the thickness of the membranes using wet and dry etching with SOI wafers because SOI wafers with required silicon layer thickness on the buried SiO_2 layer are available from venders. It is also expected to reduce the residual stress in the membrane after fabrication since diffusion process is not required. However, SOI wafers are more expansive compared to silicon wafers.

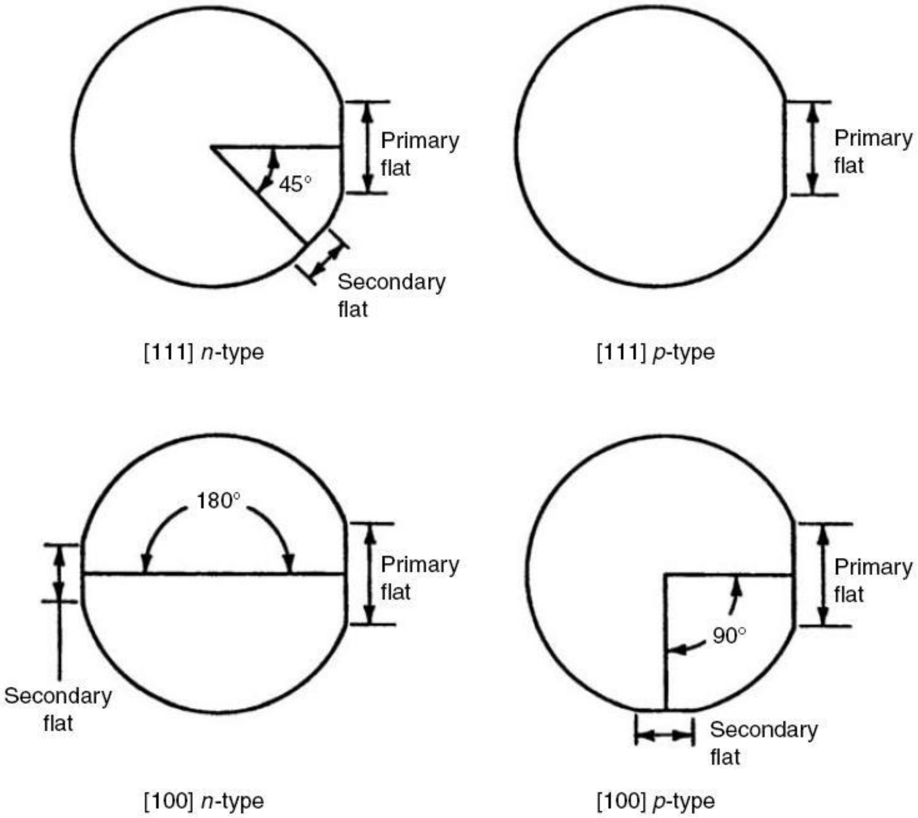

Figure 3-1: Primary and secondary flats on silicon wafers [74].

Figure 3-2: Schematic view of SOI wafer.

3.2 Furnace Processes

3.2.1 High Temperature Oxidation

High temperature oxidation (HTO) of bare silicon wafers is the first step in fabrication of pMUTs. Silicon wafers were subjected to high temperature wet oxidation at 1050°C in a mixed oxygen and nitrogen environment to grow thick SiO_2 layer. A 45 minutes ramp to 1050°C was followed by 80 minutes soak time to grow 500nm SiO_2 layer on silicon. Oxide layer on top side (where membranes will be fabricated) of the wafer was then stripped using a commercially available buffered oxide etchant (BOE) solution of HF, NH_4F, and H_2O for 10 minutes, while the backside of the wafer was protected using semiconductor tape. A schematic view of silicon wafer after HOT and BOE is shown in Figure 3-3.

Figure 3-3: Silicon wafer after BOE.

3.2.2 Boron Diffusion

Boron-doped silicon layer is an effective etch stop for anisotropic silicon wet etching to fabricate membranes. Solid boron disks are used as sources of boron for the diffusion process on the bare silicon side at 1125°C for 110 minutes to result in 2.3μm depth of boron doped silicon layer. The diffusion on the backside was blocked by the oxide layer retained there after BOE. Boron diffusion also results in borosilicate glass formation on the entire surface of wafer and it was removed with etching in BOE for 20 minutes and Figure 3-4 illustrate the wafer after this step.

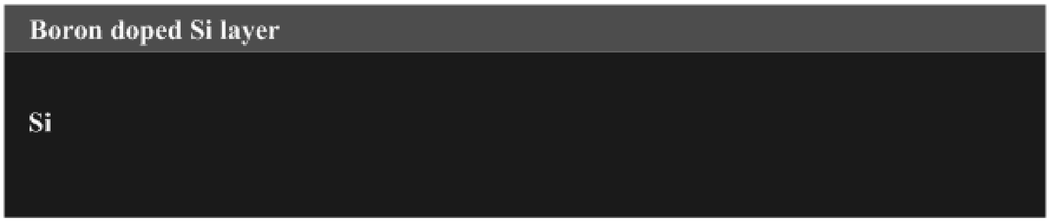

Figure 3-4: Silicon wafer after boron diffusion and BOE.

3.2.3 Low Temperature Oxidation

A sacrificial oxide layer was grown by the first low temperature oxidation (LTO) at 850^{o}C for 2 hours. The object of the first LTO was to remove impurities in the boron surface and provide a clean foundation for the final oxide layer. The sacrificial LTO layer was then removed in BOE for 10 minutes. The wafers are flawlessly clean as pure silicon wafers after BOE. If the wafers were polished in both sides, one needs to be careful to know which side is the boron doped side since both sides look the same. The way to identify which side is boron doped is by dipping the wafers into DI water. The boron doped side is more hydrophilic and pure silicon side is more hydrophobic in a relative sense. Final LTO layer is grown for 2.5 hours after removing the sacrificial oxide layer at the same condition as the first LTO. This final oxide layer will be used to make etch mask (silicon windows) for EDP etching.

3.3 Membrane Fabrication

3.3.1 Backside Mask Design and Photolithography

To create the silicon windows on the backside of the wafers, a template mask was used. The mask was designed using CorelDRAW and the dimensions of the slots in the mask had to be bigger than the actual membrane size to accommodate the 54.7^o angle between the (100) and (111) etching directions and thickness of the wafer. Positive photolithography was used to make pattern on the back side of the wafers along with the designed template mask. Hexamethyldisilazane (HMDS) was applied on the wafer and spun for 30 seconds at 3,000 rpm, which will be an adhesion layer for photoresist. A photoresist (AZ5214) was spun for 30 seconds at 3,000 rpm and the wafer was soft baked for one minute on an 110^{o}C hotplate. The back side of the wafer was then exposed to ultraviolet (UV) light with desired mask for 12 seconds. AZ400K was mixed with water (H_2O:AZ400K = 4:1) to make developer and the wafer was developed in this developer for a minute with light agitation. Top side of the wafer (boron doped side) was covered by semiconductor tape to protect the SiO_2 layer on this side when the wafer was dipped in BOE for five minutes to make etch mask on the back side of final oxide layer. After BOE, the wafer was cleaned with acetone, isopropyl alcohol (IPA), and DI water to remove all the left photoresist. A schematic view of the wafer after photolithography is given in Figure 3-5.

Figure 3-5: Silicon wafer after pattern etch mask for EDP etching.

3.3.2 Anisotropic Silicon Etching

After opening silicon windows on the backside of the wafer using positive photolithography, anisotropic wet etching is required to fabricate silicon membranes. The etching is done using EDP at 110°C for necessary duration depending on the thickness of the wafers. This backside anisotropic etching results in 2μm thick silicon membrane of desired dimensions. A typical etch rate of silicon wafer in (100) direction is 1.25μm/min at 115°C and the etch rate ratio between (100) and (111) directions is 35 at the same temperature [74]. SiO_2 layer from final LTO is used as an etch mask because its etch rate is much slower than silicon. The ratio of etch rates of Si and SiO_2 could be as large as 5000:1 (74). The boron doped Si layer is the etch stop for EDP anisotropic Si etching. A schematic view of a membrane after EDP etching is shown in Figure 3-6 and a scanning electron microscope (SEM) image of membranes after EDP is given in Figure 3-7.

Figure 3-6: Schematic view of a fabricated membrane after EDP etching.

EDP etching must be done in a fume hood and mixing of the chemicals should be done with extreme caution because the chemicals in EDP are harmful. It was reported that ethylenediamine can cause allergic respiratory sensitization and pyrocathechol is described as a toxic corrosive material [57, 74]. Since the solution is optically dense, it is difficult if not impossible to check the progress of the etching while the wafers are in the EDP solution. EDP solution ages quickly and its color turns to red-brown as it aged [57, 74]. Therefore, used EDP solution should be properly dumped after etching 15 to 20 wafers or after certain period of time; if it is the time to replace the old EDP solution to new batch, one can see much of precipitation in the solution when the solution is in a room temperature.

After EDP etching, the wafers are removed from the EDP container and dipped in DI water as soon as possible to avoid marks on the wafer surface. The wafers need to be taken out from the DI water one by one and rinsed with acetone-IPA-acetone-IPA-DI water and dried using canned air or nitrogen. The rinsing process is very critical to avoid any water marks on the top side of the wafers.

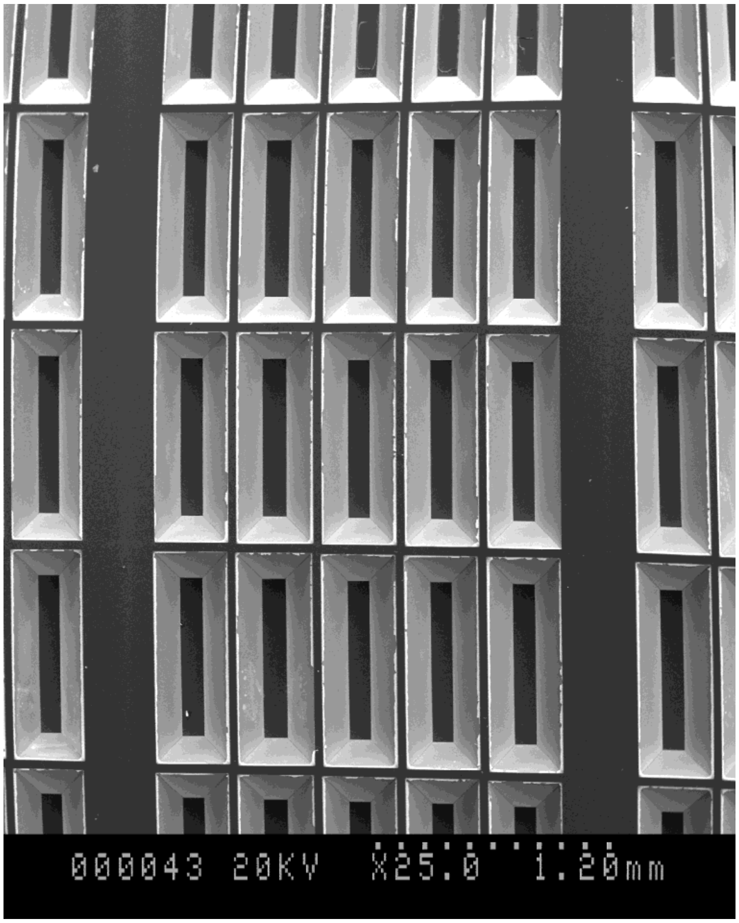

Figure 3-7: SEM image of membrane arrays after EDP.

3.4 Thin Film Deposition

There are three major steps to deposit thin films on the wafer to fabricate pMUTs; platinum sputtering for bottom electrode, PZT deposition for active layer, and gold sputtering for top electrode. Each step will be explained in the following sections.

3.4.1 Sputtering for Bottom Electrode

The DC sputter machine in WSU clearnroom can hold maximum six wafers at a time and two different magnetron source targets can be installed to sputter two different materials in a sequence. The wafers are usually loaded on a rotating wafer holder in the chamber. The chamber is closed and pumping down is done until the pressure reaches at least 1×10^{-6} Torr. The usual working pressure is 9×10^{-7} Torr and it takes 8 to 12 hours and filling nitrogen in the sputter machine helps to speed up the pumping down process. Ti is sputtered as an adhesive layer between SiO_2 and platinum for 3 minutes and 15 seconds at 1.6 mTorr and 0.4 ampere. Platinum layer is sputtered as a bottom layer for 19 minutes and 46 seconds for the thickness of 175nm or for 22 minutes and 35 seconds for the thickness of 200nm at 11 mTorr and 60 watts. In both cases, pre-sputtering for 2 minutes with the shutter closed is done to remove any possible impurities on the surfaces of targets. Between Ti and Pt sputtering, at least 30 seconds pumping down should be done to remove all the Ti particles in the chamber before Pt sputtering. After Pt sputtering, 10 minute annealing at 650^{o}C is required to avoid delamination between SiO_2 and platinum layers. A side view of a membrane is given in Figure 3-8 and the Ti layer has been neglected in the figure since its thickness is relatively small compared to other layers.

Figure 3-8: A schematic view after sputtering Pt layer.

3.4.2 PZT Thin Film Deposition

PZT precursor solution is used to deposit PZT thin film on a platinized wafer. 0.5M metallorganic precursor solution is prepared via sol-gel method using 2-methoxy ethanol (2MOE) as a solvent and lead acetate tri-hydrate, titanium isopropoxide, zirconium n-propoxide as the starting materials. Distillation and refluxing steps are done in the preparation of PZT solution. The composition of PZT precursor solution can be varied and additives could be added to improve certain material properties [75]. Further details of the solution preparation and material optimization using dopants can be found in Refs. [37, 67, 76].

First, PZT solution is deposited on the platinized wafer using a syringe with 0.2µm pore filter starting from edge to center of the wafer. Prior to the deposition of PZT precoursor solution, it is recommended to clean the surface of the wafer using canned air or nitrogen gas to remove any dust or particles on the wafer. Spin coating of PZT layer was done by spin-coater at 3000 rpm for 30 seconds with wafer holder. Prior to the spin coating, the spin-coater must be setup for this condition. The wafer then transferred on a hot plate at 375^{o}C for 2 minutes for pyrolysis to remove organics. Before and after pyrolysis, the wafer was slowly transferred to and removed from the hot plate for about 30 seconds to reduce any possible thermal shock. The wafer was then left in a wafer carrier for more than 1 minute to cool it down at room temperature. Three to four layers of PZT layers were deposited before crystallization at 650°C for 10 minutes. Twelve layers of PZT layers were required to get 1μm thick PZT thin film by three to four times of crystallization including the final crystallization at 700°C. Before deposition of PZT solution on the wafer after each crystallization process, the filter and needle on the syringe are changed to avoid any possible solidified PZT particle in the filter and needle to improve the film quality. A schematic diagram of a membrane after PZT deposition is shown in Figure 3-9.

Figure 3-9: A schematic view of a membrane after PZT deposition.

3.4.3 Sputtering for Top Electrode

Top electrode is DC sputtered by the same procedures as explained in section 3.4.1 using TiW and Au instead of Ti and Pt. 5nm of TiW which serves as adhesive layer at 100 watts and 200nm of Au layer which serves as the top electrode at 75 watts are sputtered for 51 seconds and 15 minutes 28 seconds, respectively. Both of the sputtering are done at 7.5 mTorr. It is always better to start the sputter machine for top electrode right after the final crystallization of PZT and blow canned air before installing the wafers in the sputter machine to remove any possible particles. If there is delay between the final crystallization and top electrode sputtering, it is recommended to rinse the wafers and dry on a hot plate at 110^{o}C prior to placing the wafers in the sputter machine. Figure 3-10 is given below after top electrode sputtering and the TiW layer is neglected by the same reason as Ti layer in the bottom electrode.

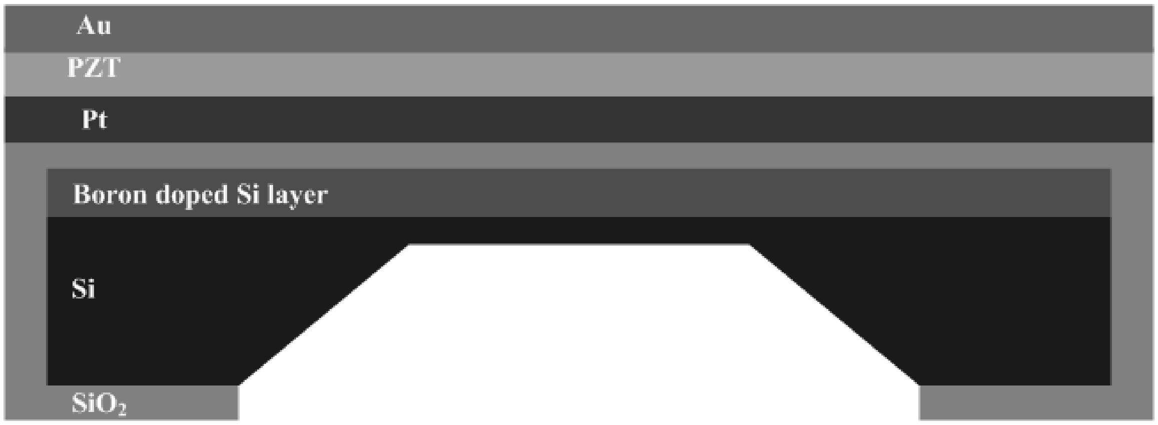

Figure 3-10: A schematic view of a membrane after top electrode sputtering.

3.5 Patterning Top Electrode and PZT film

In order to pattern the top electrode, positive photolithography is used as explained in section 3.3.1. Special care needs to be taken to pattern the top electrode since the resolution of top electrode mask is usually finer and the design is more complex compared to the back side mask. Alignment of the top electrode mask is very critical for the performance of the devices so that it can save times if one checks the alignment after developing in diluted AZ400K. It is much easier doing photolithography several times until he/she gets good alignment than running sputter machine again after unacceptable gold etching.

After developing the photoresist in diluted AZ400K, exposed gold is then etched away using TFA gold etchant (Transene Company, Inc., MA) for 2 minutes and DI water is used to clean the wafer. The wafer is dried and TiW layer is removed using 30% hydrogen peroxide in

DI water for 40 seconds. The wafer needs to be rinsed with acetone, IPA, acetone, IPA, and DI water to remove the left photoresist and clean the wafer prior to patterning PZT thin film.

Patterning of PZT layer is required to open bottom (Pt) electrode. The process is very similar compared to the top electrode pattering except dipping the wafers in a PZT etchant after developing the photoresist in AZ400K. PZT was etched for about 5 minutes or until the shinny Pt surface is exposed. Again, the wafer needs to be rinsed to remove the photoresist and clean it. A side view of the finished pMUT is shown in Figure 2-7.

CHAPTER 4

4 Characterization of pMUTs

Several different designs of single element and array type pMUTs are fabricated following the fabrication process in the previous section. There are three major characterization methods for pMUTs such as ferroelectric, impedance, and acoustic characterizations. Ferroelectric characterization is mainly done by Precision workstation ferroelectric tester (Radiant Technologies, NM) to characterize the properties of PZT thin film on the membrane. The electrical impedance is measured with an impedance analyzer and impedance probe kit (Agilent Technologies, 4294A Precision Impedance Analyzer, 42941A Impedance Probe Kit) to understand the electromechanical behavior of single element pMUT. Finally, the acoustic test can be done by pulse-echo testing with pulser/receiver or microphone to study the characteristics of single or array pMUTs as ultrasound transducers in a medium which is usually water. The details of each characterization are explained in the following sections.

4.1 Ferroelectric Measurement

Ferroelectric measurement is the measurement of polarization in a piezoelectric material under an applied electric field. An example of polarization measurements is shown in Figure 4-1 as function of applied voltage and it is called ferroelectric hysteresis loop. In this figure, saturation polarization, remnant polarization, and coercive electric field were measured for a single element pMUT by Precision workstation ferroelectric tester to test the ferroelectric properties of 0.7µm thickness of PZT thin film.

Figure 4-2 shows top electrode design with the corresponding geometrical design parameters. Membrane width and top electrode width are simultaneously varied as shown in Table 4-1 to Table 4-3 to characterize the properties of PZT thin film. Corresponding to each membrane width, four electrode widths were studied. The length of these membranes remains constant and they are at least in the ratio of 1:10 as membrane width (*W*) to length (*L*). Therefore, the length for 60 and 90µm width membranes were maintained at 1000µm and for 120µm width membrane at 1200µm. Top electrode length (*h*) was also taken as a constant as 900µm for 60 and 90µm membranes and 1100µm for 1200µm membranes.

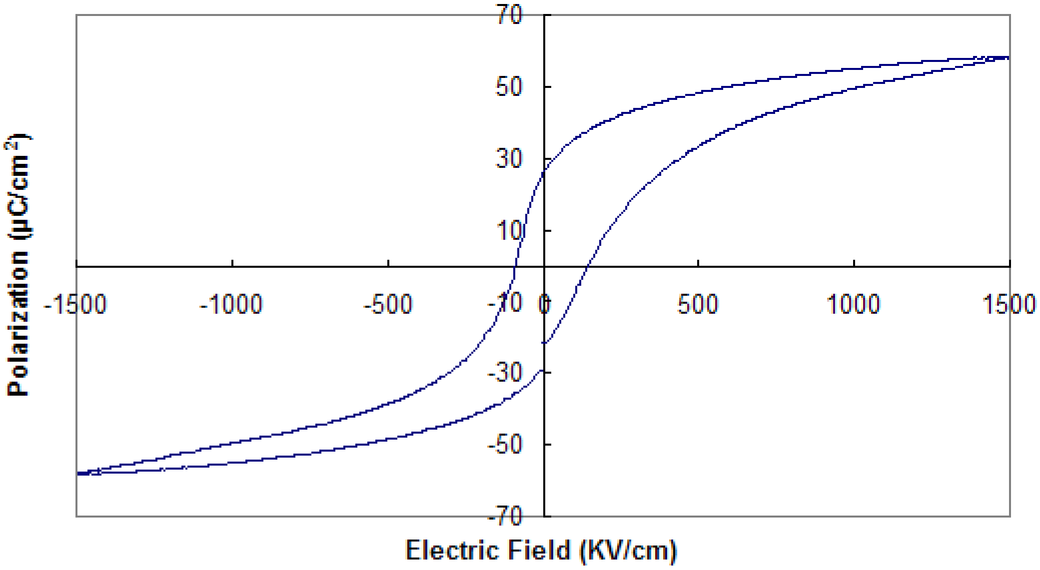

Figure 4-1: Polarization behavior of the 52/48 PZT thin film.

In Figure 4-1, the electric field was applied from 0 to about 1500KV/cm. As the electric field is increased, the polarization in the film is increased as almost linearly and it is saturated at about 1500KV/cm. During this process, randomly oriented dipoles are aligned in the direction of applied electric filed. When all the dipoles are aligned in one direction, it is called saturation polarization (*Ps*). After this point, the field is reduced until 0 KV/cm and the polarization at this moment is called remnant polarization (*Pr*). From this point, the field is decreased more until the film is saturated (negative saturation) in the reversed direction compared to the previous saturation. In this case, the saturation polarization is about 55μC/cm^2 and the remnant polarization is about 25μC/cm^2.

Saturation polarization, remnant polarization, and coercive electric field for each design are listed in Table 4-1 to Table 4-3. As can be seen in Table 4-1 to Table 4-3, the results are uniform for all designs and ascertained the quality of the deposited PZT thin film.

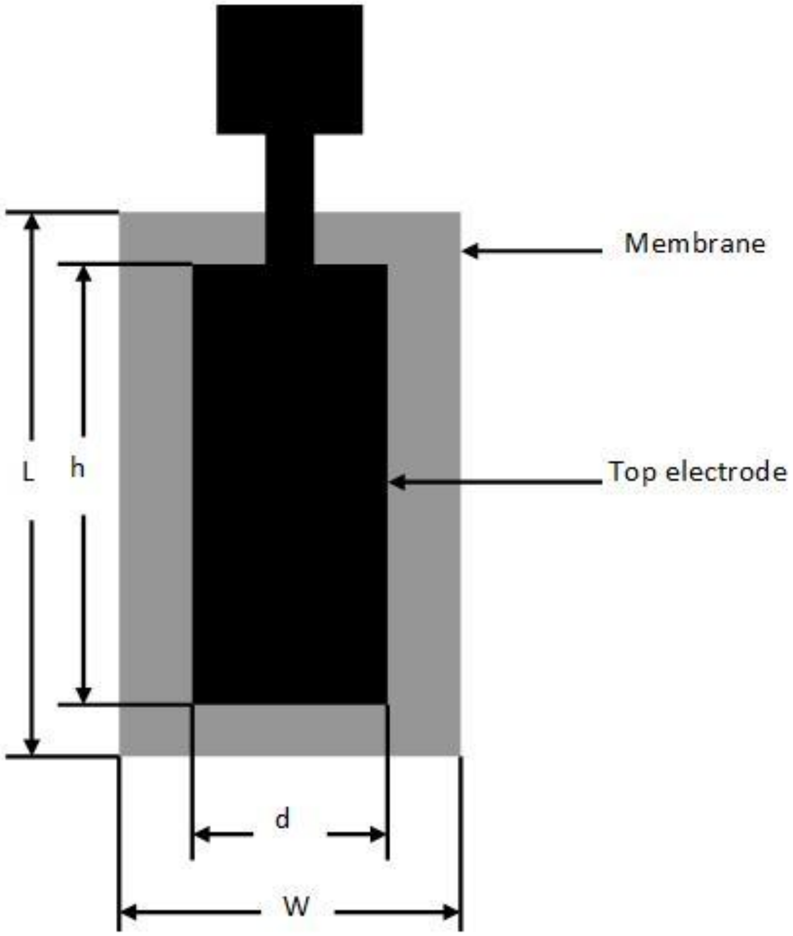

Figure 4-2: Schematic details of design with respective variables.

Top Electrode Width (μm)	Saturation Polarization ($\mu C/cm^2$)	Remnant Polarization ($\mu C/cm^2$)	Coercive Field (KV/cm)
110	55.46	22.91	169.1
120	55.59	22.81	171.0
130	56.05	22.47	149.6
140	56.67	22.27	132.4

Table 4-1: Saturation polarization, remnant polarization, and coercive field for 120μm by 1200μm membranes.

Top Electrode Width (μm)	Saturation Polarization ($\mu C/cm^2$)	Remnant Polarization ($\mu C/cm^2$)	Coercive Field (KV/cm)
80	55.41	23.75	178.4
90	58.02	25.85	145.2
100	55.99	23.60	169.6
110	55.45	22.85	159.7

Table 4-2: Saturation polarization, remnant polarization, and coercive field for 90μm by 1000μm membranes.

Top Electrode Width (μm)	Saturation Polarization ($\mu C/cm^2$)	Remnant Polarization ($\mu C/cm^2$)	Coercive Field (KV/cm)
50	57.92	28.33	258.8
60	56.50	27.01	261.7
70	57.06	27.43	255.8
80	56.47	27.08	259.2

Table 4-3: Saturation polarization, remnant polarization, and coercive field for 60μm by 1000μm membranes.

4.2 Electrical Impedance Measurement

4.2.1 Impedance Measurement and Equivalent Circuit Analysis

Characterization of the fabricated single element pMUTs can be done by electrical impedance measurement combined with an equivalent circuit analysis. The main objectives of the impedance measurement are finding the first mode resonance frequency and measuring the magnitude of electrical impedance and its phase angle. The sample is elevated in the air by 1cm from the surface of the probe station and the measurement is done in the air. A typical impedance measurement result is shown in Figure 4-3. The measured data is then used to extract the values of the equivalent circuit components as shown in Figure 4-4 for further investigation of the fabricated pMTUs. The equivalent circuit represents the behavior of an ultrasound transducer near its resonance frequency [33, 75, 77]. It has four components, C_0, C_1, L_1, and R_1. C_0 represents the parallel capacitance of the structure in the absence of piezoelectricity, and L_1 (the motional inductance), R_1 (resistance), and C_1 (capacitance) represent the inertia mass, internal damping, and stiffness of the transducer, respectively [33, 75, 77].

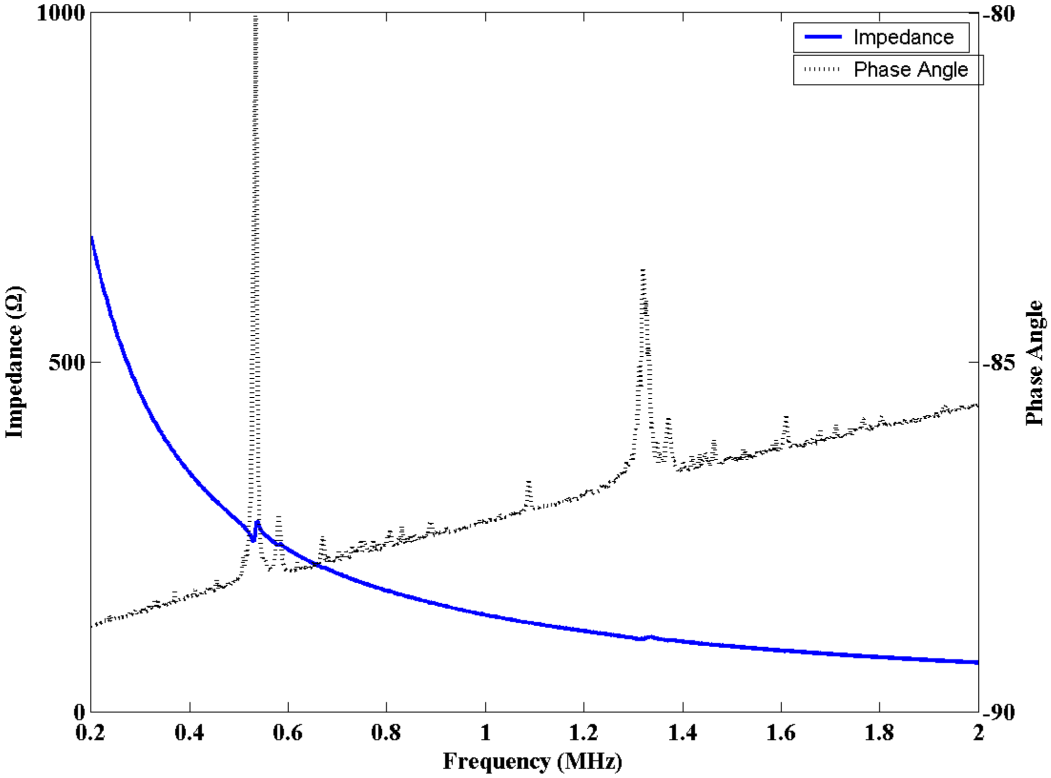

Figure 4-3: Measured impedance magnitude and impedance phase angle.

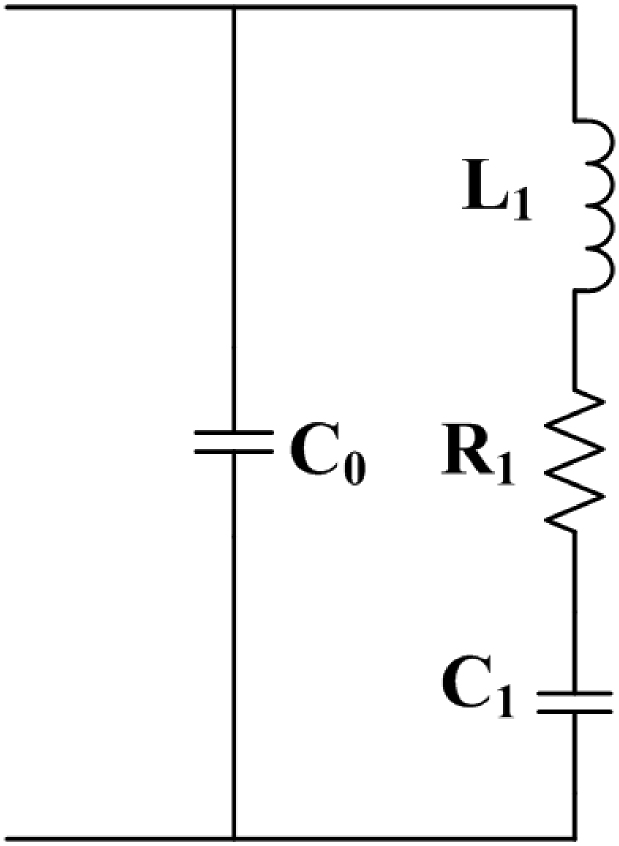

Figure 4-4: Equivalent circuit of electromechanical transducers.

The resonance frequency (f_r), anti-resonance frequency (f_p), and effective coupling coefficient $\left(k_{eff}^2\right)$ of the system are related to the aforementioned circuit parameters through the following relations [33, 75, 77].

$$f_r = \frac{1}{2\pi\sqrt{L_1 C_1}} \tag{4-1}$$

$$f_p = \frac{1}{2\pi}\sqrt{\frac{C_0 + C_1}{C_0 L_1 C_1}} \tag{4-2}$$

$$k_{eff}^2 = \frac{C_1}{C_0 + C_1} = \frac{f_p^2 - f_s^2}{f_p^2} \tag{4-3}$$

Effective coupling coefficient $\left(k_{eff}^{2}\right)$ is defined as the transduced electrical or mechanical energy over the total input energy to the system [33]. Based on this definition, effective coupling coefficient can be calculated using the electric circuit components or resonance and anti-resonance frequencies. Quality factor is defined as a ratio of the total energy stored in the system to the energy lost per cycle due to the damping effects [17, 77]. Higher quality factor (*Qu*) means more stored energy and less lost energy so that the system is expected to have higher efficiency. Quality factor can be calculated using electric circuit components and it is a dimensionless number [77].

$$Qu = \frac{\sqrt{L_1/C_1}}{R_1} \tag{4-4}$$

A typical impedance matching near the first resonance frequency is shown in Figure 4-5. Extraction of the equivalent circuit components is done essentially by curve fitting the equivalent circuit equation to the experimental data. To enhance the self-consistency of the curve fitting results, the fitting was carried out in a systematic manner. C_0 was adjusted based on the overall shape of impedance curve; C_1 and L_1 were mainly based on the experimentally measured resonance frequency, the width of the two peaks (maximum and minimum impedance magnitude peaks) shown in Figure 4-5(a) and the width of impedance phase angle shown in Figure 4-5(b); and R_1 was based on the vertical span of the impedance magnitude and impedance phase angle data. After a set of C_0, C_1, L_1, and R_1 that could match reasonably with the experimental data was identified, an iterative procedure was then used to minimize the variance of the curve fitting results and finalize the values for these parameters.

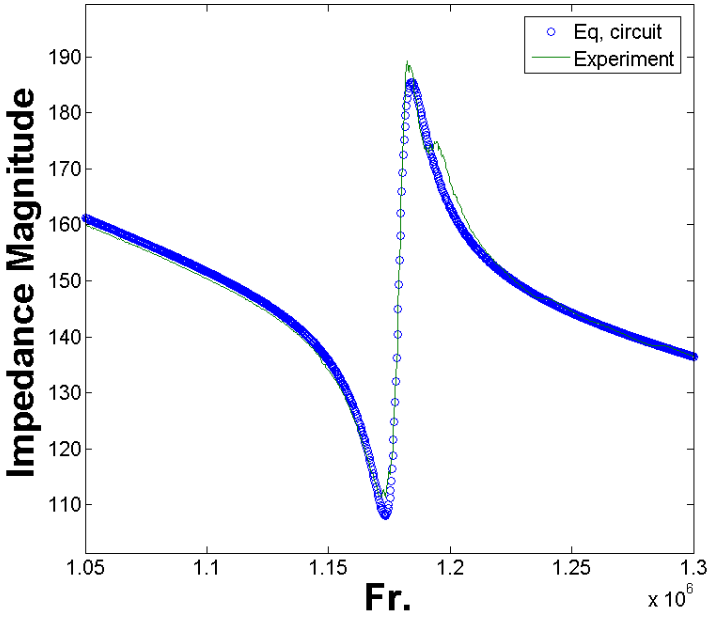

(a)

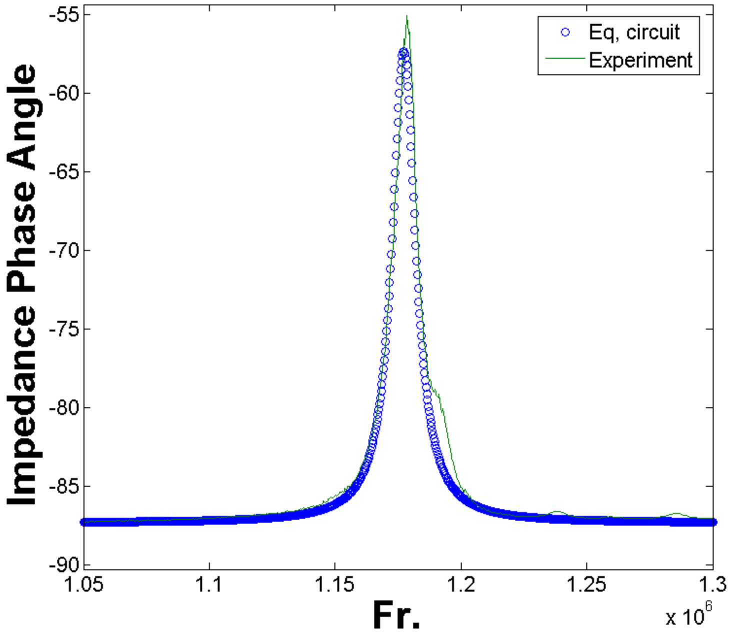

(b)

Figure 4-5: Measured (solid lines) and fitted (symbols) impedance magnitude (a) and impedance phase angle (b).

4.2.2 Fabricated pMUTs Samples

A schematic diagram of the side view and pictures of the fabricated pMUTs from the top side are given in Figure 2-7 and Figure 4-6, respectively. As shown in Figure 4-6, two different general sizes of pMUTs, small and large (in a relative sense), are designed for impedance measurement. The smaller membranes are used to generate relatively higher frequencies and analyzed using equivalent circuit analysis. For the small membranes, as shown in Figure 4-6(a), the widths (W) are varied by 90, 120, 150, and 180μm and the lengths (L) by 860, 1160, 1460, 1760, and 2060μm. The corresponding L/W aspect ratios range from 5 to 23. For the large membranes, the membranes with the square shape (SM) have the side dimensions of 470, 570, 1070, 1570, and 2070μm, respectively, and those with the rectangular shape (RM) have dimensions of 570μm × 1070μm, 570μm × 1570μm, and 570μm × 2070μm, corresponding to L/W aspect ratios of 1.9, 2.8, and 3.6, respectively.

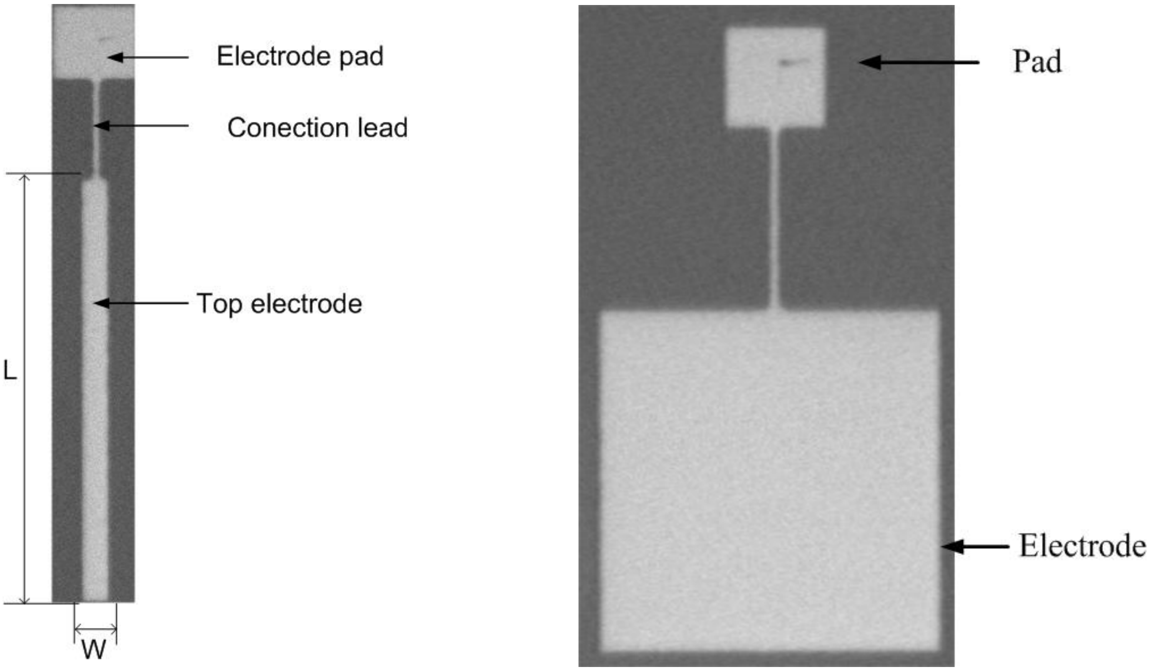

(a) (b)

Figure 4-6: Top view of the pMUT membrane structure; (a) small membrane, (b) large membrane.

The size of the top electrode was slightly smaller than the membrane, i.e. 30µm and 35µm shorter from each side of the membrane for the small and large membranes, respectively. For example, for a 180 by 2060µm small size membrane, the top electrode size is 120 by 2000µm. The corresponding bottom electrode layer is 175 and 200nm thick for small and large membranes, respectively. To apply electric current between the top and bottom electrodes, an electrode pad is placed outside of the membrane and the electrode and electrode pad are connected by connection lead as shown in Figure 4-6. This will avoid breaking of a membrane while applying electricity to the top electrode through the pad and lead using needles or wires. The sizes of electrode pad and connection lead are 300 by 300µm and 30 by 400µm, respectively.

4.2.3 Results

As mentioned earlier, pMUTs with twenty different dimensions were designed in this study for small membranes. For each design, multiple samples, ranging from 9 to 15, were fabricated and tested so that statistically meaningful results could be obtained. The measured median impedance magnitudes for membrane length 860, 1160, 1460, 1760 and 2060µm when the membrane width is 120µm are shown in Figure 4-7 and it tells that the membrane length has little effect on the resonance frequency for small membranes when their length to width ratios is large.

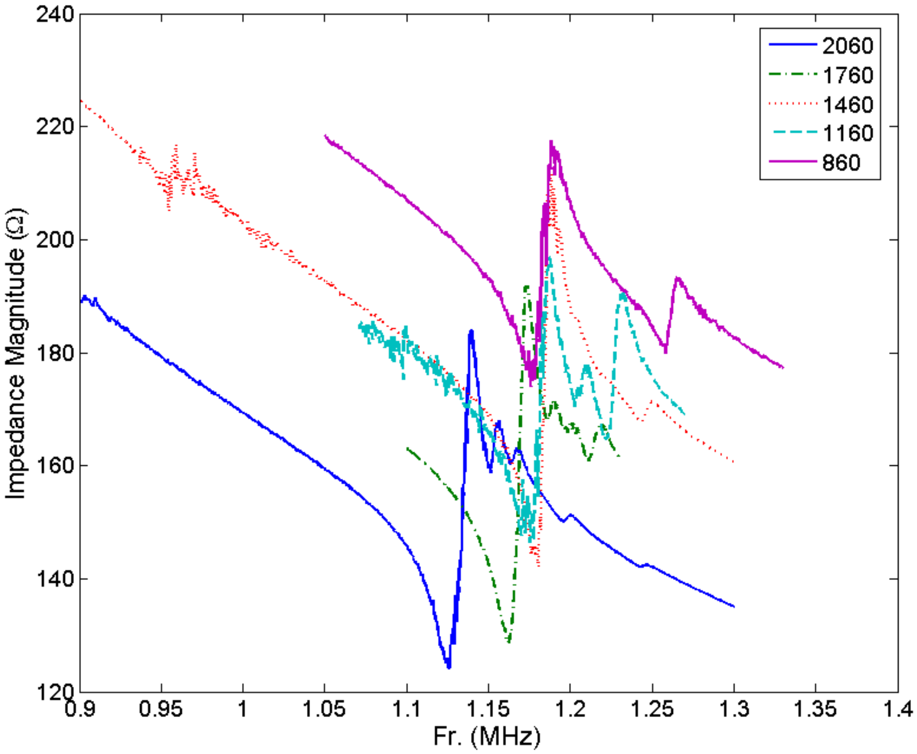

Figure 4-7: Impedance magnitude for each membrane length when the membrane width is 120µm.

Values for inductance (L_1) are shown in Figure 4-8. The symbols represent the mean value and the error bars specify the standard deviations. The data indicates that L_1 appears to be relatively insensitive to the width (W) when $W \leq 150\mu m$, but increase with the width when $W \geq 150\mu m$. The data also show that L_1 decreases with the membrane length for a given width and the decrease of $L1$ correlates with total mass.

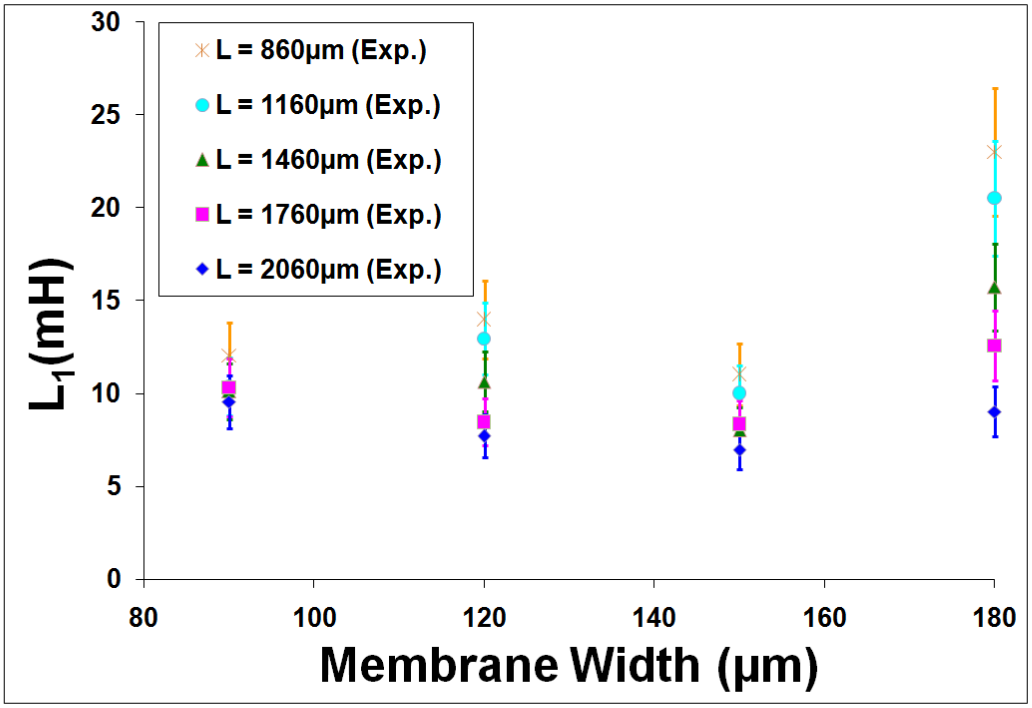

Figure 4-8: Motional inductance (L_1) as a function of membrane dimensions.

The results for C_1 are shown in Figure 4-9. The figure depicts a clear overall trend that C_1 increases with the membrane width. It also indicates that C_1 increases with the length for the membranes whose widths are greater than $90\mu m$.

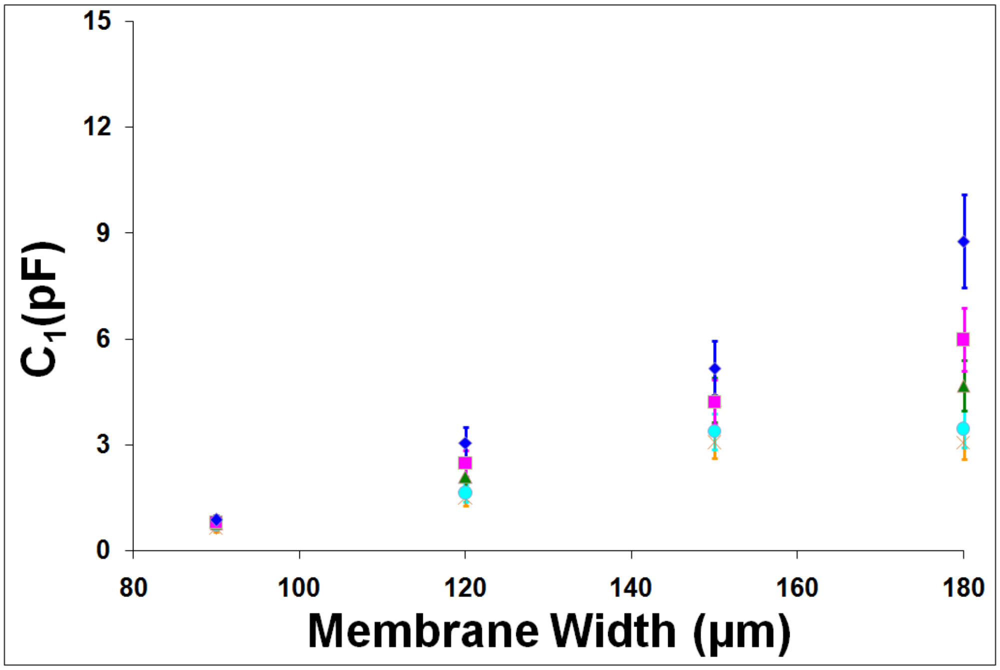

Figure 4-9: Motional capacitance (C_1) as a function of membrane dimensions. See Figure 4-8 for the legends.

Shown in Figure 4-10 and Figure 4-11 are the results for C_0, parallel capacitance before and after considering parasitic capacitance, respectively. Figure 4-10 shows the results directly from the equivalent circuit analysis and Figure 4-11 shows the modified results taking into consideration of the parasitic capacitance. As mentioned earlier and shown in Figure 4-6, an electrode pad was connected to the top electrode on the membrane through a connection lead. The input voltage was applied to the pad, instead of the membrane electrode directly, through a pair of the probes. This prevented the thin membrane from breaking by the mechanical force applied through the needles of probe station. However, the extra electrode areas also induced some parasitic capacitance and diverted some input electric energy. To take the effect of parasitic capacitance into consideration, the C_0 values obtained directly from the equivalent circuit analysis were modified by multiplying them with the ratio of the electrode area to the total area of gold layer which consisted of electrode, connection lead, and electrode pad. The corresponding membrane electrode area ratios ranged from 70% to 19% for the largest and smallest membranes, respectively. Thus, the effect of parasitic capacitance could be quite significant, especially for the smaller membranes. As shown in both Figure 4-10 and Figure 4-11, C_0 increased with both the membrane width and length, similar to what was observed in Figure 4-9 for C_1. However, with the correction of parasitic capacitance, the length dependence became more pronounced as shown in Figure 4-11.

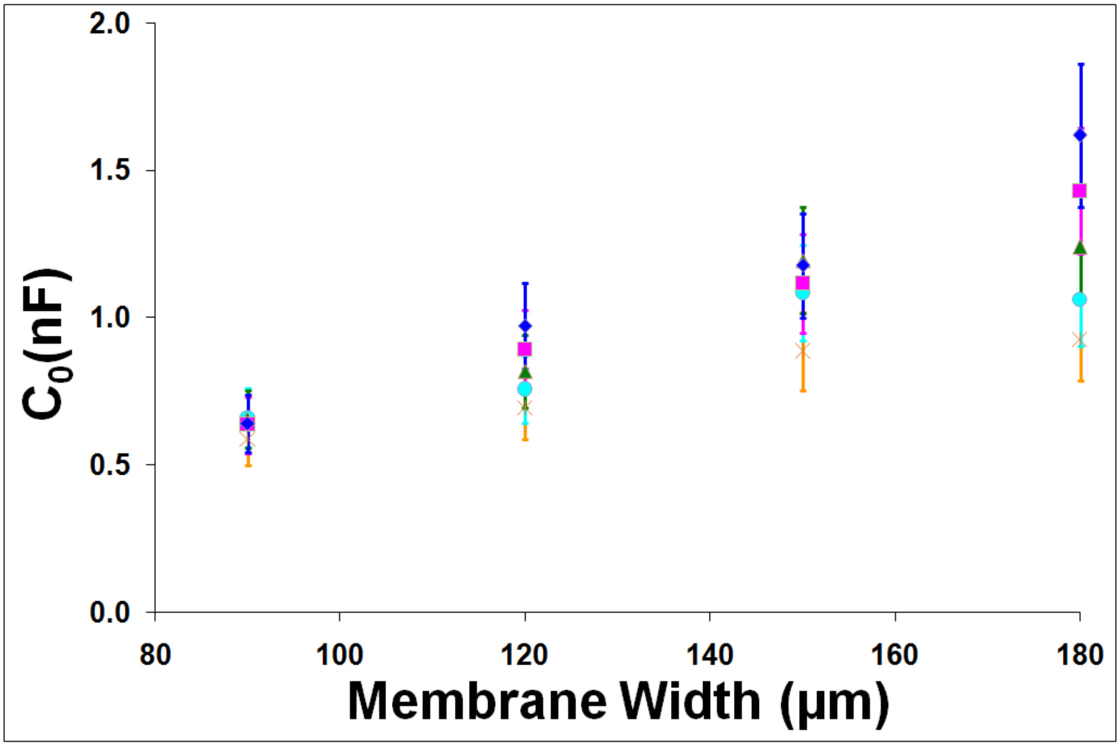

Figure 4-10: Parallel capacitance (C_0) as a function of membrane dimensions before considering parasitic capacitance. See Figure 4-8 for the legends.

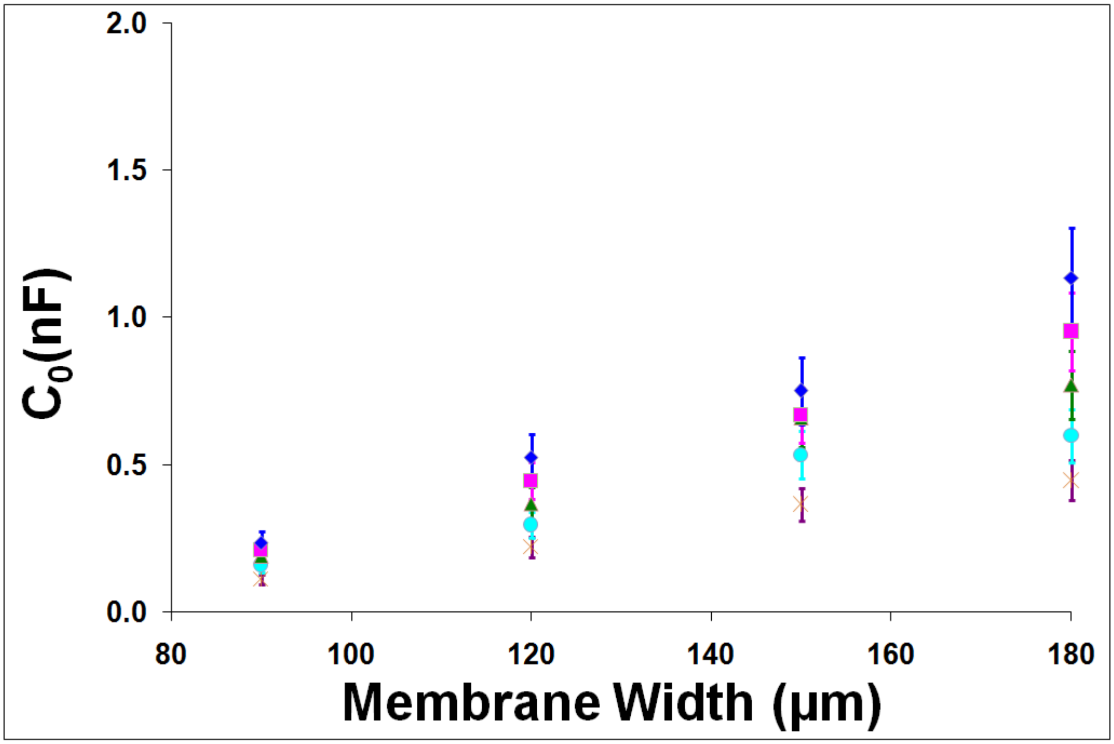

Figure 4-11: Parallel capacitance (C_0) as a function of membrane dimensions after considering parasitic capacitance. See Figure 4-8 for the legends.

The results for R_1 are shown in Figure 4-12. The data do not seem to show a consistent overall trend. Generally speaking, R_1 appears to decrease with the width for $W \leq 150\mu m$ and increase for $W \geq 150\mu m$. There is no clear indication on the length dependence either, except that for a given width, the membrane with the smallest length possesses the largest R_1. R_1 indicates damping effect caused by the outside and inside of the transducer environment such as air damping, material damping, material friction, etc. Analyzing R_1 in a precise way is rather complicate so that it is not further investigated in this study and left as a future work. Therefore, R_1 will not be considered in the following analytical solutions in Chapters 6 and 7.

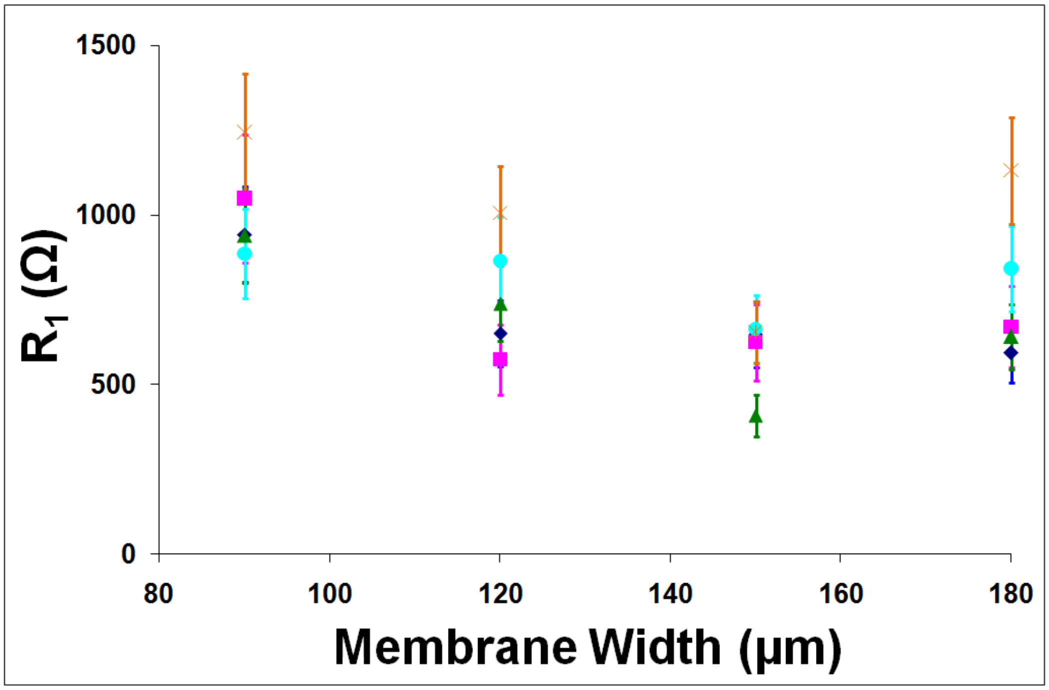

Figure 4-12: Motional resistance (R_1) as a function of membrane dimensions. See Figure 4-8 for the legends.

The results for resonance frequencies ($f_r \approx f_p \approx f_s$) are shown in Figure 4-13. It shows clearly that frequencies decrease with the width, but have no appreciable length dependence. As shown in Figure 4-7, membrane length has little effect on the resonance frequency if length to width ratios are large. The frequencies difference caused by the different membrane length is negligible if one considers the frequency range of pMUT.

The results of effective coupling coefficients $\left(k_{eff}^2\right)$ are displayed in Figure 4-14 and Figure 4-15 before and after considering parasitic capacitance. Without the correction of parasitic capacitance, k_{eff}^2 appeared to increase with both the width and length of the membrane as shown in Figure 4-14. However, with the correction of parasitic capacitance, k_{eff}^2 appeared to increase with the width up to approximately 150µm and then decrease as shown in Figure 4-15.

With respect to the length dependence, there was some pattern in the ordering of mean values of k_{eff}^2 associated with length *L* at each width *W*, although the pattern was not consistent. Finally, the quality factor (*Qu*) as a function of membrane dimensions is shown in Figure 4-16. The figure shows that *Qu* decreases with the width but does not appear to have appreciable and consistent length dependence.

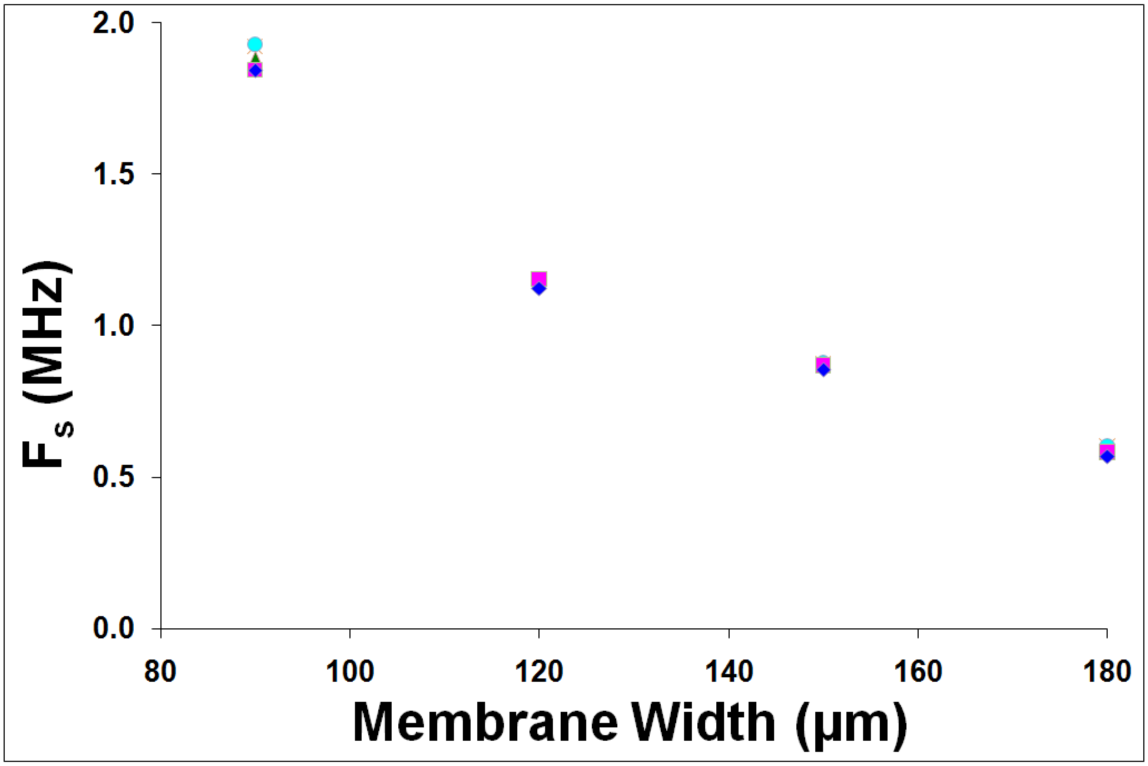

Figure 4-13: Resonance frequency (f_s) as a function of membrane dimensions. See Figure 4-8 for the legends.

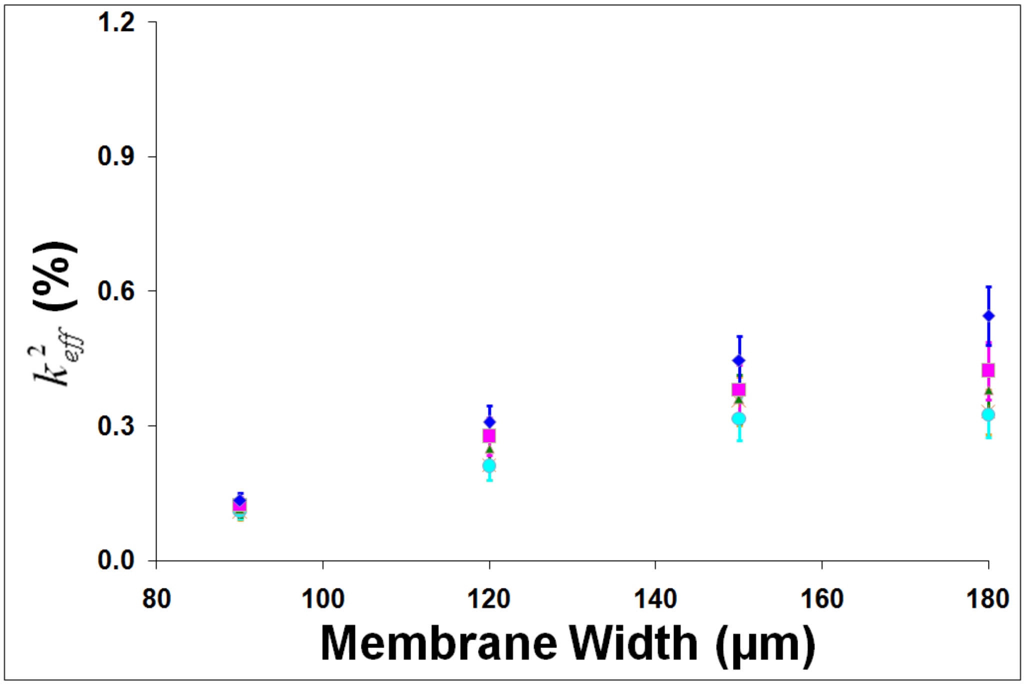

Figure 4-14: Effective coupling coefficient (k_{eff}^2) as a function of membrane dimensions before considering parasitic capacitance. See Figure 4-8 for the legends.

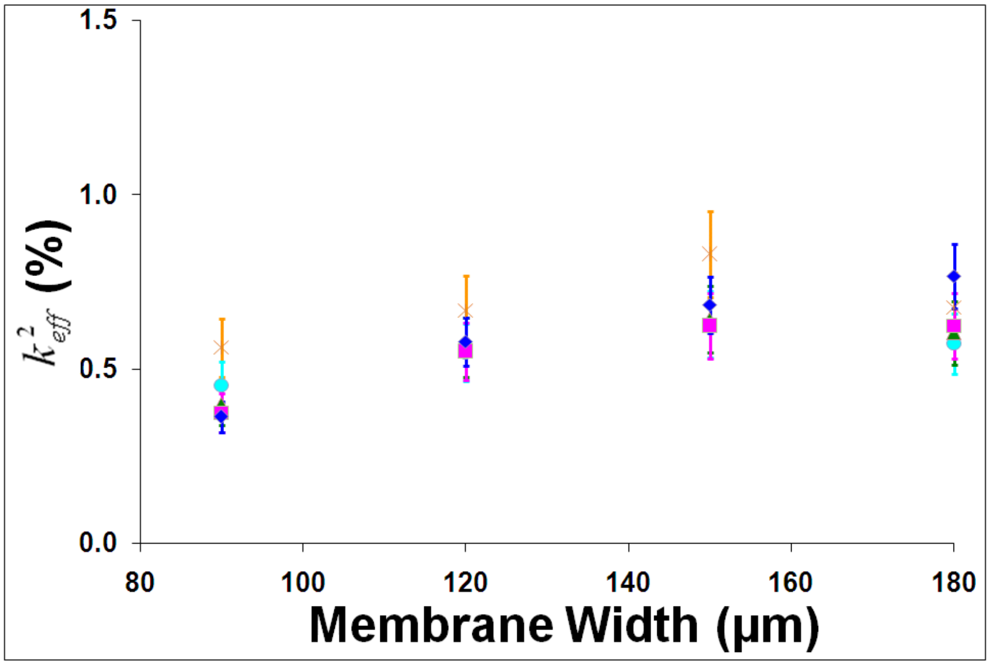

Figure 4-15: Effective coupling coefficient (k_{eff}^2) as a function of membrane dimensions after considering parasitic capacitance. See Figure 4-8 for the legends.

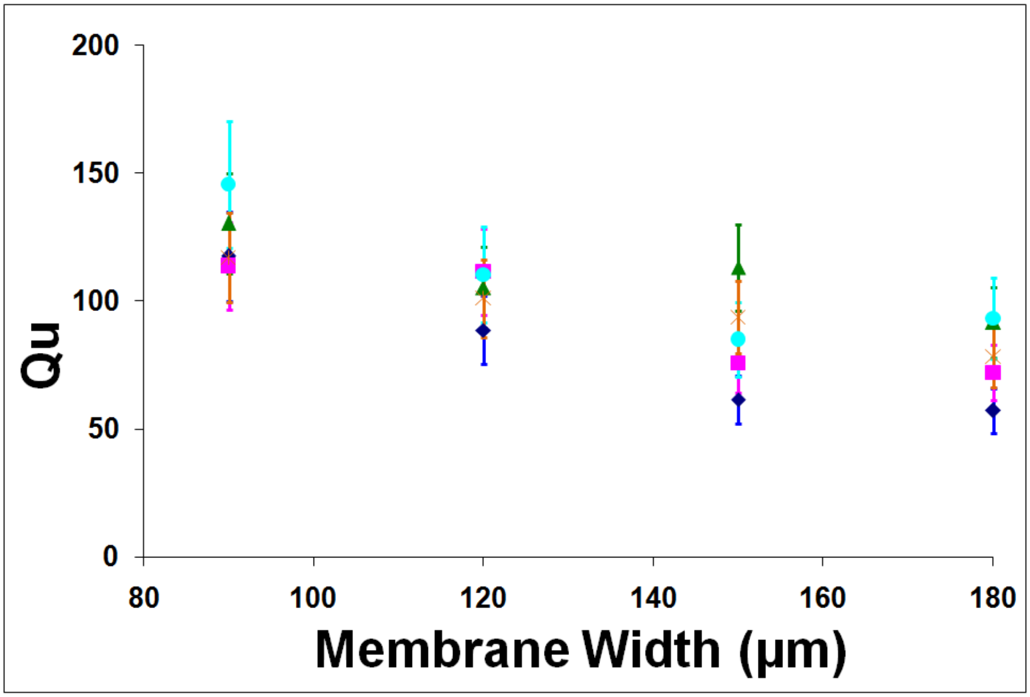

Figure 4-16: Quality factor (*Qu*) as a function of membrane dimensions. See Figure 4-8 for the legends.

For the lager membranes, the same method was used to measure impedance. Only the first resonance frequencies are interested for large membranes because they are used as benchmark for FE models in Chapter 5. The experimental results of smaller and lager membranes will be presented combined with the corresponding modeling data in the following chapters.

4.3 Characterization of Array Type pMUTs

Using the single element pMUTs as the building block, array type pMUTs have also been fabricated as shown in Figure 4-17. For the sample given here, there are five groups of 1D array pMUTs and each group has 5 by 10 elements (total 50 elements). In each group, ten membranes are connected in series and five of the series are connected in parallel. On the left side, there are five opened bottom electrodes (platinum) and five top electrodes (gold) are shown on the right side. Ten through holes are made in the substrate for wire connections.

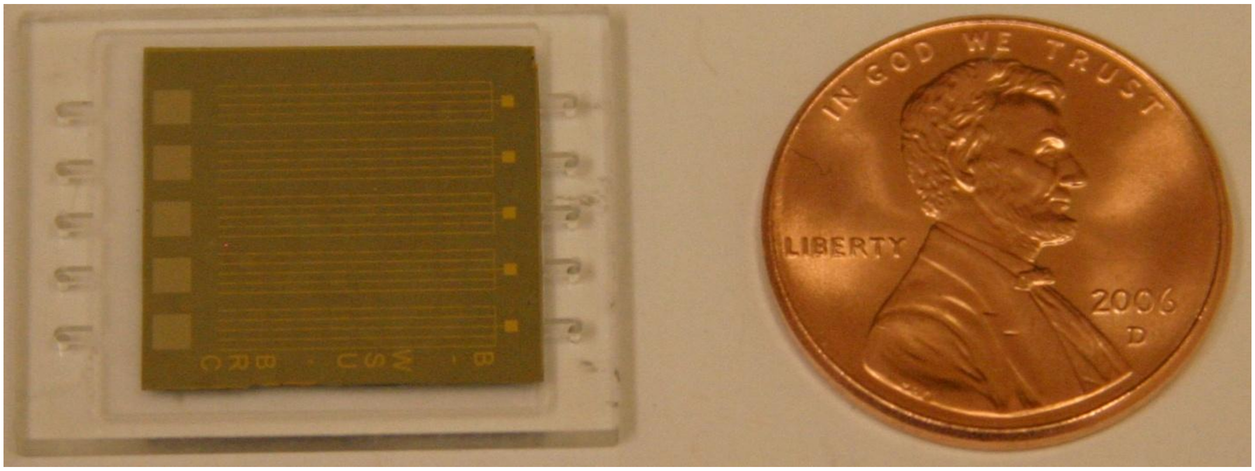

Figure 4-17: Array type pMUTs with five 5 by 10 elements (total 250 elements).

A 5 by 10 array is shown in Figure 4-18 after connecting the top and bottom electrodes with wires. The array is mounted on a Plexiglas substrate and the wires are connected from the backside of the substrate using two through holes. Silver paste was used to connect the wires and there should minimal stress on the silver paste by fixing the wires on the Plexiglas substrate to avoid disconnection later. Silver paste was also used to avoid heating the samples during soldering. In an array type pMUTs, there are many membranes and their top electrodes are connected each other as shown in Figure 4-17 and Figure 4-18. An impedance measurement of this 1D array pMUTs are shown in Figure 4-19(a) and Figure 4-19(b) for wide range and narrow range frequencies, respectively. As can be seen in here, there are mutiple resonance peaks and they are overlapped because of the slightly different resoance frequencies for each membrane. Therefore, understanding the characteristics of array type pMUTs using impedance analyzer or equivalent circuit analysis is very difficult if not impossible. For this reason, an alternative characteristic technique is required to characterize array type pMUTs. The alternative method is acoustic test using pulser/receiver or microphone. The details of acoustic test will be introduced in Chapter 8 as a recommendation for future work.

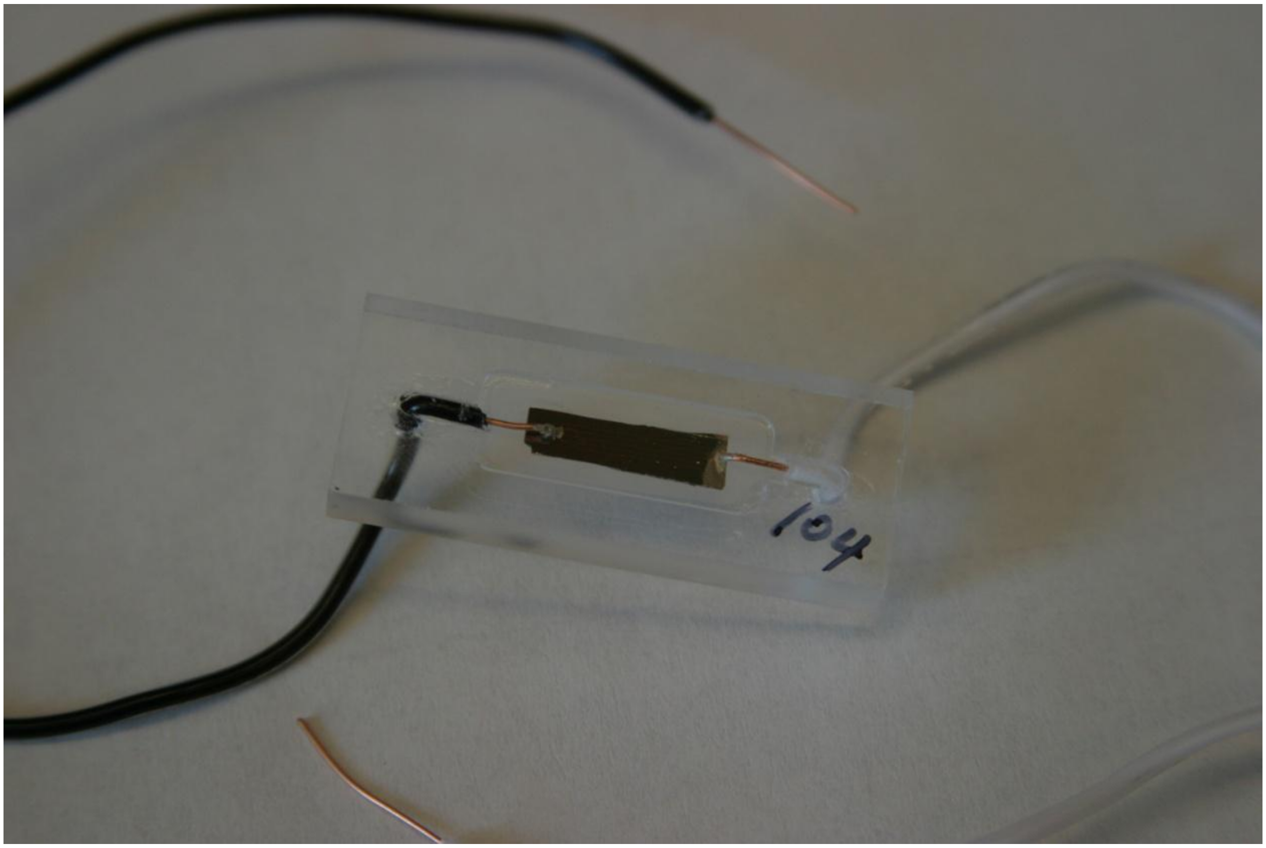

Figure 4-18: An array type pMUTs connected with wires.

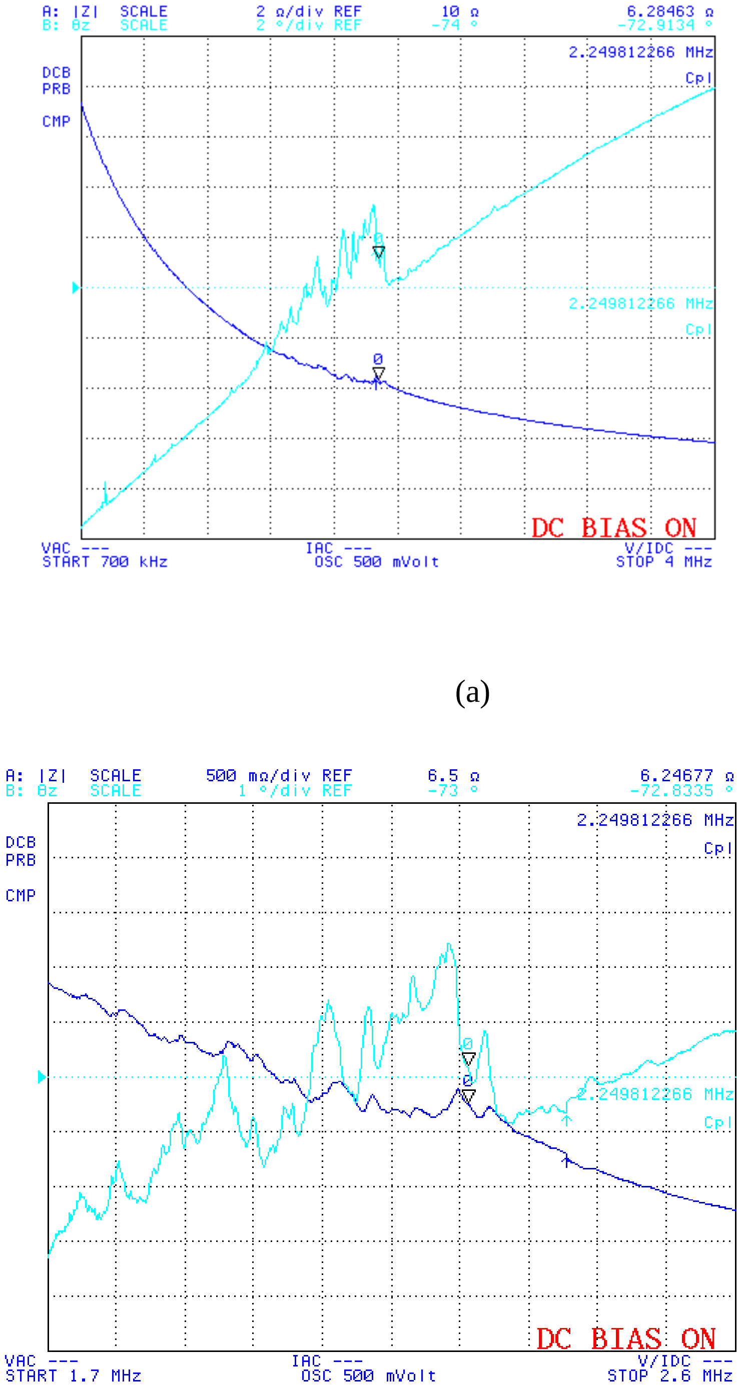

(a)

(b)

Figure 4-19: Impedance measurements of 5 by 10 array type pMUTs.

4.4 Conclusions

Single element and array type pMUTs were fabricated and characterized. Ferroelectric characterization was done by measuring polarization in PZT thin film under an applied electric field. Saturation polarization, remnant polarization, and coercive electric field are measured to understand the characteristics of PZT thin film. The results show the uniformity of PZT thin film for all designs and ascertain the quality of the deposited PZT thin films.

For small membranes, electrical impedance measurement combined with equivalent circuit analysis was used to analyze single element pMUTs. For impedance measurement, multiple samples of pMUTs, ranging from 9 to 15, with twenty different designs were fabricated to obtain statistically meaningful results. The main motivations of the impedance measurement are finding the resonance frequencies and calculating effective coupling coefficients of the devices. To do these, the measured electrical impedance was used to extract the values of the equivalent circuit components. Using the values of equivalent circuit components, resonance frequency, anti-resonance frequency, and effective coupling coefficient of pMUTs were calculated. The resonant frequencies were observed to decrease with the width of the membrane, but have no appreciable length dependence. With the correction of parasitic capacitance, the effective coupling coefficients were observed to increase with the width up to around 150μm and then decrease. The first resonance frequencies of large membranes are measured using an impedance analyzer and used as a benchmark for FE models.

1D array type pMUTs were fabricated based on the single element pMUT design. The fabricated array type pMUTs were mounted on Plexiglas substrates and sealed with air pocket in the back side. There are many membranes in an array type pMUTs and their top electrodes are connected to each other. Because of this, there are mutiple resonance peaks and they are overlapped when electrical impedance was measured with array type pMUTs. Therefore, acoustic test such as pulse-echo test using pulser/receiver or hydrophone is suggested to characterize array type pMUTs. For acoustic test, pMUTs need to be installed in housing for easy of handling and measurement. The acoustic test has not been done and the suggestions will be introduced in Future Work.

CHAPTER 5

5 Finite Element Method for pMUTs

5.1 Introduction

Fabrication of thin film structures is both a time-consuming and costly process. As the design flexibility increases, so does the demand for design software which could provide some good insights into the behavior of the structure before it is fabricated. There is some commercial software available for this purpose such as the ANSYS [66] and the PZFlex [31]. However, as common to most of the commercial software, they in general lack the flexibility to address many specific issues that may be encountered in the development of new devices. Thus, it is advantageous and sometimes necessary to develop a special-purpose code or software as a part of the designing tool for product development.

The development of design software based on finite element method as a part of the overall pMUT project is the objective of this chapter. Specifically in this FE model, the pMUT is treated as a laminated piezoelectric composite plate and the finite element model developed by Reddy [78, 79] was used to gain some insights into the mechanical responses of pMUT. As reviewed by Benjeddou [80], there have been quite a few efforts made towards the development of a finite element code for predicting the electromechanical behavior of laminated piezoelectric composite plates. However, most of these studies were aimed towards the development of the so-called smart engineering structures with the capability of shape change or vibration suppression through the piezoelectric actuator and sensor. These structures are typically in a much larger length scale than that for the pMUT, which is in the order of micrometers. These micro-scale structures could present some new challenges for the relevant design software, but few studies have been done in this area.

Besides numerical investigation, multiple pMUTs with different designs were also fabricated and characterized as explained in Chapters 3 and 4 to compare with the finite element model. The experimental results provide an important benchmark for the FE code development. Furthermore, some unique insights on the mechanical behavior of pMUTs could also be gained by comparing experimental results with numerical simulations. The formulation of the finite element model is summarized in the following section. A comparison between the experimental data and numerical simulation is then carried out, and some conclusions are drawn afterwards.

5.2 Finite Element Formulation for Laminated Composite Plate

As described in the previous chapters, the structure of pMUT is essentially a laminated composite. The finite element code used in this study was based on a combination of the equivalent single-layer theory and the classical laminated plate theory (CLPT) using a rectangular conforming plate element. These theories together with their finite element formulation were well developed by Reddy [78, 79]. In the equivalent single layer theory, the multi-layered composite is transformed into an equivalent single layer. The CLPT was based on the classical Kirchhoff hypothesis for the thin plate such as the transverse normal to mid-surface of the plate remains straight and normal to the mid-surface before and after the deformation, and the plate is inextensible in the normal direction. For composite plates, it is further assumed that the layers are perfectly bonded together, so that there is no delamination between the layers.

Following the above assumptions, the displacement field with respect to a coordinate system shown in Figure 5-1 can be expressed as

$$u(x,y,z,t) = u_0(x,y,t) - z\frac{\partial w_0}{\partial x} \tag{5-1}$$

$$v(x,y,z,t) = v_0(x,y,t) - z\frac{\partial w_0}{\partial y} \tag{5-2}$$

$$w(x,y,z,t) = w_0(x,y,t) \tag{5-3}$$

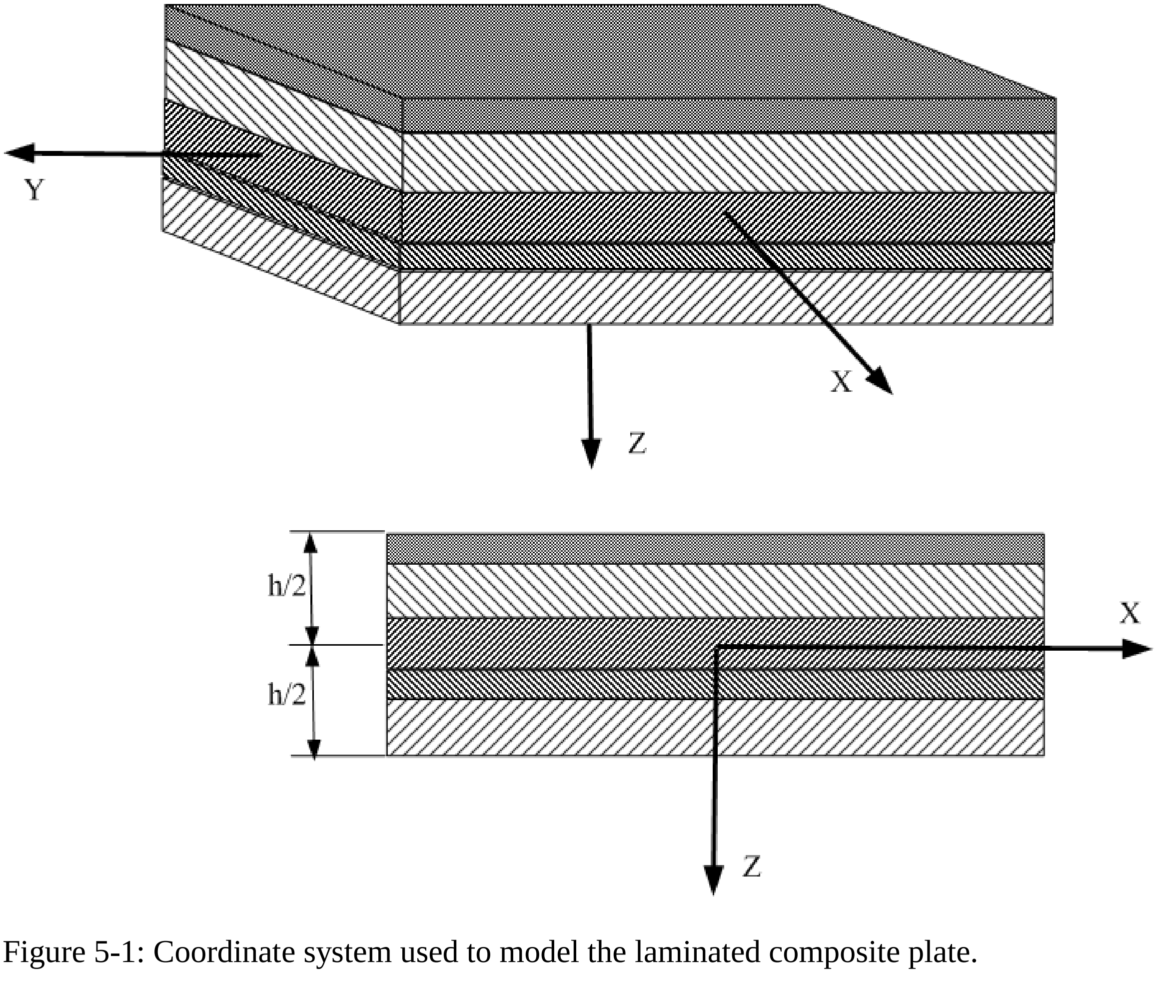

Figure 5-1: Coordinate system used to model the laminated composite plate.

where $u, v,$ and w are the displacements in $x, y,$ and z directions, and $u_0, v_0,$ and w_0 are the displacements in mid-plane. Assuming infinitesimal strain and infinitesimal rotation of the normal to the mid-surface, the strain field corresponding to the above displacement field can be deduced as

$$\begin{Bmatrix} S_{xx} \\ S_{yy} \\ S_{xy} \end{Bmatrix} = \begin{Bmatrix} S_{xx}^{(0)} \\ S_{yy}^{(0)} \\ S_{xy}^{(0)} \end{Bmatrix} + z\begin{Bmatrix} S_{xx}^{(1)} \\ S_{yy}^{(1)} \\ S_{xy}^{(1)} \end{Bmatrix} = \begin{Bmatrix} \dfrac{\partial u_0}{\partial x} \\ \dfrac{\partial v_0}{\partial y} \\ \dfrac{\partial u_0}{\partial y} + \dfrac{\partial v_0}{\partial x} \end{Bmatrix} - z\begin{Bmatrix} \dfrac{\partial^2 w_0}{\partial x^2} \\ \dfrac{\partial^2 w_0}{\partial y^2} \\ 2\dfrac{\partial^2 w_0}{\partial x \partial y} \end{Bmatrix}, \text{ or} \qquad (5\text{-}4)$$

$$\{S\} = \{S^0\} - z\{S^1\}$$

where $\{S^0\}$ and $\{S^1\}$ are the membrane and the bending strains, respectively. The transverse strains S_{xz}, S_{yz}, and S_{zz} are all equal to zero.

Including the piezoelectric effect and following the notations used in IEEE standard on piezoelectricity [77], the constitutive equations for piezoelectric materials can be written in the following form,

$$\{T\} = [c^E]\{S\} - [e]\{E\}, \qquad (5\text{-}5)$$

$$\{D\} = [e]\{S\} + [\varepsilon^S]\{E\}, \qquad (5\text{-}6)$$

where $\{T\}$, $\{S\}$, $\{D\}$, $\{E\}$ are the stress tensor, strain tensor, electric displacement and electric field respectively and $[c^E]$, $[e]$, and $[\varepsilon^s]$ are stiffness, piezoelectric, and dielectric permittivity tensors respectively. Under plane stress condition as encountered in a thin layer or plate, the constitutive equations can be written in the following form for an orthotropic material with respect to the axes of material symmetry as

$$\begin{Bmatrix} T_1 \\ T_2 \\ T_6 \end{Bmatrix} = \begin{bmatrix} c_{11} & c_{12} & 0 \\ c_{12} & c_{22} & 0 \\ 0 & 0 & c_{66} \end{bmatrix} \begin{Bmatrix} S_1 \\ S_2 \\ S_6 \end{Bmatrix} - \begin{bmatrix} 0 & 0 & e_{31} \\ 0 & 0 & e_{32} \\ 0 & 0 & 0 \end{bmatrix} \begin{Bmatrix} E_1 \\ E_2 \\ E_3 \end{Bmatrix} \tag{5-7}$$

$$\begin{Bmatrix} D_1 \\ D_2 \\ D_3 \end{Bmatrix} = \begin{bmatrix} 0 & 0 & 0 \\ 0 & 0 & 0 \\ e_{31} & e_{32} & 0 \end{bmatrix} \begin{Bmatrix} S_1 \\ S_2 \\ S_6 \end{Bmatrix} + \begin{bmatrix} \varepsilon_{11} & 0 & 0 \\ 0 & \varepsilon_{22} & 0 \\ 0 & 0 & \varepsilon_{33} \end{bmatrix} \begin{Bmatrix} E_1 \\ E_2 \\ E_3 \end{Bmatrix} \tag{5-8}$$

where

$$c_{11} = \frac{E_1}{1-\nu_{12}\nu_{21}}, \qquad c_{22} = \frac{E_2}{1-\nu_{12}\nu_{21}}$$

$$c_{12} = \frac{\nu_{12}E_2}{1-\nu_{12}\nu_{21}}, \qquad c_{66} = G_{12}$$

with E_i, G_{ij}, and ν_{ij} being the Young's modulus, shear modulus, and Poisson's ratio respectively. With respect to the global coordinate system, the constitutive equations can be expressed as the following through standard tensor transformation,

$$\begin{Bmatrix} T_{xx} \\ T_{yy} \\ T_{xy} \end{Bmatrix} = \begin{bmatrix} \bar{c}_{11} & \bar{c}_{12} & \bar{c}_{16} \\ \bar{c}_{12} & \bar{c}_{22} & \bar{c}_{26} \\ \bar{c}_{16} & \bar{c}_{26} & \bar{c}_{66} \end{bmatrix} \begin{Bmatrix} S_{xx} \\ S_{yy} \\ S_{xy} \end{Bmatrix} - \begin{bmatrix} 0 & 0 & \bar{e}_{31} \\ 0 & 0 & \bar{e}_{32} \\ 0 & 0 & \bar{e}_{36} \end{bmatrix} \begin{Bmatrix} E_x \\ E_y \\ E_z \end{Bmatrix}, \tag{5-9}$$

$$\begin{Bmatrix} D_x \\ D_y \\ D_z \end{Bmatrix} = \begin{bmatrix} 0 & 0 & 0 \\ 0 & 0 & 0 \\ \bar{e}_{31} & \bar{e}_{32} & \bar{e}_{36} \end{bmatrix} \begin{Bmatrix} S_{xx} \\ S_{yy} \\ S_{xy} \end{Bmatrix} + \begin{bmatrix} \varepsilon_{xx} & \varepsilon_{xy} & 0 \\ \varepsilon_{xy} & \varepsilon_{yy} & 0 \\ 0 & 0 & \varepsilon_{zz} \end{bmatrix} \begin{Bmatrix} E_x \\ E_y \\ E_z \end{Bmatrix}. \tag{5-10}$$

The finite element formulation is based on the rectangular conforming plate element. Following the notations used by Lam *et. al*. [81], let $\{u\}$ and $\{\bar{u}\}$ be defined, respectively, as

$$\{u\} = \{u \quad v \quad w\}^T \quad , \tag{5-11}$$

and $$\{\bar{u}\} = \{u_0 \quad v_0 \quad w_0 \quad \partial w_0/\partial x \quad \partial w_0/\partial y \quad \partial^2 w_0/\partial x \partial y\}^T . \tag{5-12}$$

Here, $\{\bar{u}\}$ specifies the nodal degrees of freedom for a conforming element. For a nonconforming element as used by Lam *et. al*. [81], the degree of freedom, $\partial^2 w_0 / \partial x \partial y$, is excluded. A detailed discussion on conforming and nonconforming elements can be found in [79, 82]. $\{u\}$ is related to $\{\bar{u}\}$ by

$$\{u\} = \left[H\right]\{\bar{u}\} = \begin{bmatrix} 1 & 0 & 0 & -z & 0 & 0 \\ 0 & 1 & 0 & 0 & -z & 0 \\ 0 & 0 & 1 & 0 & 0 & 0 \end{bmatrix}\{\bar{u}\} \tag{5-13}$$

Through the shape functions, $\{\bar{u}\}$ for each element can be interpolated as follows.

$$u_0\left(x,y,t\right) \approx \sum_{i=1}^{4} u_{0i}^{e}\left(t\right)\psi_i^e\left(x,y\right) \tag{5-14}$$

$$v_0\left(x,y,t\right) \approx \sum_{i=1}^{4} v_{0i}^{e}\left(t\right)\psi_i^e\left(x,y\right) \tag{5-15}$$

$$w_0\left(x,y,t\right) \approx \sum_{i=1}^{4} w_{oi}(t) g_{i1}(x,y) + \frac{\partial w_{oi}(t)}{\partial x} g_{i2}(x,y) + \frac{\partial w_{oi}(t)}{\partial y} g_{i3}(x,y) + \frac{\partial^2 w_{oi}(t)}{\partial x \partial y} g_{i4}(x,y) \tag{5-16}$$

where the subscript *i* represents the node number and ψ_i and g_{ij} are the shape functions. With respect to the natural coordinate system (ξ, η) as shown in Figure 5-2 where $-1 \le \xi \le 1$ and $-1 \le \eta \le 1$, the shape functions can be expressed as [79, 81]

$$\psi_i = \frac{1}{4}(1+\xi\xi_i)(1+\eta\eta_i) \tag{5-17}$$

$$\begin{aligned} g_{i1} &= \frac{1}{16}\left(\xi + \xi_i\right)^2\left(\xi\xi_i - 2\right)\left(\eta + \eta_i\right)^2\left(\eta\eta_i - 2\right) \\ g_{i2} &= \frac{1}{16}\xi_i\left(\xi + \xi_i\right)^2\left(1-\xi\xi_i\right)\left(\eta + \eta_i\right)^2\left(\eta\eta_i - 2\right) \\ g_{i3} &= \frac{1}{16}\eta_i\left(\xi + \xi_i\right)^2\left(\xi\xi_i - 2\right)\left(\eta + \eta_i\right)^2\left(1-\eta\eta_i\right) \\ g_{i4} &= \frac{1}{16}\xi_i\eta_i\left(\xi + \xi_i\right)^2\left(1-\xi\xi_i\right)\left(\eta + \eta_i\right)^2\left(1-\eta\eta_i\right) \end{aligned} \tag{5-18}$$

For a 4-node rectangular element with the dimension of $2a \times 2b$ in x-y system, the transformation relations between x-y and ξ-η are $\xi = \frac{x - x_c}{a}$ and $\eta = \frac{y - y_c}{b}$.

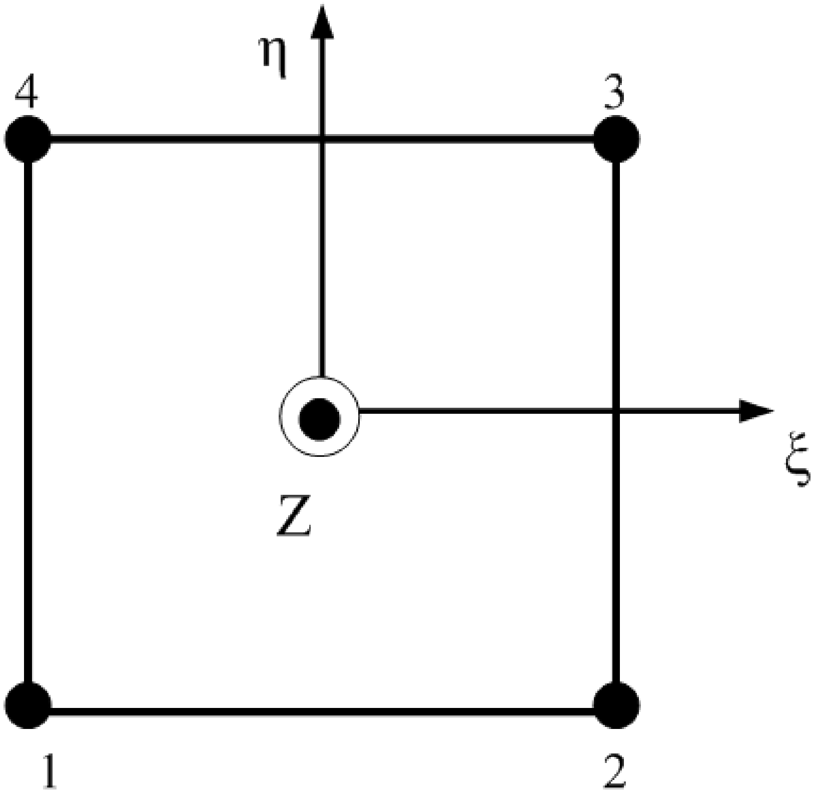

Figure 5-2: Node numbering and the natural coordinate system for the conforming rectangular element.

With the above interpolation incorporated, Eqn. (5-13) can be rewritten as

$$\{u\} = [H][N]\{u^e\}, \tag{5-19}$$

where $[N] = [N_1 \quad N_2 \quad N_3 \quad N_4]$, with $[N_i]$ being

$$\left[N_i\right] = \begin{bmatrix} \psi_i & 0 & 0 & 0 & 0 & 0 \\ 0 & \psi_i & 0 & 0 & 0 & 0 \\ 0 & 0 & g_{i1} & g_{i2} & g_{i3} & g_{i4} \\ 0 & 0 & \partial g_{i1}/\partial x & \partial g_{i2}/\partial x & \partial g_{i3}/\partial x & \partial g_{i4}/\partial x \\ 0 & 0 & \partial g_{i1}/\partial y & \partial g_{i2}/\partial y & \partial g_{i3}/\partial y & \partial g_{i4}/\partial y \\ 0 & 0 & \partial^2 g_{i1}/\partial x\partial y & \partial^2 g_{i2}/\partial x\partial y & \partial^2 g_{i3}/\partial x\partial y & \partial^2 g_{i4}/\partial x\partial y \end{bmatrix},$$

and $\{u^e\} = \{u_1^e \; u_2^e \; u_3^e \; u_4^e\}^T$ with $\left\{u_i^e\right\} = \left\{u_{0i} \quad v_{0i} \quad w_{0i} \quad \partial w_{0i}/\partial x \quad \partial w_{0i}/\partial y \quad \partial^2 w_{0i}/\partial x\partial y\right\}^T$.

Furthermore, the strain tensor can also be written in terms of $\{u^e\}$ as

$$\left\{S\right\} = \left[B\right]\left\{u^e\right\} \tag{5-20}$$

where $\left\{B\right\} = \left[\left[B_1\right] \; \left[B_2\right] \; \left[B_3\right] \; \left[B_4\right]\right] = \left[A\right] - z\left[C\right]$, with $\left[B_i\right] = \left[A_i\right] - z\left[C_i\right]$ and

$$\left[A_i\right] = \begin{bmatrix} \partial\psi_i/\partial x & 0 & 0 & 0 & 0 & 0 \\ 0 & \partial\psi_i/\partial y & 0 & 0 & 0 & 0 \\ \partial\psi_i/\partial y & \partial\psi_i/\partial x & 0 & 0 & 0 & 0 \end{bmatrix}$$

$$\left[C_i\right] = \begin{bmatrix} 0 & 0 & \partial^2 g_{i1}/\partial x^2 & \partial^2 g_{i2}/\partial x^2 & \partial^2 g_{i3}/\partial x^2 & \partial^2 g_{i4}/\partial x^2 \\ 0 & 0 & \partial^2 g_{i1}/\partial y^2 & \partial^2 g_{i2}/\partial y^2 & \partial^2 g_{i3}/\partial y^2 & \partial^2 g_{i4}/\partial y^2 \\ 0 & 0 & \partial^2 g_{i1}/\partial x\partial y & \partial^2 g_{i2}/\partial x\partial y & \partial^2 g_{i3}/\partial x\partial y & \partial^2 g_{i4}/\partial x\partial y \end{bmatrix}.$$

After the approximation relations are established, the dynamic finite element matrix equations can be derived using Hamilton’s principle, i.e.

$$\delta\int_{t_1}^{t_2}\left(T_k + W - U\right)dt = 0 \tag{5-21}$$

where T_k is the kinetic energy, W is the external work, and U is the strain energy defined, respectively, as [81]

$$T_k = \frac{1}{2}\int_{\overline{V}}\left(\rho\{\dot{u}\}^t\{\dot{u}\}\right)d\overline{V} \tag{5-22}$$

$$W = \int_{\overline{V}} \{u\}^T \{f_b\} d\overline{V} + \int_{\overline{S}} \{u\}^T \{f_s\} d\overline{S} + \{u\}^T \{f_c\} \tag{5-23}$$

$$U = \frac{1}{2}\int_{\overline{V}} \{S\}^T \{T\} d\overline{V} \tag{5-24}$$

where $\dot{u}$ is the velocity, f_b, f_s, f_c are body force, distributed surface force, and concentrated force, respectively. Substituting $\{u\}$, $\{S\}$, and $\{T\}$ into Eqns. (5-22), (5-23), and (5-24), we then obtain the dynamic element matrix equation as

$$\left[M^e\right]\left\{\ddot{u}^e\right\} + \left[K^e\right]\left\{u^e\right\} = \left\{F^e\right\} \tag{5-25}$$

$$\left[M^e\right] = \sum_{k=1}^{N} \int_{-1}^{1}\int_{-1}^{1} \rho_k \left[N\right]^T \left[\int_{z_k}^{z_{k+1}} \left[H\right]^T \left[H\right] dz\right] \left[N\right] \left|J\right| d\xi d\eta \tag{5-26}$$

$$\left[K^e\right] = \int_{V_e} \left[B\right]^T \left[c\right]\left[B\right] dv = \left[K_1^e\right] - \left[K_2^e\right] - \left[K_2^e\right]^T + \left[K_3^e\right] \tag{5-27}$$

$$\left[K_1^e\right] = \sum_{k=1}^{N} \left(z_{k+1} - z_k\right) \int_{-1}^{1}\int_{-1}^{1} \left[A\right]^T \left[c\right]_k \left[A\right] \left|J\right| d\xi d\eta \tag{5-28}$$

$$\left[K_2^e\right] = \sum_{k=1}^{N} \frac{1}{2}\left(z_{k+1}^2 - z_k^2\right) \int_{-1}^{1}\int_{-1}^{1} \left[A\right]^T \left[c\right]_k \left[C\right] \left|J\right| d\xi d\eta \tag{5-29}$$

$$\left[K_3^e\right] = \sum_{k=1}^{N} \frac{1}{3}\left(z_{k+1}^3 - z_k^3\right) \int_{-1}^{1}\int_{-1}^{1} \left[C\right]^T \left[c\right]_k \left[C\right] \left|J\right| d\xi d\eta \tag{5-30}$$

$$\left\{F^e\right\} = \int_{V_e} \left[N\right]^T \left[H\right]^T \left\{f_b\right\} dv + \int_{S_1} \left[N\right]^T \left[H\right]^T \left\{f_s\right\} dv + \left[N\right]^T \left[H\right]^T \left\{f_c\right\} \tag{5-31}$$

where *N* is the number of layers with each layer extending from z_k to z_{k+1}, and *J* is the Jacobean matrix. Notice that the electric force has not been incorporated in the matrix equation for the current work. The assembled global matrix equation is in the same form as Eqn. (5-25) but without the superscript "*e*".

5.3 Validation of FE Model

To validate the developed FE code, both static and eigenvalue problems were solved and the results were compared with published data. Static problems were solved by setting the inertia term equal to zero, i.e.

$$\left[K^e\right]\left\{u^e\right\}=\left\{F^e\right\}. \tag{5-32}$$

The eigenvalues (ω), which correspond to the natural frequencies of the system, were determined by solving the homogeneous equation in the form of

$$\left([K]-\omega^2[M]\right)\left\{u\right\}=0. \tag{5-33}$$

The boundary conditions considered in the FE model were simply supported and clamped conditions. The former were specified by $u_n=0$, $w_0=0$, and $M_n=0$ where u_n was the in-plane displacement normal to the side surface and M_n was the normal bending moment applied to the side of the membrane; and the latter were specified by $u_0=\mathrm{v}_0=w_0=\dfrac{\partial w_0}{\partial n}=0$ where n is the distance measured along the normal to the side surface.

For static problems, maximum deflection of square laminated plate with uniformly distributed transverse load were calculated for (0/90) cross-ply and $(-45/45)_4$ angle-ply composites under simply supported boundary condition. (0/90) cross-ply means the composite consists of two layers aligned in the 0° and 90° directions, respectively, and $(-45/45)_4$ means that a pair of –45 and 45 angle plies are laminated four times, i.e. eight layers in total. Due to the symmetry, only one quarter of the plate was analyzed to save computing cost. The obtained results along with some published data [79] are tabulated in Table 5-1.

	Elements	2 by 2	4 by 4	8 by 8	16 by 16	32 by 32	Anal. [79]
Cross-Ply (0/90)	**Current result**	1.6466	1.6838	1.6926	1.6948	1.6952	1.6955
	Ref. [70]	1.7004	1.6909	1.6935	NA	NA	1.6955
Angle-Ply	**Current result**	0.3857	0.3857	0.3858	0.3858	0.3858	0.3858
(-45/45)$_4$	**Ref.** [70]	0.3948	0.3870	0.3859	NA	NA	0.3858

Table 5-1: Nondimensionalized maximum deflections ($\bar{w}$) of simply supported laminated plates. $\bar{w} = w_0\left(\frac{E_2h^3}{a^4q_0}\right)*100$, where a is the length of the square plate, h is the thickness of a square plate, and q_0 is the distributed load. $a/h = 10$, $E_1/E_2 = 25$, $G_{12} = E_2/2$, $v_{12} = 0.25$.

For the eigenvalue problems, the fundamental frequencies for (-45/45)$_2$ angle-ply and (0/90)$_4$ cross-ply under simply supported boundary condition, and (0/0/0), (15/-15/15), (30/-30/30), and (45/-45/45) angle-plies under clamped boundary condition were calculated and the results are tabulated in Table 5-2 and Table 5-3, respectively, in normalized form. The excellent agreement between the calculated results and published data provides a credible validation for the developed code.

(-45/45)$_2$	**Ref.** [83]	**Ref.** [84]	**Ref.** [79]	**Current results**		**Anal.** [79]
				4 by 4	20 by 20	
Frequency	23.530	23.530	23.294	23.319	23.305	23.304
(0/90)$_4$	**Current results**					**Anal.** [79]
	4 by 4	8 by 8	16 by 16	25 by 25	35 by 35	
Frequency	18.3622	18.3582	18.3573	18.3571	18.3570	18.3520

Table 5-2: Fundamental frequencies ($\varpi = \omega\left(\frac{a^2}{h}\right)\sqrt{\frac{\rho}{E_2}}$) of simply supported (-45/45)$_2$ angle-ply and (0/90)$_4$ cross-ply (*$a/h = 10$, $E_1/E_2 = 40$, $G_{12} = 0.6E_2$, $v_{12} = 0.25$*).

	Element	**Current result (Fr.)**	**Ref.** [85]
(0/0/0)	20 by 20	8.463	8.498
(15/-15/15)	20 by 20	8.417	8.444
(30/-30/30)	20 by 20	8.317	8.418
(45/-45/45)	20 by 20	8.269	8.334

Table 5-3: Fundamental frequencies ($\varpi = \omega \left(\frac{a^2}{h} \right) \sqrt{\frac{\rho}{E_1}}$) of angle-plies under clamped boundary condition ($a/h = 16.67$, $E_1 = 60.7GPa$, $E_2 = 24.8GPa$, $G_{12}=12.0GPa$, $v_{12} = 0.23$).

5.4 Comparison of FEA and Experimental Results

As another validation of the numerical results, the fundamental frequencies of the fabricated membrane structures as described in Chapter 4 were measured and the results were compared with the corresponding calculations from finite element analysis. The fundamental frequencies were characterized with an impedance analyzer and impedance probe kit as explained before. The experimental results are shown in Figure 5-3 combined with FEA calculations. As expected, the data showed that the frequencies decreased with the increase of the membrane sizes. Furthermore, for the small membranes, the frequencies showed little length dependence. This was due to their large length to the width aspect ratios. For the large aspect ratios, the behavior of a structure is close to what would be expected for a one-dimensional structure for which the length can be considered as infinitely long with respect to the width. Under this condition, the length dependence is expected to diminish. As the *L*/*W* aspect ratios get smaller, the length dependence becomes stronger as shown by the data for the rectangular membranes (RM) for large membranes.

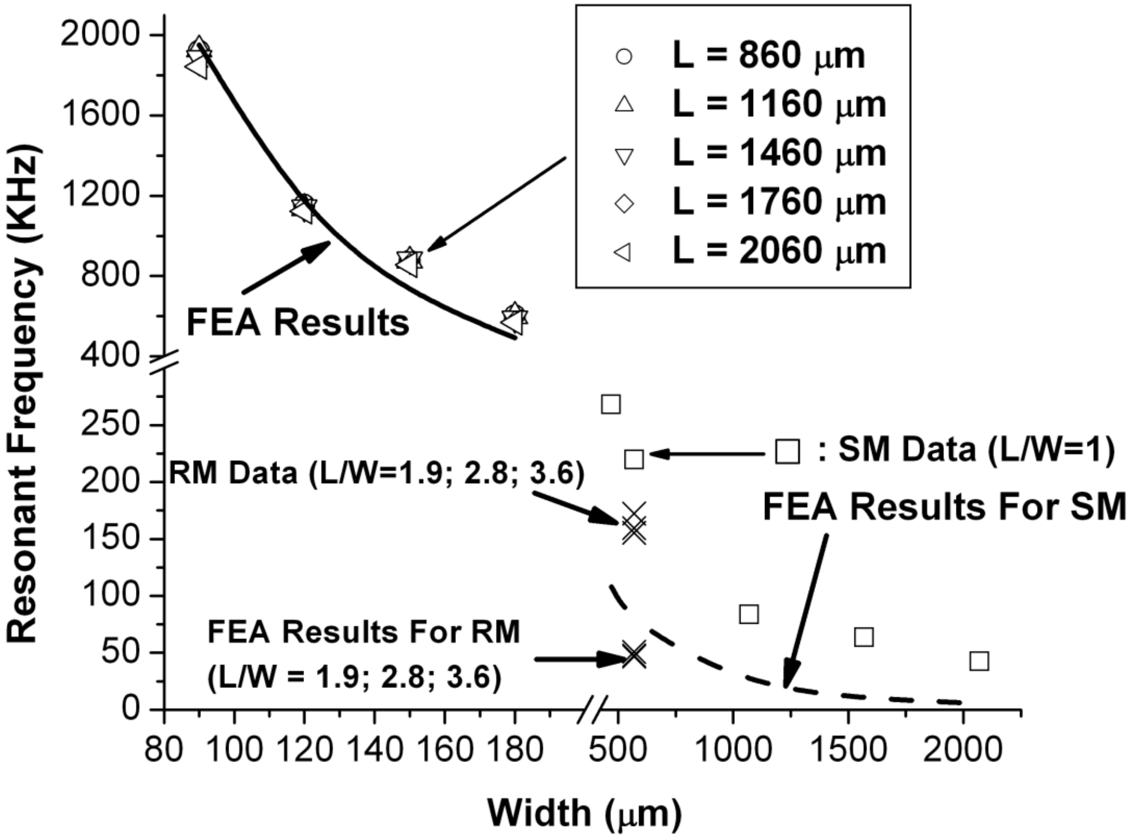

Figure 5-3: Experimental data and FEA results for the thin film membrane structures.

For numerical simulation, the appropriate number of elements used was determined by convergence study. As an example, the numbers of elements used for the large membranes are listed in Table 5-4. In these models, the materials were assumed to be isotropic and the relevant properties are listed in Table 5-5. Clamped boundary condition was used in all the following calculations.

SM	**Size (mm)**	**Elements**
SM1	0.47 by 0.47	20 by 20
SM2	0.57 by 0.57	20 by 20
SM3	1.07 by 1.07	20 by 20
SM4	1.57 by 1.57	20 by 20
SM5	2.07 by 2.07	20 by 20
RM		
RM1	0.57 by 1.07	15 by 30
RM2	0.57 by 1.57	10 by 30
RM3	0.57 by 2.07	10 by 40

Table 5-4: Sizes and numbers of elements used for the FE analysis of large membranes.

	E (GPa)	**ν**	**G (GPa)**	**ρ (Kg/m^3)**	**Thickness (μm)**
Silicon	125	0.278	48.90	2330	2.0
SiO_2	75	0.17	32.05	2200	0.2
Pt	170	0.39	61.15	21440	0.175 (small)/ 0.2 (large)
PZT	63	0.31	24.05	7500	1.0 (small)/ 0.8 (large)
Gold	80	0.44	27.78	19280	0.2

Table 5-5: Material properties used in the FE calculations.

As indicated by Figure 5-3, the calculations were matched fairly well with the data for the small membranes. However, they underestimated the frequencies for large membranes, both SM and RM. The calculations also showed little length dependence for small membranes and some dependence for large ones. These were also consistent with the experimental data. A plot of the calculated mode shape for a square membrane is shown in Figure 5-4.

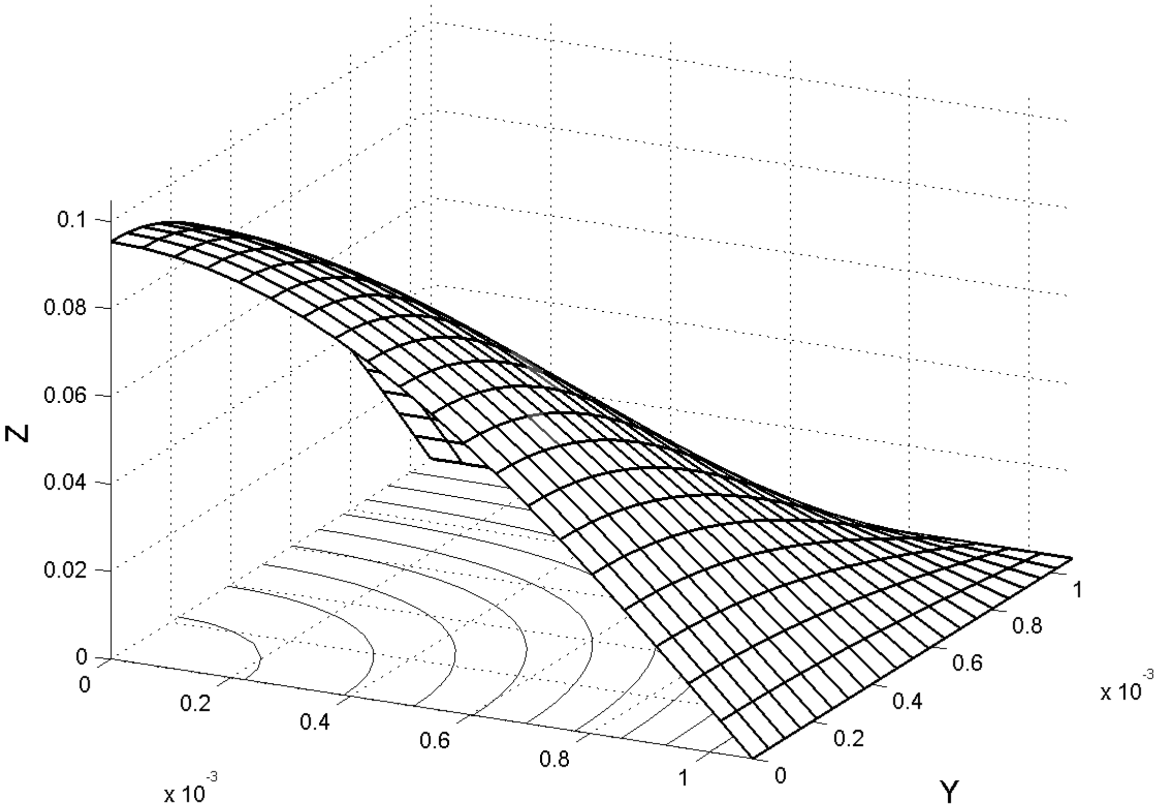

Figure 5-4: Fundamental mode shape for a square membrane.

Besides the calculations described above, a parametric study was also carried out to investigate the effect of the layer thickness on the fundamental frequencies of the membrane structures and the results are shown in Figure 5-5. In these calculations, the thickness of Si and PZT were independently varied from 1 to 5μm while keeping the rest of dimensions and material properties fixed as shown in Table 5-5. The membrane size used in these calculations was 180μm by 860μm. The thickness of Si and PZT were more than 85% of the overall thickness. Thus, they played more dominant role than the other layers in the dynamic response of the thin film structure. Figure 5-5 shows that the fundamental frequencies increase with the thickness of

Si and PZT layers. This is expected as the increase of the thickness leads to increase of the stiffness of the structure which in turn leads to increase of the fundamental frequency.

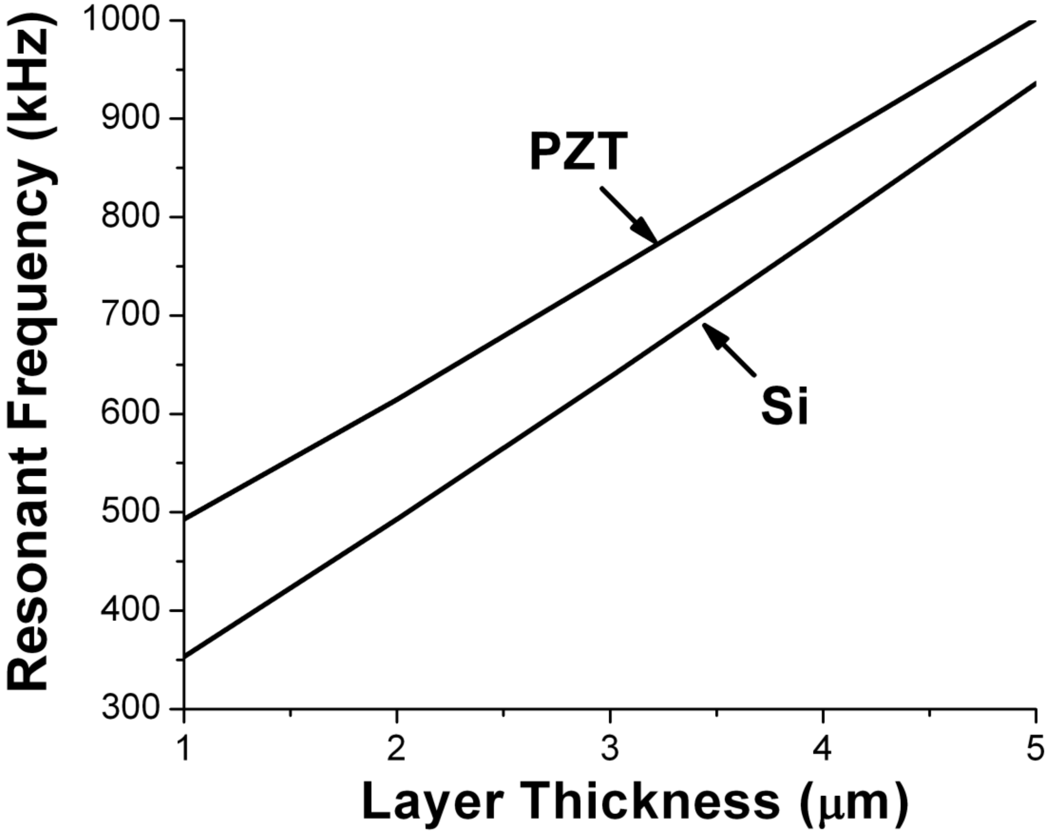

Figure 5-5: Simulated effects of thickness of Si and PZT layers on the fundamental frequencies of the membrane structure. The membrane size is 180μm by 860μm. The material properties and the rest of dimensions are kept the same as those shown in Table 5-5.

5.5 Discussion

In this chapter, a finite element model based on a combination of equivalent single-plate theory, classical plate theory, and rectangular conforming element was used to study the mechanical response of thin film membrane structures. After it was successfully validated by the published data on the static and dynamic responses of plates and membranes, the model was then used to predict the fundamental frequencies of thin film membrane structures in the micro length scale. It was demonstrated that the model predicted the qualitative trend correctly. On the quantitative side, the calculations were matched fairly well with the experimental data for the small membranes with the width less than 200µm, but underestimated them for large ones with the width greater than 500µm.

One most probable reason for the aforementioned quantitative discrepancies is the residual stress. The residual stress is likely to be generated during the micro fabrication process due to the different thermal expansion coefficients for different layer materials. As mentioned earlier, platinum layer was annealed at 650^{o}C for 10 minutes after DC sputtering to avoid delamination between SiO_2 and platinum layers. After annealing, the wafer was cooled at a rate of 100˚C/min to room temperature [86]. This thermal cycling process would undoubtedly generate some residual stress in the structure. One of the significant consequences from the residual stress is the shape distortion. In the aforementioned calculations, the membranes were all assumed to be flat. A distorted membrane, e.g. a dome-shaped membrane, would certainly have different dynamic responses than flat membranes. Between small and large membranes, the shape of the latter would be expected to be affected more by residual stress due to its larger flexibility.

Another possible reason for the discrepancy is the effect of DC bias voltage. We observed slight increase of fundamental frequency when the DC bias voltage increases while measuring the fundamental frequency. Similar observations were also reported by Baborowski *et al*. [87] and Muralt *et al*. [65]. Furthermore, the parasitic capacitance by the square pad and connection lead may also play some role on the dynamic behavior of the structure.

Other possible reasons include the difficulties in obtaining the precise measurement of the dimensions and material properties of the thin films and identification of the precise boundary conditions for the analysis. The boundary condition used in the current calculations was clamped condition which implied infinite rotational stiffness for the support. For the pMUTs fabricated in this study, the size of the membrane portion was very small compared to that of the support which constituted the rest of the structure. Thus, clamped boundary condition seemed to be reasonable and was not expected to be a contributor to the discrepancies observed here. However, for a more general membrane structure with a shape similar to that illustrated in Figure 2-7, the actual boundary conditions for the membrane could be quite complicated. The size, geometry, and material properties for the support could all affect the stiffness of the membrane.

Finally, it should be reiterated that the work in this chapter only considered the mechanical responses of thin film membrane structures for pMUTs and is a working progress towards more general electromechanical analysis. The electrical response and its coupling with mechanical responses of the structure will be addressed in the future work.

5.6 Conclusions

In this chapter, a finite element code based on a combination of equivalent single-plate theory and classical laminated plate theory was developed to predict the dynamic response of thin film membrane structures in micro length scale. The FE model was first validated by comparing the results with published data. As a benchmark for the code development, thin film structures were also fabricated using MEMS technology and their fundamental frequencies were characterized. It was demonstrated that the model predictions were matched fairly well with the experimental data for the small membranes whose widths were less than 200µm, but underestimated them for large ones whose widths were greater than 500µm. The model also demonstrated that the fundamental frequencies increased with the thickness of the layers and a model shape was presented for a square membrane.

The areas that need to be investigated further in order to improve the predicative capability of the calculations include effects of residual stress, DC bias voltage, parasitic capacitance, interaction of membrane vibration with the supports of the structure, and accurate measurement of the dimensions and material properties of the thin films.

CAHPTER 6

6 One Dimensional Analytical Solution for pMUTs

6.1 Introduction

A typical design methodology consists of both an analytical study and numerical simulation and they are expected to contribute to save fabrication time and cost. The analytical study provides rapid and rational insights, while the numerical simulation renders a detailed analysis of the response of the structures. To find the optimized design parameters of pMUTs, the existence of analytical or numerical model is advantageous and sometimes necessary.

Examples of analytical models for actuators/sensors or transducers can be found in the following references. Smits *et al.* [23], DeVoe *et al.* [24], and Weinberg [25] presented the analytical modeling of piezoelectric cantilever actuators/sensors. Two-dimensional plate equations for circular piezoelectrically actuated ultrasound transducers are presented by Percin *et al.* [26, 27]. One-dimensional model was developed by Cho *et al.* to predict the performance of membrane-type piezoelectric device [28]. For the numerical simulation, a recent effort can be found in the work by Choi *et al.* [88]. Since the small size single element pMUT has a long rectangular membrane with large length/width aspect ratio, the one-dimensional model presented by Cho *et al.* was used in this study to understand the effect of design parameters on the performance of pMUT. However, two-dimensional model is necessary if the length/width aspect ratio is not large enough.

The single-element pMUT shown in Figure 4-6(a) has a long, slender shape, i.e. a large length/width aspect ratio, and represents the first generation of our pMUT design. One objective of this chapter is to implement the one-dimensional model as reported in [28] as an analytical design model to gain physical insights into the observed performance. As will be shown later, the use of one-dimensional model is justified by the large length/width aspect ratio possessed by the current design of pMUTs. This work is part of the overall research effort for optimizing the design parameters and development of design methodology for pMUTs. Some previous experimental work related to this effort was reported in [76, 89].

6.2 1D Composite Beam Model and Its Correlation with the Equivalent Circuit

To gain insights into the physical significance of the equivalent circuit components, an electromechanical model was used to study the correlation between the circuit components and structural parameters for the pMUTs studied here. As mentioned earlier, the pMUT has a long, slender shape. The length to width aspect ratio ranges from 5:1 to 23:1 with more than half of them was having an aspect ratio greater than 10. Because of the large aspect ratios involved here, the pMUT was idealized as a one-dimensional structure, with its length assumed to be infinitely large compared to its width. Specifically, it was treated as a one-dimensional, two-layer composite beam as described in [28] and the 1D theory developed in [28] was used to study the correlation. One justification for the assumption of the one-dimensional model is that the resonance frequencies shown in Figure 4-13 had little length dependence.

A schematic diagram of the beam model and its geometric correlation with the pMUT is shown in Figure 6-1, where the layer with thickness h is made of an active piezoelectric material and the layer with thickness d is made of a passive elastic material. The electrode covers the area of $a \le x \le b$ and $0 \le y \le L$. The neutral plane is at $z = 0$ and its vertical deflection is designated by *w(x,t)*. The distance between the neutral plane and the bottom side of beam is z^*. As mentioned earlier, for the pMUTs fabricated in this study, $a \approx 30\mu m$.

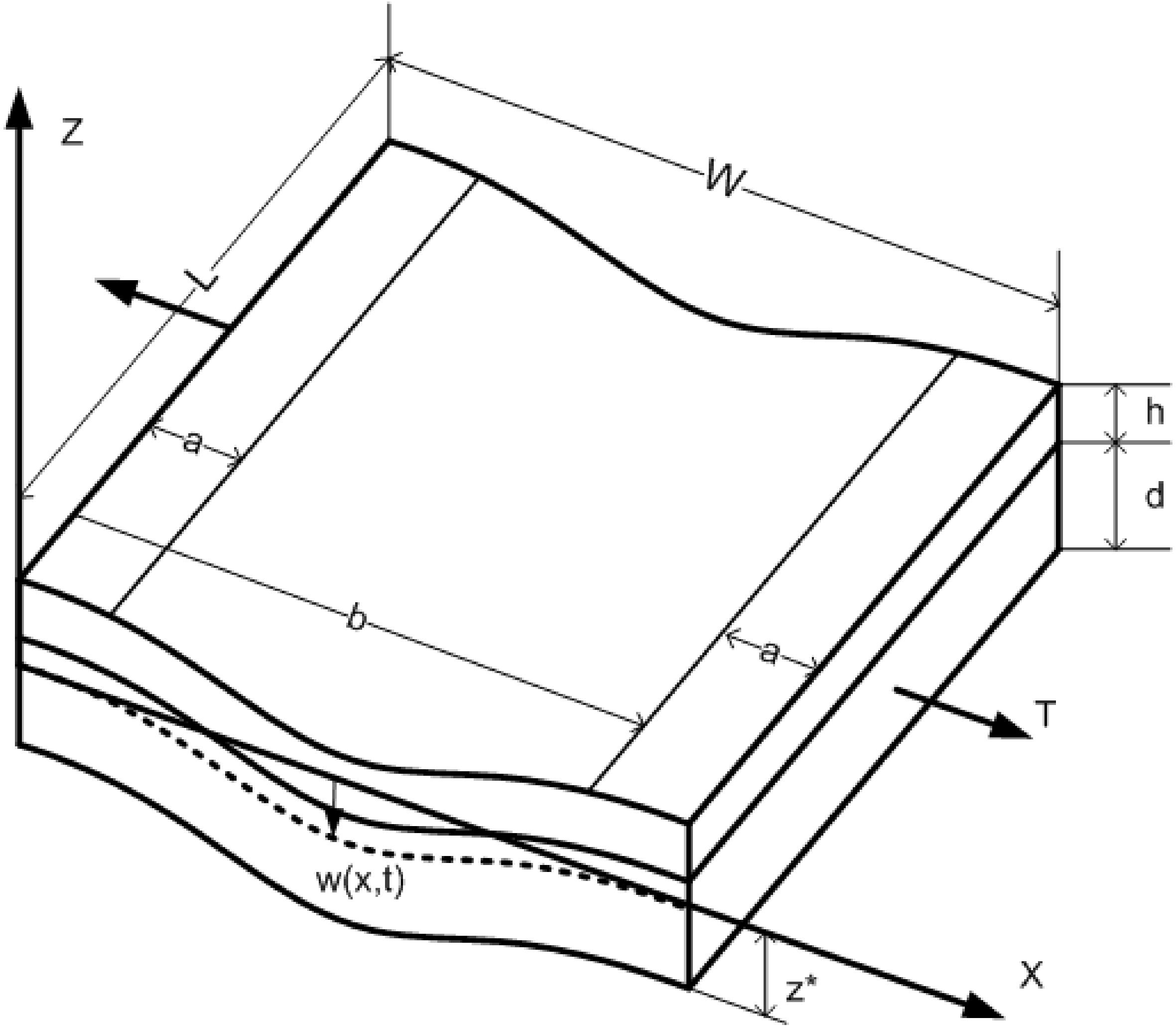

Figure 6-1: One-dimensional composite beam model.

The idea of modeling pMUTs with a 1D membrane model is very similar to the soap film or thin membrane analogy used in the study of the torsion of a bar with narrow rectangular cross section [90]. In this study, the out-of-plane displacement of the bar is analyzed by treating the cross section as a 1D membrane which has the same shape and dimension as those of the cross section of the bar. The vertical displacement of a 1D membrane is a function of the dimension along the width direction only, i.e. *x* in Figure 6-1. To illustrate this point, the fundamental mode shapes for the pMUTs with the largest (23:1) and smallest (5:1) aspect ratios were calculated with a finite element analysis software, ANSYS 10.0 and are shown in Figure 6-2(a) and (b), respectively. The figures show that although some end effect still exists for both cases, the displacement gradient along the *x* or width direction is significantly larger than that along the *y* or length direction, implying that 1D is a reasonable assumption. The 1D approximation of the mode shape is depicted in Figure 6-3, which shows that the end effect along the length direction is ignored, i.e. the length is considered to be infinitely long compared to width. Accordingly, the out of plane displacement is a function of *x* only, hence, one dimensional.

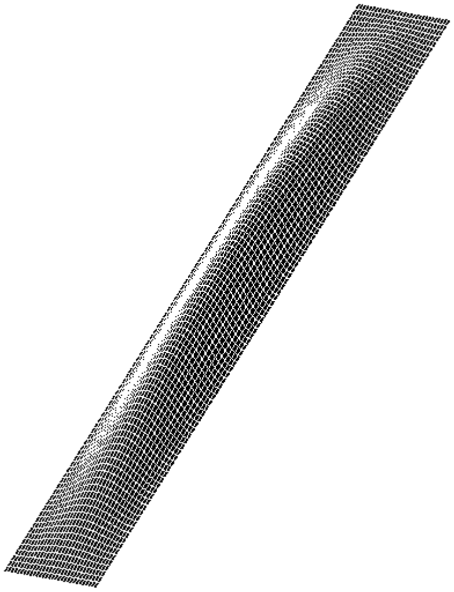

(a)

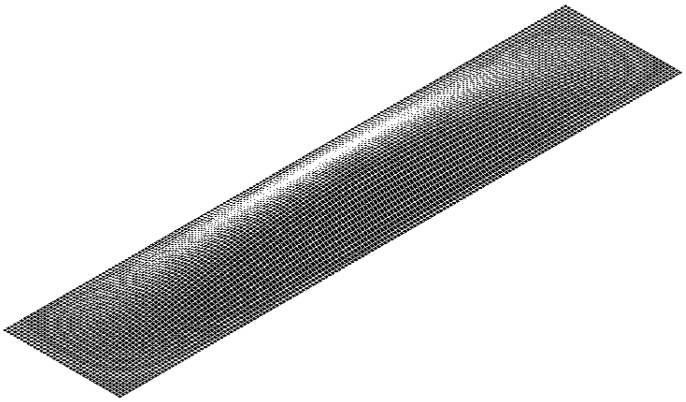

(b)

Figure 6-2: Fundamental mode shape calculated by ANSYS; (a) aspect ratio = 23:1 (b) aspect ratio = 5:1.

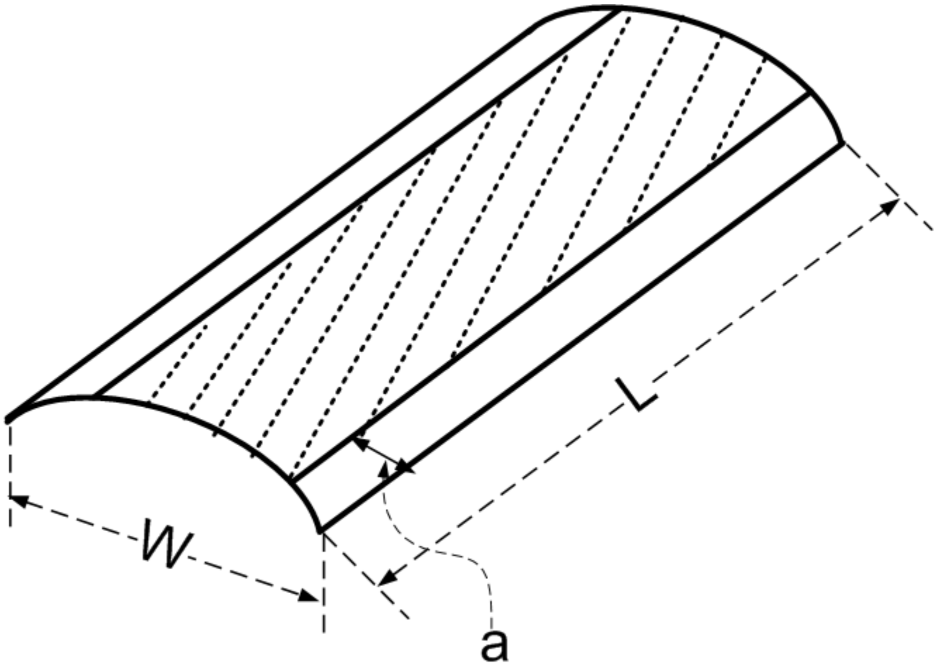

Figure 6-3: 1D approximation of the mode shape.

The relevant governing equations for the composite beam are listed in the following.

Equation of motion:

$$\bar{\rho}\frac{\partial^2 w}{\partial t^2}-\frac{\partial^2 M}{\partial x^2}=F \tag{6-1}$$

where $\bar{\rho}=\rho_d d+\rho_h h$ is the mass per unit area with ρ_d and ρ_h being the densities of the silicon and PZT layers respectively, M is the bending moment per unit length, and $F(t)$ is an applied vertical force per unit area. In [28], equation of motion also contains the contribution from an axial force that was assumed to result from the residual stress. The effect of residual stress will be discussed later.

Constitutive Equation:

$$\begin{aligned} S_1 &= s_{11}^E T_1 + s_{12}^E T_2 + d_{31} E_3 \\ S_2 &= s_{12}^E T_1 + s_{22}^E T_2 + d_{31} E_3 \\ D_3 &= d_{31} T_1 + d_{31} T_2 + \varepsilon_{33}^T E_3 \end{aligned} \tag{6-2}$$

where *S, T, E,* and *D* are strain, stress, electric field, and electric displacement, respectively; s_{ij}, d_{ij}, and ε_{ij} are mechanical compliance, piezoelectric constant, and dielectric permittivity, respectively; the superscripts '*E*' and '*T*' represent the states of constant electric field and constant stress respectively; and the indices *1, 2,* and *3* indicate *x, y,* and *z* directions, respectively. For non-piezoelectric material, the piezoelectric and dielectric constants are zero.

Strain-displacement relation:

$$S_1=-z\frac{\partial^2 w}{\partial x^2} \tag{6-3}$$

Maxwell Equation:

$$\frac{\partial D_3}{\partial z}=0 \tag{6-4}$$

Electric field –potential (V) relation:

$$E_3=-\frac{\partial V}{\partial z} \tag{6-5}$$

The detailed derivation of the electromechanical equations for the composite beam can be found in [28]. For the continuity of this section and convenience for subsequent discussion, some key results are described in the following.

By combining the aforementioned governing equations, the equation of motion can be written in terms of vertical displacement w as follows.

$$\bar{\rho}\frac{\partial^2 w}{\partial t^2}+K\frac{\partial^4 w}{\partial x^4}+\frac{d_{31}}{s_{11}^E}\left(d-z^*+\frac{h}{2}\right)\left[\delta'(x-a)-\delta'(x-b)\right]V=F \tag{6-6}$$

where $K=\left[\frac{1}{s_{11}^E}d\left(\frac{d^2}{3}-dz^*+z^{*2}\right)+\alpha h\left(d^2+z^{*2}-2dz^*+hd-hz^*+\frac{h^2}{3}\right)\right]$ represents the bending stiffness with $\alpha=\frac{1}{s_{11}^E\left(1-\frac{d_{31}^2}{s_{11}^E\varepsilon_{33}^T}\right)}$, and $\delta'(x)=\frac{d\delta}{dx}$ with $\delta(x)$ being the Dirac delta function. In arriving this equation, it was assumed that the forces caused by coupling with the derivatives of the membrane deflection could be neglected [28]. The last term on the left-hand side of Eqn. (6-6) represents the line moment at the edges of the electrode caused by the applied voltage V. Furthermore, by applying Gauss' law, the free charge on the whole electrode can also be written as

$$Q=\frac{L(b-a)\varepsilon_{33}^T}{h}\left(1-\frac{d_{31}^2}{s_{11}^E\varepsilon_{33}^T}\right)V-\frac{Ld_{31}}{s_{11}^E}\left(d-z^*+\frac{h}{2}\right)\int_a^b\frac{\partial^2 w}{\partial x^2}dx \tag{6-7}$$

Notice that Eqns. (6-1) to (6-5) were formulated on a per unit length basis, e.g. M in Eqn. (6-5) represents the bending moment per unit length. These equations would have led to free charge per unit length of electrode, i.e.

$$\frac{Q}{L}=\frac{(b-a)\varepsilon_{33}^{T}}{h}\left(1-\frac{d_{31}^{2}}{s_{11}^{E}\varepsilon_{33}^{T}}\right)V-\frac{d_{31}}{s_{11}^{E}}\left(d-z^{*}+\frac{h}{2}\right)\int_{a}^{b}\frac{\partial^{2}w}{\partial x^{2}}dx \tag{6-8}$$

However, in order to compare the model with the experimental data, the model has to be scaled up to the actual length of the structure. Accordingly, the right hand side of the free charge equation has to be multiplied by L to get the "total" free charge, Q. This is how "L" comes into the model even though all the governing equations are one dimensional. This point will be illustrated later again.

Using mode superposition and fundamental mode approximation, $w(x,t)$ can be approximated as

$$w(x,t)=\sum_{n}\Phi_{n}(x)g_{n}(t)\approx\Phi_{1}(x)g_{1}(t) \tag{6-9}$$

where Φ_n and g_n represent the mode shape and mode coordinate for the n^{th} normal mode, respectively. Substituting Eqn. (6-9) into Eqns. (6-6) and (6-7) yields a lumped two-port electromechanical model for the "whole" structure (not the structure on a unit-length basis) as followings.

$$\frac{m}{\Psi^{2}}(\Psi\ddot{g}_{1})+\frac{s}{\Psi^{2}}(\Psi g_{1})+V=\frac{\bar{F}}{\Psi} \tag{6-10}$$

and

$$Q=C_{0}V+\Psi g_{1} \tag{6-11}$$

where

$$m=\bar{\rho}L\Lambda_{0} \tag{6-12}$$

$$s = KL\Lambda_4 \tag{6-13}$$

$$\Psi = -\frac{Ld_{31}}{s_{11}^E}\left(d - z^* + \frac{h}{2}\right)\int_0^W \Phi_1'' dx \tag{6-14}$$

$$\bar{F} = \int_0^W L\Phi_1 F dx \tag{6-15}$$

$$C_0 = \frac{L(b-a)\varepsilon_{33}^T}{h}\left(1 - \frac{d_{31}^2}{s_{11}^E \varepsilon_{33}^T}\right) \tag{6-16}$$

with $\Lambda_0 = \int_0^W \Phi_1^2 dx$, and $\Lambda_4 = \int_0^W \Phi_1 \Phi_1'''' dx$. Φ_1'' and Φ_1'''' refer to the second and fourth order derivatives, respectively.

From Eqn. (6-10), L_1 and C_1 in the equivalent circuit can be established as

$$L_1 = \frac{m}{\Psi^2}, \tag{6-17}$$

and $C_1 = \frac{\Psi^2}{s}$ (6-18)

Notice that length L also appears in Eqns. (6-12) to (6-16) for exactly the same reason as described for Eqns. (6-7) and (6-8). Taking Eqn. (6-12) as an example, $\bar{\rho}\Lambda_0$ represents the mass per unit length and the total mass, m, is obtained by multiplying L to $\bar{\rho}\Lambda_0$. The appearance of L in these equations is essentially to obtain the structure properties that are extensive with respect to the length, namely, Q, m, s, Ψ, $\bar{F}$, and C_0 as described by Eqns.(6-7), (6-12) to (6-16), respectively; and is necessary for comparison of the model with the experimental data which were obtained from a structure with a non-unity length. In other words, the length dependence results purely from the scaling relation instead of multi-dimensionality of the physics involved.

It should be reminded again that the governing equations has no " y " dependence as illustrated in Figure 6-3.

It should also be mentioned that damping, which is related to the quality factor (Qu), was not considered in equation of motion. To demonstrate the correlation between damping and Qu, consider a linear damping case in which equation of motion is modified as

$$\bar{\rho}\frac{\partial^2 w}{\partial t^2}+b\frac{\partial w}{\partial t}-\frac{\partial^2 M}{\partial x^2}=F \tag{6-19}$$

where b is the damping coefficient. Accordingly, Eqn. (6-10) is changed to

$$\frac{m}{\Psi^2}(\Psi\ddot{g}_1)+\frac{d}{\Psi^2}(\Psi\dot{g}_1)+\frac{s}{\Psi^2}(\Psi g_1)+V=\frac{\bar{F}}{\Psi} \tag{6-20}$$

where $d=b\Lambda_0$. This equation indicates that R_1 in the equivalent circuit is equal to $b\Lambda_0/\Psi^2$, and its correlation with the quality factor can then be expressed as

$$Qu\ =\ \frac{\sqrt{L_1/C_1}}{R_1}=\frac{\sqrt{ms}}{R_1\Psi^2} \tag{6-21}$$

Since the damping behavior of pMUTs is far more complicated than the linear damping illustrated above, more in-depth studies will be needed. Accordingly, this effect was not considered in the current work.

Finally, some comments on the originality of the one dimensional model are in order. Compared to other composite plate models as used for the analysis of bulk composites such as [33] and those mentioned in the previous section, the current model has at least three important and unique features. One is that the current analysis results in a lumped electromechanical model which can be directly correlated with the equivalent circuit for the thin film membrane structures in contrast to the traditional bulk composites. Secondly, the current model deals with partial coverage of the electrode over the membrane. The latter has very important implication on the effect of electrode coverage area on the performance of pMUT, as will be discussed later. Thirdly, the effect of residual stress could also be included and examined by the model as will be demonstrated later.

6.3 First Order Analysis Based on the One-Dimensional Model

After the correlation between the equivalent circuit components and structural parameters is established, we can now use it to gain insights into the experimental results. A simple qualitative prediction could be made quite easily by a first order analysis of the equivalent circuit components, namely, C_0, C_1, and L_1. To this end, the orders of Ψ , Λ_0, and Λ_4, which are all related to $\Phi_1(x)$,i.e. the fundamental mode shape, have to be evaluated first.

For the pMUTs fabricated in this study, the size of the membrane was very small compared to that of the support. Thus, it is reasonable to assume that the boundary of the membrane was clamped, i.e. $\Phi(0)=\Phi(W)=\Phi'(0)=\Phi'(W)=0$. Under this boundary condition, $\Phi_1(x)$ can be approximated as [79]:

$$\Phi_1 = C\left(\frac{x}{W}\right)^2\left(1-\frac{x}{W}\right)^2 \tag{6-22}$$

Accordingly, the following relations can be derived.

$$\Lambda_0 = \int_0^W \Phi_1^2 dx \approx O(W) \tag{6-23}$$

$$\Lambda_4 = \int_0^W \Phi_1\Phi_1'''' dx \approx O\left(\frac{1}{W^3}\right) \tag{6-24}$$

Here, $O(W)$ implies that Λ_0 is in the order of W and so on. According to Eqn. (6-14), the order of Ψ is given as

$$\Psi \approx O\left(\frac{L}{W}\right) \tag{6-25}$$

Substituting Eqns. (6-23) to (6-25) into the relevant relations derived in the last section, we then obtain the following.

$$m = \bar{\rho} L \Lambda_0 \approx O(LW) \tag{6-26}$$

$$s = KL\Lambda_4 \approx O\left(\frac{L}{W^3}\right) \tag{6-27}$$

$$L_1 = m/\Psi^2 \approx O\left(\frac{W^3}{L}\right) \tag{6-28}$$

$$C_1 = \Psi^2/s \approx O(LW) \tag{6-29}$$

$$C_0 = \frac{L(b-a)\varepsilon_{33}^T}{h}\left(1 - \frac{d_{31}^2}{s_{11}^E \varepsilon_{33}^T}\right) \approx O(LW) \tag{6-30}$$

$$f_s = \frac{1}{2\pi\sqrt{L_1 C_1}} = \frac{1}{2\pi}\sqrt{\frac{s}{m}} \approx O\left(\frac{1}{W^2}\right) \tag{6-31}$$

$$k_{eff}^2 = \frac{C_1}{C_0 + C_1} = \frac{1}{C_0/C_1 + 1} \approx O(\text{constant}) \tag{6-32}$$

The linear dependence on length for m, s, Ψ, $\bar{F}$, and C_0 results from the fact that these properties are extensive with respect to length as explained earlier. The combinations of (m, Ψ^2) and (s, Ψ^2) result in $1/L$ dependence and linear length dependence for L_1 and C_1, respectively. However, the length dependence cancelled out for f_s and k_{eff}^2.

The above order analysis shows that L_1 increases with W but decreases with L; C_1 and C_0 increase with both W and L; f_s decreases with W but has no length dependence; and k_{eff}^2 is independent of either W or L. Except for the width dependence of k_{eff}^2, the predicted trends are consistent with the experimental observations as described earlier. The width dependence of k_{eff}^2 will be elaborated later.

6.4 Quantitative Prediction of pMUT Performance Based on the Beam Model

Since the beam is a two-layer composite which is different from the multi-layered pMUT, effective density and Young's modulus were used in the calculation. The material properties [28] and layer thicknesses used in the quantitative analysis are listed in Table 6-1. The bottom layer of the beam, which has a thickness *d*, consisted of silicon and SiO_2 layers, and the top layer, which has a thickness *h*, consisted of the platinum, PZT, and gold layers of the actual pMUT. The effective properties were defined as

$$\left(\rho_{eff} = \sum_{k=1}^{n} \rho_k t_k \Big/ \sum_{k=1}^{n} t_k\right), \tag{6-33}$$

and $\left(E_{eff} = \sum_{k=1}^{n} E_k t_k \Big/ \sum_{k=1}^{n} t_k\right)$. (6-34)

Material	Density ($\rho : Kg/m^3$)	Young's modulus (E: *GPa*)	$d_{31}: C/N$	k_{33}^T	Thickness (μm)
Si	2330	130	NA	NA	2
SiO_2	2200	75	NA	NA	0.2
Pt.	21440	170	NA	NA	0.175
PZT	7500	80	-88.1×10^{-12}	1100	1
Au.	19280	130	NA	NA	0.2

Table 6-1: Material properties and layer thicknesses used for the analytic solutions of pMUTs.

The constant C in Eqn. (6-22) bore no effect on the calculated results and was arbitrarily set to 1. The predicted results using the effective properties for the membranes with the largest (L=2060μm) and the smallest length (L=860μm) are included in Figure 6-4 through Figure 6-8 as dash-dot and dashed lines, respectively. The predictions for other lengths fall in between these two lines and are not shown in these figures.

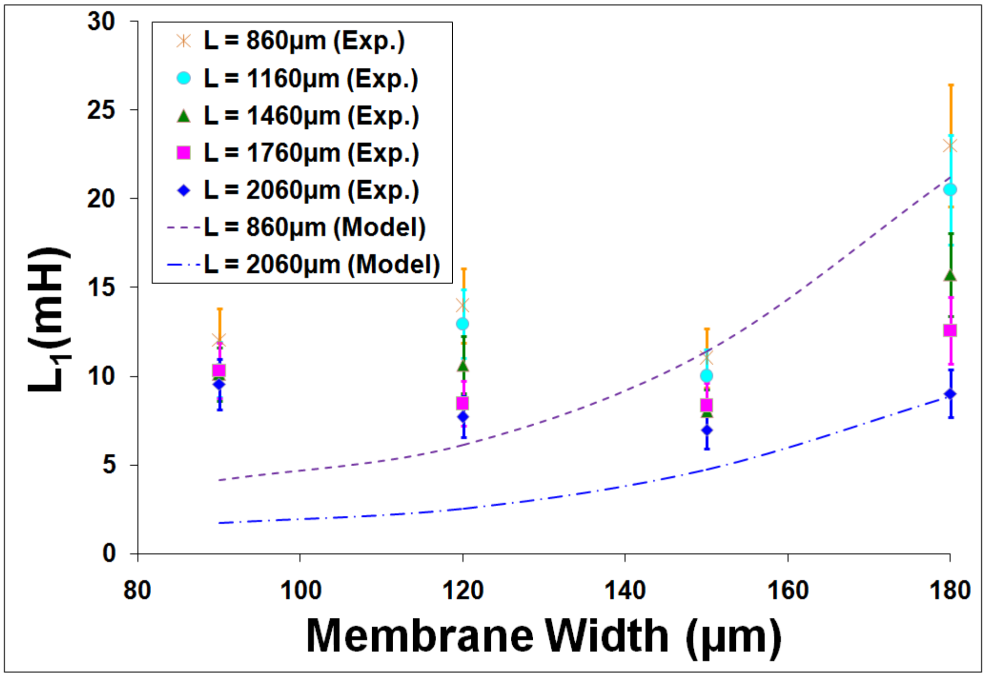

Figure 6-4: Motional inductance (L1) as a function of membrane dimensions. Dash-dot and dashed lines represent the calculated results based on the composite beam model for the membranes with the largest (L=2060μm) and the smallest length (L=860μm), respectively.

The calculated overall trend of L_1 was consistent with that exhibited by the experimental data. Quantitatively, the calculations were matched quite well with the data for the membranes with the width W greater than 150μm, but underestimated the data for widths less than 150μm. For C_1 as shown in Figure 6-5, the calculated trend was also consistent with the experimental observations although the calculations slightly overestimated the experimentally measured values. The calculations also showed a nonlinear dependence on the width in contrast with the linear dependence predicted by the first order analysis. This discrepancy will be elaborated later.

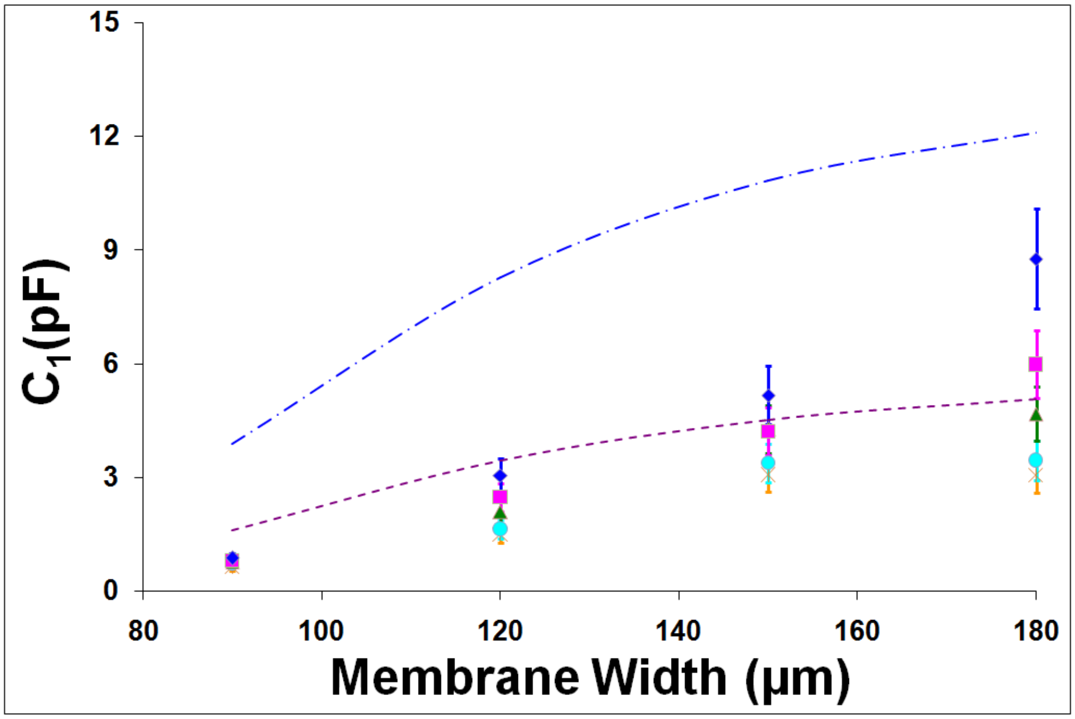

Figure 6-5: Motional capacitance (C_1) as a function of membrane dimensions. See Figure 6-4 for the legends.

For C_0 and f_s, the predictions were compared quite well with the data both qualitatively and quantitatively as shown in Figure 6-6 and Figure 6-7. For the effective coupling coefficient k_{eff}^2 shown in Figure 6-8, the calculations slightly overestimated the experimentally measured values for the membranes with W less than $150\mu m$, while reasonable agreement was observed for widths above this value. Furthermore, unlike the order analysis, the calculated results did exhibit a trend that was reasonably consistent with the experimental observation. As mentioned earlier, the experimentally measured k_{eff}^2 increased with the width up to approximately $W \approx 150\mu m$ and then started to decrease. This behavior was also observed in the predictions, although the predicted maximum k_{eff}^2 was observed to occur at a width of $W \approx 120\mu m$. The calculations also showed no length dependence for k_{eff}^2. As stated earlier, the experimental data for k_{eff}^2 did not show a consistent trend on length dependence after the error bars were taken into consideration as well.

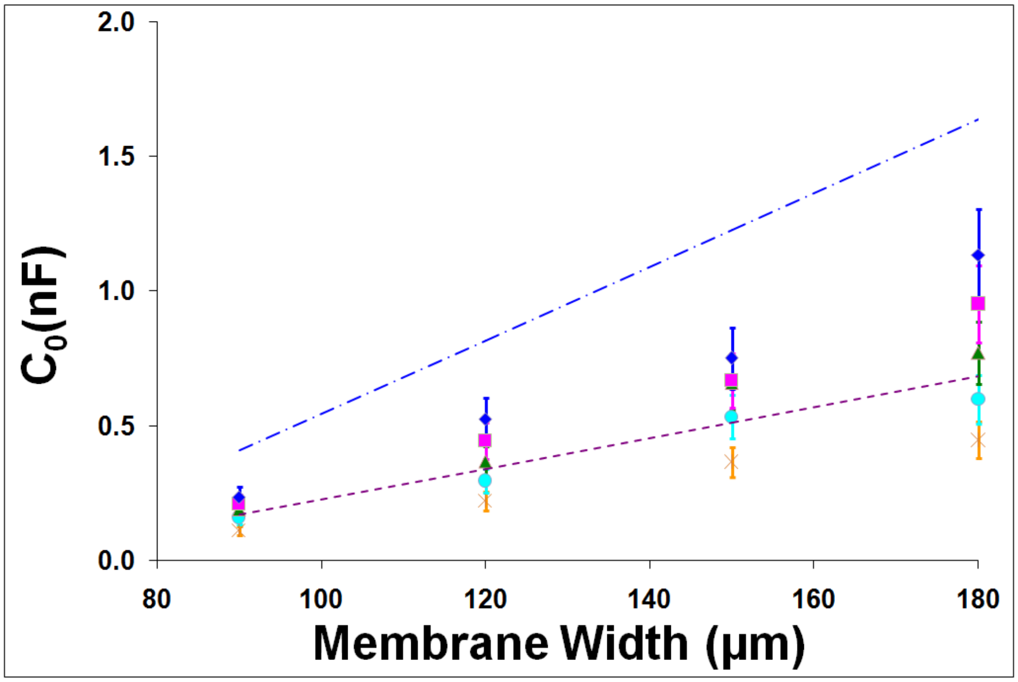

Figure 6-6: Parallel capacitance (C_0) as a function of membrane dimensions after considering parasitic capacitance. See Figure 6-4 for the legends.

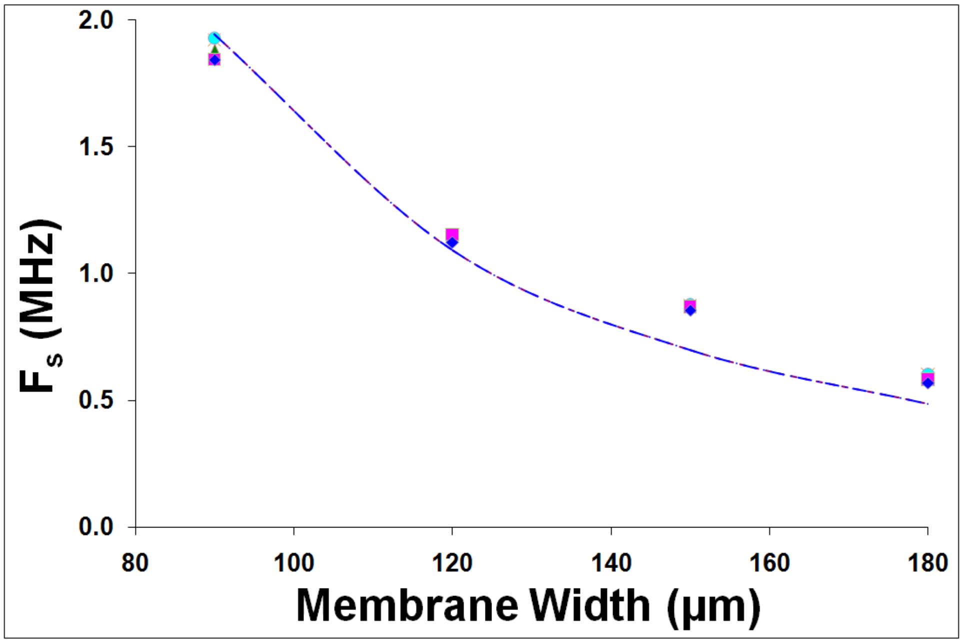

Figure 6-7: Resonance frequency (f_s) as a function of membrane dimensions. See Figure 6-4 for the legends.

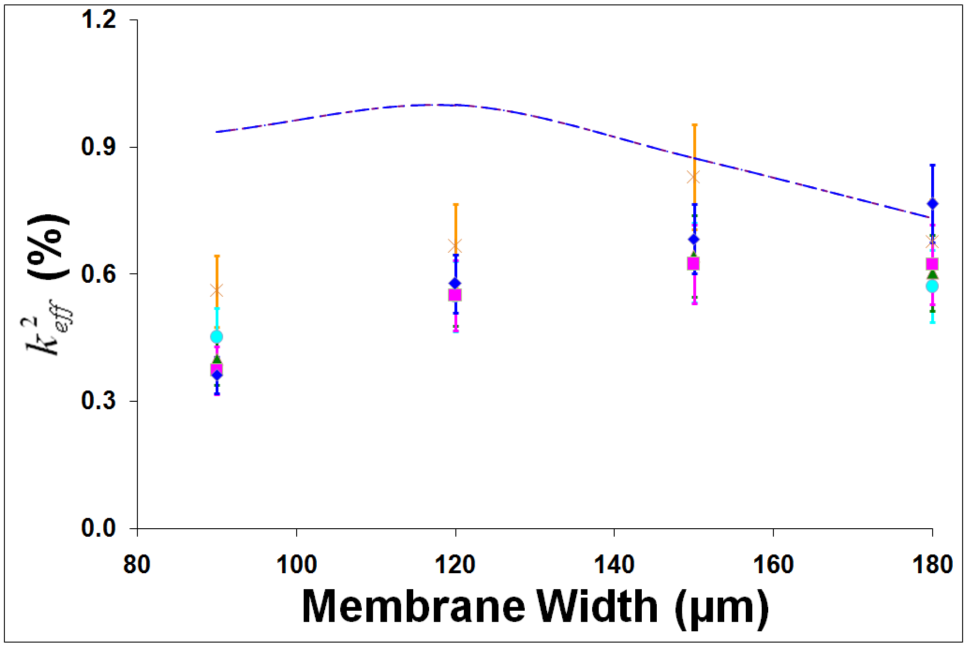

Figure 6-8: Effective coupling coefficient (k_{eff}^2) as a function of membrane dimensions after considering parasitic capacitance. See Figure 6-4 for the legends.

The slight differences between the predicted qualitative trends based on the first order and quantitative analyses can be explained as follows. Unlike the integrals for Λ_0 and Λ_4 whose integration range was from 0 to W, Ψ was obtained by integrating only over the electrode area, i.e. from *a* to *b*. The exact expression for Ψ based on Eqn. (6-14) is

$$\Psi = -\frac{Ld_{31}}{Ws_{11}^{E}}\left(d - z^{*} + \frac{h}{2}\right)\left[\frac{2(b-a)}{W} - \frac{6(b^2-a^2)}{W^2} + \frac{4(b^3-a^3)}{W^3}\right] \tag{6-35}$$

The terms inside the bracket are a function of the ratio of the electrode width to the membrane width, i.e. *(b-a)/W*. As mentioned earlier, *a* in Figure 6-1 was approximately $30\mu m$. Accordingly, the ratios ranged from 1/3 to 2/3 for *W*=90µm to *W*=180µm, respectively. The terms inside the bracket in Eqn. (6-35) represent the second order effect for all the physical quantities that involve Ψ, i.e. C_1, L_1, and k_{eff}^2. As described earlier, the first order analysis for C_1 showed a linear dependence of *W*. However, the quantitative analysis exhibited a nonlinear dependence as shown in Figure 6-5. This nonlinear dependence was attributed to the aforementioned second order effect. The same effect also contributed to part of the nonlinear dependence of L_1 on *W* although the major contribution to the nonlinear dependence appeared to be from the first order effect, i.e. L_1 was in the order of W^3.

The second order effect also showed up in k_{eff}^2 due to the dependence of k_{eff}^2 on C_1. As mentioned earlier, the first order analysis indicated that k_{eff}^2 was in the order of a constant. However, the quantitative analysis showed that k_{eff}^2 increased with the width up to certain point and then started to decrease. This trend, which was due to the second order electrode-to-membrane-ratio effect, was consistent with the experimental observation. The dependence of k_{eff}^2 on electrode-to-membrane width ratios was also observed and reported in [28]. As mentioned earlier, k_{eff}^2 was predicted to reach its maximum when $W \approx 120\mu m$. This corresponds to the case where *(b-a)/W* is 0.5, i.e. the electrode width is half of the membrane width. Recall that the edge of the electrode is where the line moment is applied according to Eqn. (6-6). This implies that k_{eff}^2 is highest when the line moment is applied at $a \approx \mathrm{W}/4$. Similar conclusion was also drawn in the works reported in [28, 91, 92].

Finally, some comments on the length dependence are in order. As explained earlier, the beam model used in this study is a one-dimensional model, i.e. all the governing equations are a function of width (*W*) only. The length dependence as shown in Eqn. (6-28) to (6-30) for L_1, C_1, and C_0, respectively, resulted purely from the fact that these physical quantities were extensive with respect to length, i.e. a scaling relation. Thus, one way to evaluate the validity of the one-dimensional model assumption is to check whether L_1, C_1, and C_0 indeed followed the trends described by Eqns. (6-28) to (6-30) with respect to the length dependence. To this end, these quantities were re-plotted in Figure 6-9 - Figure 6-11, as a function of length for a given width, for L_1, C_1, and C_0, respectively. For C_0 and C_1, the figures showed that they were reasonably proportional to length (*L*) for a given width (*W*). For L_1, the data for *W*=150µm appeared to be somewhat off the overall trend, similar to what was observed in Figure 6-4. However, for a given width, an acceptable linear relationship seemed to also exist between L_1 and $1/L$. The general consistencies between the trends shown by the data on the length dependence and those predicted by the beam model is a further confirmation that the one dimensional model is reasonable for the pMUTs fabricated in this study.

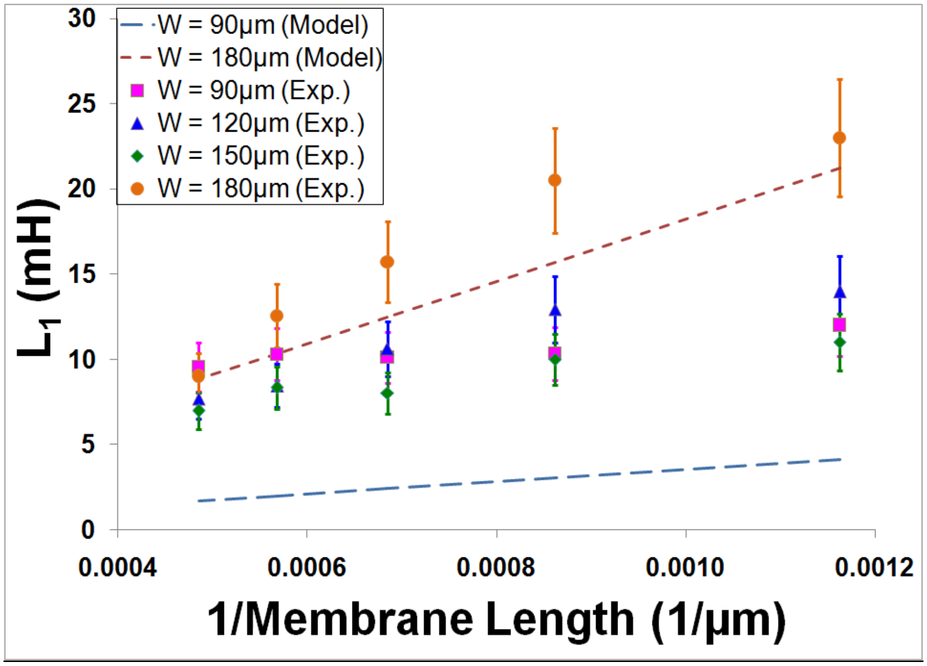

Figure 6-9: Motional inductance (*L_1*) as a function of membrane dimensions. Dash-dot and dashed lines represent the calculated results based on the composite beam model for the membranes with the smallest (*W* = 90μm) and the largest width (*W* = 180μm), respectively.

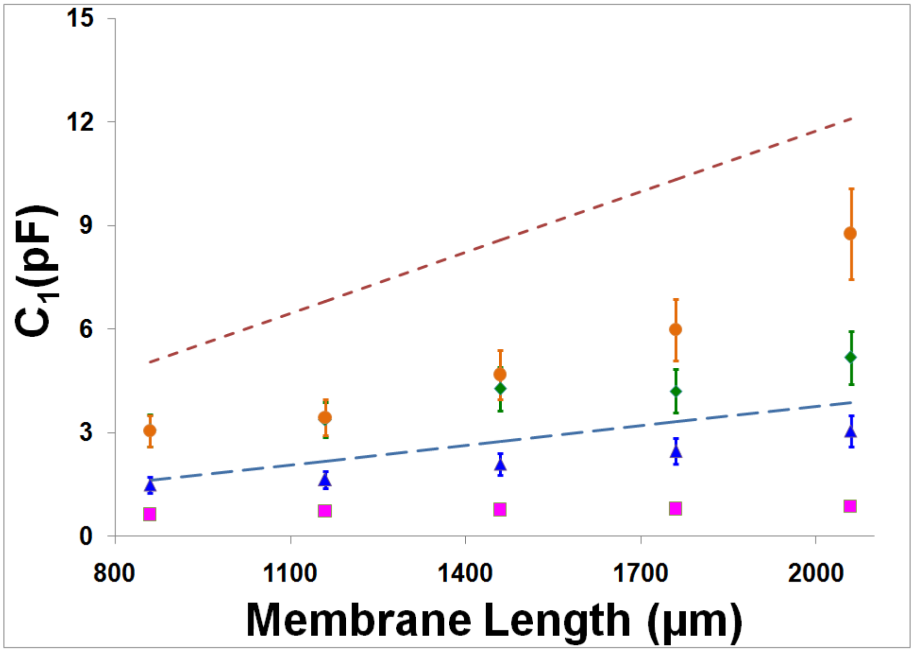

Figure 6-10: Motional capacitance (*C_1*) as a function of membrane dimensions. See Figure 6-9 for the legends.

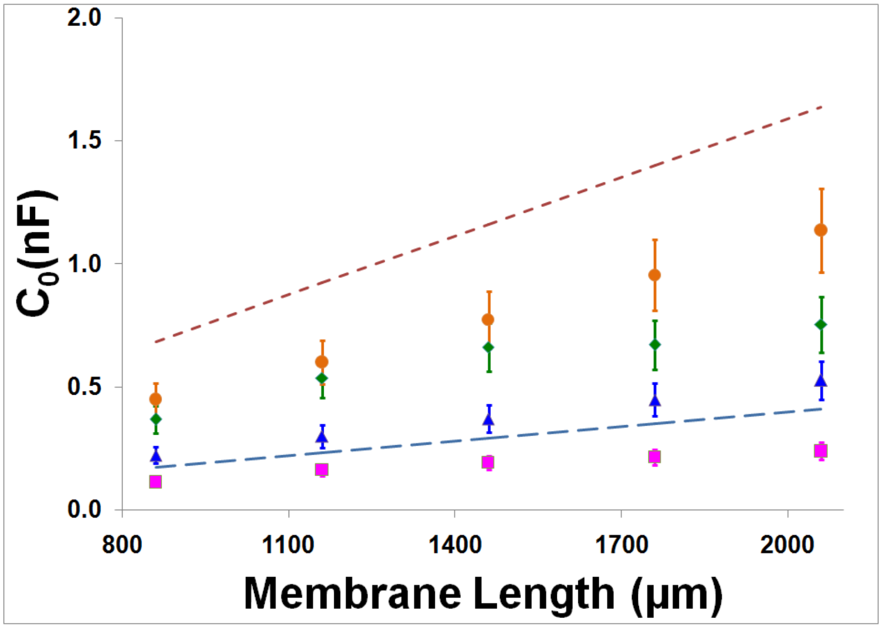

Figure 6-11: Parallel capacitance (C_0) as a function of membrane dimensions before (a) and after (b) considering parasitic capacitance. See Figure 6-9 for the legends.

6.5 Effects of Residual Stress

The analysis reported so far has not considered the effect of residual stress which is inherent in the thin film structures as a result of thermal-mechanical fabrication process. Unfortunately, residual stress is a quantity that is very difficult to quantify despite many efforts that have been devoted to this area. A recent effort can be found in [93]. Thus, the effect of residual stress was investigated through some preliminary parametric studies and the results are presented here.

Following the work reported in [28], the contribution of residual stress was modeled as a surface tension (T). With T included, Eqn. (6-1) can be modified as

$$\bar{\rho}\frac{\partial^2 \mathrm{w}}{\partial t^2}-\frac{\partial^2 M}{\partial x^2}-T\frac{\partial^2 \mathrm{w}}{\partial x^2}=F\ , \tag{6-36}$$

and the resultant electromechanical model is essentially the same as that derived in Section 6.2 except that Eqn. (6-13) needs to be modified as

$$s = KL\Lambda_4 - LT\Lambda_2\ , \tag{6-37}$$

where $\Lambda_2 = \int_0^w \Phi_1 \Phi_1^{''} dx$ (6-38)

The simulated results on the effects of residual stress on resonance frequency and coupling coefficient are shown in Figure 6-12 and Figure 6-13, respectively. These figures show that as the model gets closer to reality by including the residual stress effect, the quantitative predictions can also be further improved.

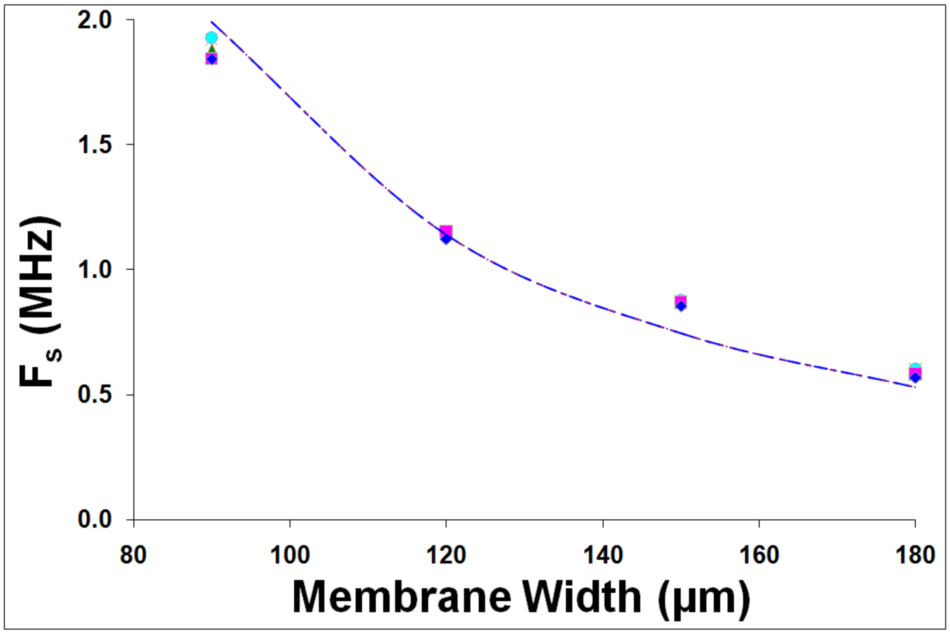

(a)

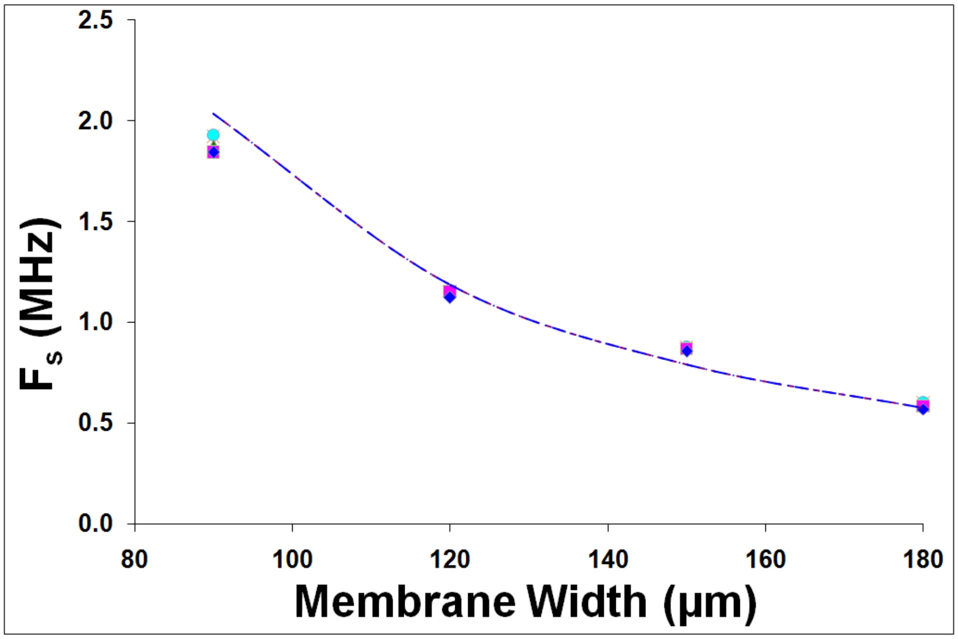

(b)

Figure 6-12: Parametric study of the residual stress effect on resonance frequencies. (a) T = 100 N/m; (b) T = 200 N/m. See Figure 6-7 for the case where T = 0.

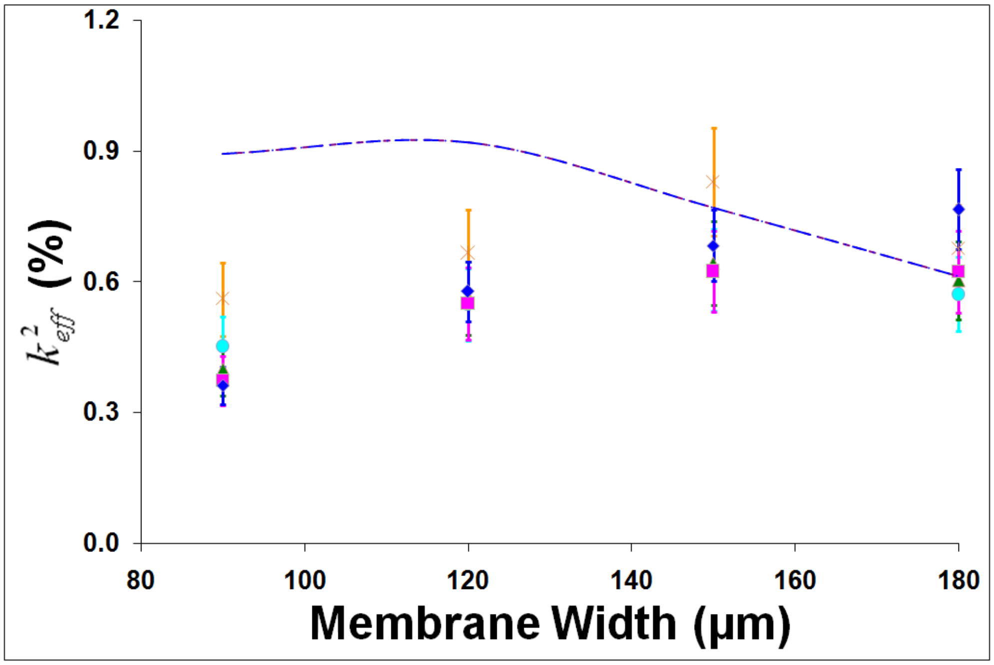

(a)

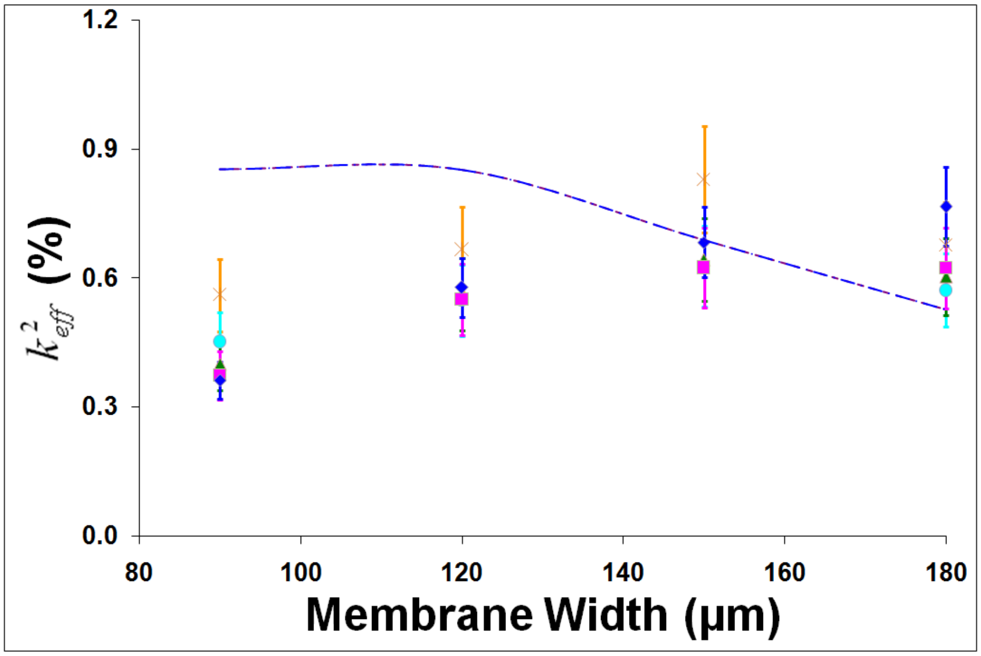

(b)

Figure 6-13: Parametric study of the residual stress effect of residual stress on the coupling coefficients. (a) T = 100 N/m; (b) T = 200 N/m. See Figure 6-8 for the case where T = 0.

6.6 Discussion

The pMUTs presented in this study represent the first generation of our design. As shown by the experimental data and analyses, the coupling coefficients based on this design are quite low. As demonstrated in the last section, the existence of residual stress could reduce the coefficient. Another possible reason is that this particular design may have imposed two much constraint on the membrane motion and thus induce a very high stiffness for the structure. Further work is currently under way to improve the design.

6.7 Conclusions

In this chapter, a one-dimensional composite beam model was used to correlate the equivalent circuit components with the structural parameters, and gain insights into the performance characteristics of pMUTs. The resonant frequencies were observed to decrease with the width of the membrane, but have no appreciable length dependence. With the correction of parasitic capacitance, the effective coupling coefficients were observed to increase with the width up to around 150µm and then decrease. However, they did not show clear and consistent length dependence. The variation of the coupling coefficient as a function of width of the membrane was shown to be mainly due to the relative ratios between the electrode and membrane widths rather than the membrane width itself. Although the model presented in this study was a simple one-dimensional electro-mechanical model, it did seem to offer both good qualitative and quantitative insights into the performance of pMUTs and provide a convenient tool for designing thin membrane transducers with large aspect ratio. The model can also take into consideration of the residual stress effect and offer an even more realistic prediction. The pMUTs presented in this study represent the first generation of our design. Further work is under way to improve the performance of the pMUTs especially the coupling coefficients.

CAHPTER 7

7 Two Dimensional Analytical Solution for pMUTs

7.1 Introduction

To gain some insights into the physical significance of the equivalent circuit components, a one-dimensional electromechanical model was used to study the correlation between the circuit components and structural parameters for pMUTs in the previous chapter. One-dimensional theory was used because the membranes had a long, slender shape; the length to width aspect ratios ranged from 5:1 to 23:1 with more than half of them having an aspect ratio greater than 10. Because of the large aspect ratios, the pMUT was idealized as a one-dimensional structure, with its length assumed to be infinitely large compared to its width. To increase the design flexibility, both length and width of the membranes need to be varied. In this regard, the one dimensional model needs to be extended to two dimensional. This chapter deals with the development of such model.

7.2 2D Composite Plate Model

A schematic diagram of the plate and its geometric correlations with the pMUT studied in this chapter is shown in Figure 7-1, where the layer with thickness h is made of an active piezoelectric material and the layer with thickness d is made of a passive elastic material. The gray area in Figure 7-1 represents top electrode which covers the area of $a \le x \le b$ in x direction and $c \le y \le d$ in y direction. The neutral surface, shown as dotted lines, is at $z=0$ and its vertical deflection is designated by *w(x,y,t)*. The distance between the bottom side and the neutral plane of the plate is *z**. As mentioned earlier, for the pMUTs fabricated in this study, *a=c=30*µm.

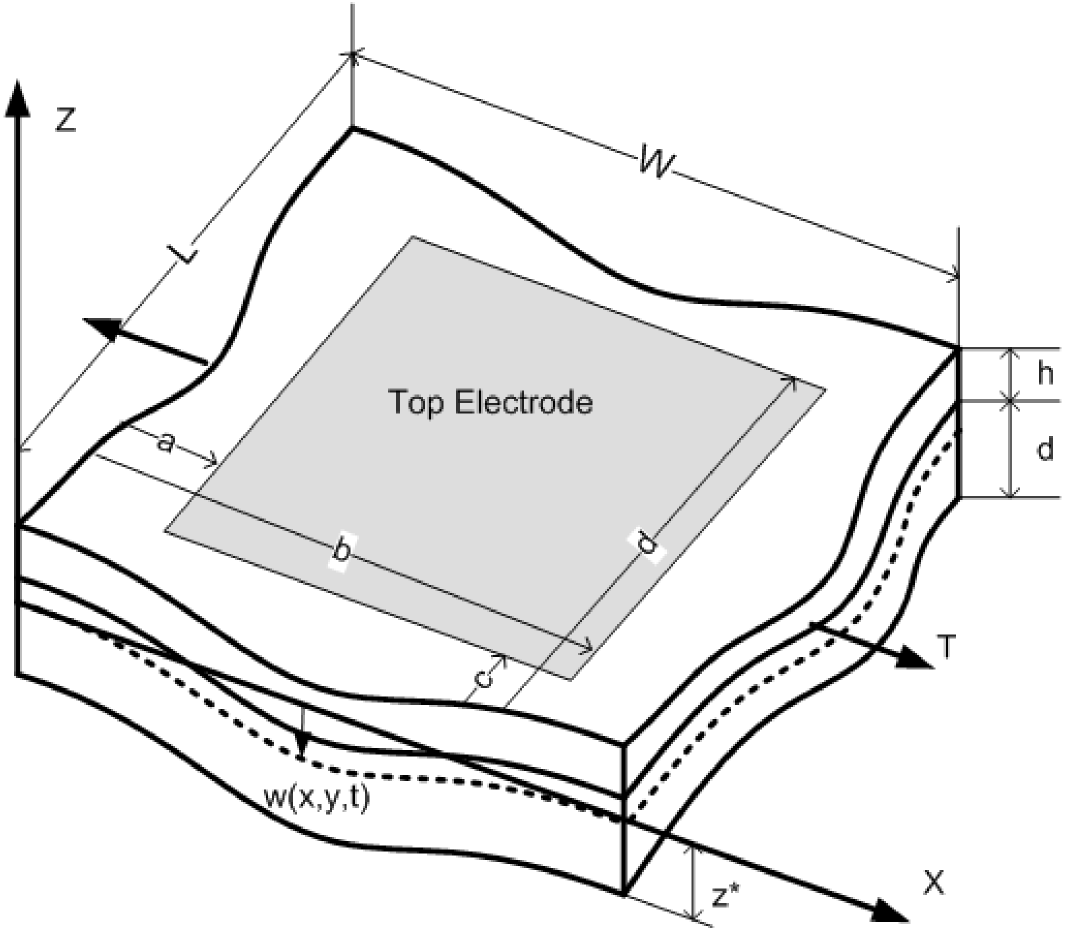

Figure 7-1: Two dimensional composite plate model.

The relevant governing equations for two-dimensional plate are listed in the following. The equation of motion was derived to be in the following form:

$$\bar{\rho}\frac{\partial^2 w}{\partial t^2}-\frac{\partial^2 M_{xx}}{\partial x^2}-2\frac{\partial^2 M_{xy}}{\partial x \partial y}-\frac{\partial^2 M_{yy}}{\partial y^2}=F(t) \tag{7-1}$$

where $\bar{\rho}=\rho_d d+\rho_h h$ is the mass per unit area with ρ_d and ρ_h being the densities of the passive elastic and active piezoelectric layers, respectively, $(M_{\mathrm{xx}}, M_{xy}, M_{yy})$ are the bending moment per unit length, *w(x,y,t)* is the displacement of the neutral surface, and $F(t)$ is an applied vertical force per unit area. In Ref. [28], the equation of motion for one-dimensional model also contains the effect of applied tension *T* to account for residual stress in the membrane. In this study, the membrane is assumed to be free of residual stress because the size effect of the pMUTs is the main concern. The residual stress is a complicated issue and needs to be addressed in a separate study.

Under the two-dimensional plate assumptions, the relevant constitutive equations for piezoelectric material are given as:

$$S_1 = s_{11}^E T_1 + s_{12}^E T_2 + d_{31} E_3 , \tag{7-2}$$

$$S_2 = s_{12}^E T_1 + s_{22}^E T_2 + d_{31} E_3 , \tag{7-3}$$

$$S_{12} = s_{66}^E T_{12} , \tag{7-4}$$

$$D_3 = d_{31} T_1 + d_{31} T_2 + \varepsilon_{33}^T E_3 , \tag{7-5}$$

where *S*, *T*, *E*, and *D* are strain, stress, electric field, and electric displacement, respectively; s_{ij}, d_{ij}, and ε_{ij} are mechanical compliance, piezoelectric constant, and dielectric permittivity, respectively; the superscripts '*E*' and '*T'* represent the states of constant electric field and constant stress, respectively, which are usually zeros; and the indices *1, 2,* and *3* indicate the directions in *x, y,* and *z*, respectively. For the passive elastic layer, the piezoelectric (d_{ij}) and dielectric (ε_{ij}) constants are zero.

Strain-displacement relations are given as the function of vertical displacement in the following form:

$$S_1 = u,_x - zw,_{xx} \tag{7-6}$$

$$S_2 = v,_y - zw,_{yy} \tag{7-7}$$

$$S_{12} = -zw,_{xy} \tag{7-8}$$

where $'xx$ implies second derivative of *x* and so on. (u, v, w) are the displacements in *x*, *y*, and *z* directions and (u, v) are assumed to be zero. Using the strain-displacement relations and Eqns. (7-2) and (7-4), T_1, T_2, and T_{12} are written as

$$T_1 = \frac{S_1 s_{11}^E - S_2 s_{12}^E - d_{31}\left(s_{11}^E - s_{12}^E\right)E_3}{\left(s_{11}^E\right)^2 - \left(s_{12}^E\right)^2} \tag{7-9}$$

$$T_2 = \frac{S_1 s_{12}^E - S_2 s_{11}^E - d_{31}\left(s_{12}^E - s_{11}^E\right)E_3}{\left(s_{12}^E\right)^2 - \left(s_{11}^E\right)^2} \tag{7-10}$$

$$T_{12} = \frac{2}{s_{66}^E} S_{12} \tag{7-11}$$

By substituting Eqns. (7-9) and (7-10) into Eqn. (7-4) and (7-5), D_3 can be written as function of S_1, S_2, and E_3 only.

$$D_3 = \frac{d_{31}}{s_{11}^E + s_{12}^E}\left(S_1 + S_2\right) + \left(\varepsilon_{33}^T - \frac{2d_{31}^2}{s_{11}^E + s_{12}^E}\right)E_3 \tag{7-12}$$

Integrate Eqn. (7-12) through the thickness of the second layer to rewrite D_3 in terms of voltage $\left(V = -\int E_3 dz\right)$ and vertical displacement *w(x,y,t)* using Maxwell Equation $\partial D_3 / \partial z = 0$.

$$D_3 = -\frac{1}{h}\left(\varepsilon_{33}^T - \frac{2d_{31}^2}{s_{11}^E + s_{12}^E}\right)V - \frac{d_{31}}{s_{11}^E + s_{12}^E}\left(d - z^* + \frac{h}{2}\right)\left(\frac{\partial^2 w_0}{\partial x^2} + \frac{\partial^2 w_0}{\partial y^2}\right) \tag{7-13}$$

E_3 can be rewritten as function of T_1, T_2, and D_3 from Eqn. (7-5) as follows.

$$E_3 = \frac{1}{\varepsilon_{33}^T} D_3 - \frac{d_{31}}{\varepsilon_{33}^T} T_1 - \frac{d_{31}}{\varepsilon_{33}^T} T_2 \tag{7-14}$$

Substitute Eqn. (7-14) into Eqns. (7-9) and (7-10) to get equations of T_1 and T_2 as function of $S_1, S_2,$ and D_3.

$$T_1 = \kappa_1 S_1 - \kappa_2 S_2 - \kappa_3 H(x,y) D_3 \tag{7-15}$$

$$T_2 = -\kappa_2 S_1 + \kappa_1 S_2 - \kappa_3 H(x,y) D_3 \tag{7-16}$$

where

$$\kappa_1 = \left(s_{11}^E - d_{31}^2 / \varepsilon_{33}^T\right) \Big/ \left(s_{11}^E - s_{12}^E\right)\left(s_{11}^E + s_{12}^E - 2\,d_{31}^2 / \varepsilon_{33}^T\right) \tag{7-17}$$

$$\kappa_2 = \left(s_{12}^E - d_{31}^2 / \varepsilon_{33}^T\right) \Big/ \left(s_{11}^E - s_{12}^E\right)\left(s_{11}^E + s_{12}^E - 2\,d_{31}^2 / \varepsilon_{33}^T\right) \tag{7-18}$$

$$\kappa_3 = \frac{d_{31}}{s_{11}^E \varepsilon_{33}^T + s_{12}^E \varepsilon_{33}^T - 2 d_{31}^2} \tag{7-19}$$

and $H(x,y)$ is Heaviside function so that $H(x,y)=1$ for $a < x < b, c < y < d$ and $H(x,y) = 0$ in other case. For the elastic layer, $\kappa_1, \kappa_2,$ and κ_3 need to be modified as necessary because the piezoelectric (d_{ij}) and dielectric (ε_{ij}) constants are zeros.

$M_{xx}, M_{yy},$ and M_{xy} are the moment per unit length in the membrane and they can be calculated using the stresses $T_1, T_2,$ and T_{12} as shown below.

$$\begin{aligned} M_{xx} &= \int_{-z^{*`}}^{d-z^*} z T_{1elsatic} dz + \int_{d-z^{*`}}^{d-z^*+h} z T_{1PZT} dz \\ &= -K_1 \frac{\partial^2 w}{\partial x^2} + K_2 \frac{\partial^2 w}{\partial y^2} - \xi H V + H \zeta \left(w,_{xx} + w,_{yy}\right) \end{aligned} \tag{7-20}$$

$$\begin{aligned} M_{yy} &= \int_{-z^{*`}}^{d-z^*} z T_{2elsatic} dz + \int_{d-z^{*`}}^{d-z^*+h} z T_{2PZT} dz \\ &= K_2 \frac{\partial^2 w}{\partial x^2} - K_1 \frac{\partial^2 w}{\partial y^2} - \xi H V + H \zeta \left(w,_{xx} + w,_{yy}\right) \end{aligned} \tag{7-21}$$

$$
\begin{aligned}
M_{xy} &= \int_{-z^{*`}}^{d-z^{*}} zT_{12elsatic}dz + \int_{d-z^{*`}}^{d-z^{*}+h} zT_{12PZT}dz \\
&= -\left(\frac{2d}{s_{66}^{E}}\frac{\partial^2 w}{\partial x \partial y}\Theta_1\right)_{elastic} - \left(\frac{2h}{s_{66}^{E}} w,_{xy}\Theta_2\right)_{PZT}
\end{aligned}
\tag{7-22}
$$

where $K_1, K_2, \Theta_1, \Theta_2, \xi, \text{and } \zeta$ are given as below.

$$K_1 = \left[\kappa_{1elastic} d\Theta_1 + \kappa_{1PZT} h\Theta_2\right]$$

$$K_2 = \left[\kappa_{2elastic} d\Theta_1 + \kappa_{2PZT} h\Theta_2\right]$$

$$\Theta_1 = \left(\frac{d^2}{3} - dz^* + z^{*2}\right)$$

$$\Theta_2 = \left(d^2 + z^{*2} - 2dz^* + hd - hz^* + \frac{h^2}{3}\right)$$

$$\xi = \kappa_3\left(d - z^* + \frac{h}{2}\right)\left(\varepsilon_{33}^{T} - \frac{2d_{31}^{2}}{s_{11}^{E} + s_{12}^{E}}\right)$$

$$\zeta = \kappa_3 h \frac{d_{31}}{s_{11}^{E} + s_{12}^{E}}\left(d - z^* + \frac{h}{2}\right)^2$$

Now substitute Eqns. (7-20), (7-21), and (7-22) into Eqn. (7-1) to get the equation of motion as function of vertical displacement *w(x,y,t)* as follows.

$$
\begin{aligned}
&\bar{\rho} w,_{tt} + K_1 w,_{xxxx} - 2K_2 w,_{xxyy} + K_1 w,_{yyyy} + \xi H,_{xx} V + \xi H,_{yy} V \\
&-\left[H,_{xx}\zeta\left(w,_{xx} + w,_{yy}\right) + 2H,_{x}\zeta\left(w,_{xxx} + w,_{xyy}\right) + H\zeta\left(w,_{xxxx} + w,_{xxyy}\right)\right] \\
&+\left(4d/s_{66}^{E}\, w,_{xxyy}\Theta_1\right)_{elastic} + \left(4d/s_{66}^{E}\, w,_{xxyy}\Theta_2\right)_{PZT} \\
&-\left[H,_{yy}\zeta\left(w,_{xx} + w,_{xxyy}\right) + 2H,_{y}\zeta\left(w,_{xxy} + w,_{yyy}\right) + H\zeta\left(w,_{xxyy} + w,_{yyyy}\right)\right] = F(t)
\end{aligned}
\tag{7-23}
$$

The applied voltage (*V*) generates the line moments at the perimeter of the electrode. To get a lumped parameter model, the forces caused by coupling with the derivatives of the plate displacement are neglected. Under this assumption, the equation of motion is simplified as

$$\begin{aligned}&\bar{\rho} w_{,tt} + K_1 w_{,xxxx} - 2K_2 w_{,xxyy} + K_1 w_{,yyyy} + \xi H_{,xx} V + \xi H_{,yy} V \\ &+ \left(4d/s_{66}^E\, w_{,xxyy}\Theta_1\right)_{elastic} + \left(4d/s_{66}^E\, w_{,xxyy}\Theta_2\right)_{PZT} = F(t)\end{aligned} \tag{7-24}$$

Gauss' law is applied to the electrode area to calculate the free charge Q accumulated on the electrode using the electric displacement as shown in Eqn. (7-13). The result is a relation between the free charge accumulated on the electrode and the deflection of the membrane.

$$Q = \frac{(b-a)(d-c)}{h}\left(\varepsilon_{33}^T - \frac{2d_{31}^2}{s_{11}^E + s_{12}^E}\right)V - \frac{d_{31}}{s_{11}^E + s_{12}^E}\left(d - z^* + \frac{h}{2}\right)\int_a^b\int_c^d \left(w_{,xx} + w_{,yy}\right)dxdy \tag{7-25}$$

The displacement of the membrane can be expressed by mode superposition and fundamental mode approximation as also used in 1D theory.

$$w(x,y,t) = \sum_n \Phi_n(x,y)g_n(t) \approx \Phi_1(x,y)g_1(t) \tag{7-26}$$

where Φ_n and g_n represent the mode shape and mode coordinate for the n^{th} normal mode, respectively. Substituting Eqn. (7-26) into the complete set of electro-mechanical equations yields a two-port, lumped electromechanical model in the following form.

$$m\ddot{g}_1 + sg_1 + \Psi V = \bar{F}(t) \tag{7-27}$$

and

$$Q = C_0 V + \Psi g \tag{7-28}$$

where

$$m = \bar{\rho}\Lambda_0 \tag{7-29}$$

$$s = K_1\left(\Lambda_{xxxx} + \Lambda_{yyyy}\right) - 2K_2\Lambda_{xxyy} + \left(4d/s_{66}^E\,\Theta_1\right)_{elastic}\Lambda_{xxyy} + \left(4d/s_{66}^E\,\Theta_2\right)_{PZT}\Lambda_{xxyy} \tag{7-30}$$

$$\Psi = \xi\int_0^W\int_0^L \left(\Phi_1 H_{,xx} + \Phi_1 H_{,yy}\right)dxdy \tag{7-31}$$

$$\overline{F}(t)=\int_{c}^{d}\int_{a}^{b}\Phi_1 F(t)dxdy \tag{7-32}$$

$$C_0=\frac{(b-a)(d-c)}{h}\left(\varepsilon_{33}^{T}-\frac{2d_{31}^{2}}{s_{11}^{E}+s_{12}^{E}}\right) \tag{7-33}$$

with $\Lambda_0=\int_0^W\int_0^L\Phi_1^2dydx$, $\Lambda_{xxxx}=\int_0^W\int_0^L\Phi_1\Phi_{1'xxxx}dydx$, $\Lambda_{xxyy}=\int_0^W\int_0^L\Phi_1\Phi_{1'xxyy}dydx$, and

$\Lambda_{yyyy}=\int_0^W\int_0^L\Phi_1\Phi_{1'yyyy}dydx$.

Eqn. (7-27) can be rewritten as

$$\frac{m}{\Psi^2}(\Psi\ddot{g}_1)+\frac{s}{\Psi^2}(\Psi g_1)+V=\frac{\overline{F}}{\Psi}. \tag{7-34}$$

Eqns. (7-28) and (7-34) constitute a two-port electromechanical model and the corresponding equivalent circuit parameters are given as

$$L_1=\frac{m}{\Psi^2}, \tag{7-35}$$

and $C_1=\frac{\Psi^2}{s}$. (7-36)

In Eqn. (7-34), damping effect was not considered for the same reason as one-dimensional case in the previous chapter.

Based on the derived equivalent circuit parameters from two-dimensional analysis solution, resonance frequency (f_s) and effective coupling coefficient (k_{eff}^2) can be established by the Eqns. (4-1) and (4-3) which are rewritten here.

$$f_r=\frac{1}{2\pi\sqrt{L_1C_1}}$$

$$k_{eff}^2 = \frac{C_1}{C_0 + C_1} = \frac{f_p^2 - f_s^2}{f_p^2}$$

7.3 Prediction of pMUTs Performance Based on 2D Plate Model

After the correlation between the equivalent circuit components and structural parameters are established in the previous section, the comparison between the experimental and the modeling results are performed to validate the two-dimensional composite plate model. The boundary is assumed to be clamped conditions for the same reason as one-dimensional case, i.e. $\Phi(0) = \Phi(W) = \Phi'(0) = \Phi'(W) = 0$ in x direction and $\Phi(0) = \Phi(L) = \Phi'(0) = \Phi'(L) = 0$ in y direction. Under this boundary condition, $\Phi_1(x)$ can be represented as following [79]:

$$\Phi_1 = C\left(\frac{x}{W}\right)^2 \left(1 - \frac{x}{W}\right)^2 \left(\frac{y}{L}\right)^2 \left(1 - \frac{y}{L}\right)^2 \tag{7-37}$$

To evaluate the size dependence of the equivalent circuit components, we need to evaluate $\left(\Lambda_0, \Lambda_{xxxx}, \Lambda_{xxyy}, \Lambda_{yyyy}\right)$ in Eqns. (7-29) and (7-30), respectively. Eqn. (7-27) is useful for the analysis of the effect of the relative dimensions between the electrode and membrane on the electromechanical behavior of the pMUT structure without damping. However, more precise prediction of the membrane behavior requires much more detailed analysis. For example, in deriving Eqn. (7-27), only the fundamental mode was considered. Superposition of higher order modes may be necessary for more accurate analysis. In addition, the nonlinearity of the membrane may also need to be taken into consideration.

The prediction of pMUTs performance can be done by using the developed two-dimensional model. This prediction can show the accuracy of this model by comparing with the experimental data combined with the equivalent circuit analysis. The model is an important tool for designing new pMUTs to predict their performance, especially for resonance frequency and effective coupling coefficient, before fabrication. They are also can be used for the analysis of other types of ultrasound transducers and energy conversion devices which are using piezoelectric thin film as a sensing/actuation component.

Clamped boundary condition is adopted for the boundary conditions at $x=y=0$, $x=W$, and $y = L$. Calculations are performed for all the different size of the pMUTs which were fabricated for this study. Since the modeled plate is a two-layer composite structure which is different from the multi-layered pMUT, effective density and Young's modulus were used in the calculation. The material properties and layer thicknesses used in the calculations are listed in Table 6-1. The bottom layer of the plate, which has a thickness d, was assumed to consist of silicon and SiO_2 layers, and the top layer, which has a thickness h, was assumed to consist of the platinum, PZT, and gold layers of the actual pMUT. The effective density and Young's modulus were defined the same as one-dimensional case and they are given here for the convenience of reading.

$$\rho_{eff} = \sum_{k=1}^{n} \rho_k t_k \Big/ \sum_{k=1}^{n} t_k \qquad\qquad E_{eff} = \sum_{k=1}^{n} E_k t_k \Big/ \sum_{k=1}^{n} t_k$$

The constant C in Eqn. (7-37) had no effect on the calculated results and was arbitrarily set to 1. The predicted results using the effective density and Young's modulus for the membranes with the largest (L = 2060µm) and the smallest length (L = 860µm) are included in Figure 7-2 through Figure 7-6 as dash-dot and dashed lines, respectively. The results for other lengths fall in between these two lines and are not shown in these figures.

The calculated overall trend for L_1 was consistent with the experimental data as shown in Figure 7-2. Quantitatively, the calculations were matched quite well with the data for the membranes with the width W greater than 150µm, but underestimated the inductance L_1 for widths less than 150µm. Figure 7-3 showed the trend for calculated C_1 and it was also consistent with the experimental observations although the calculations slightly overestimated the experimentally measured values. The calculations also showed a nonlinear dependence on width. For C_0 and f_s, the predictions compared quite well with the data both qualitatively and quantitatively as shown in Figure 7-4 and Figure 7-5.

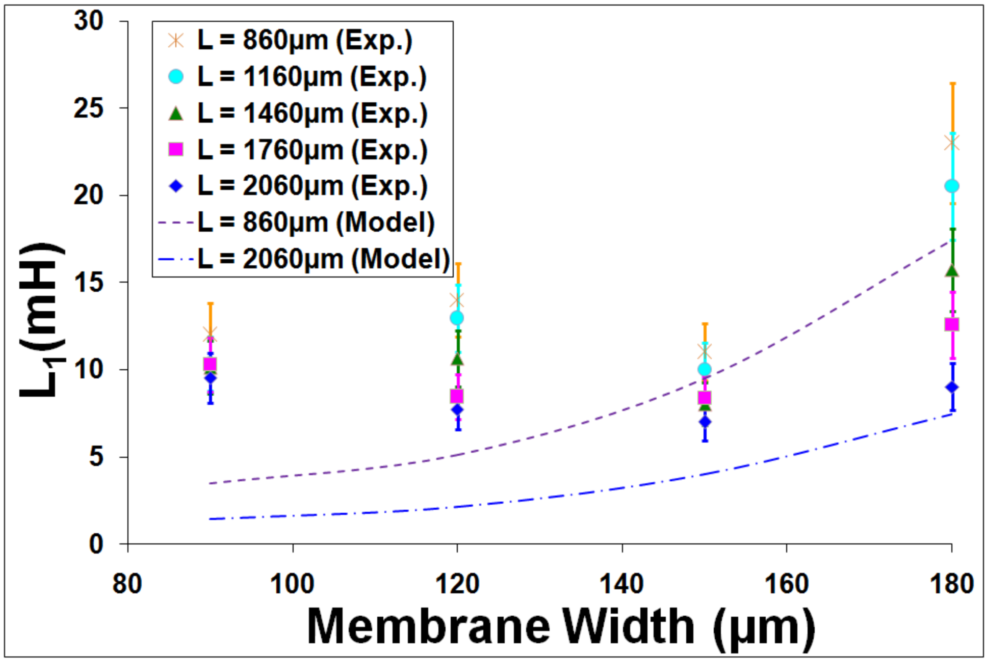

Figure 7-2: Motional inductance (L_1) as a function of membrane dimensions. Dash-dot and dashed lines represent the calculated results based on the 2D composite plate model for the membranes with the largest (L = 2060µm) and the smallest length (L = 860µm), respectively.

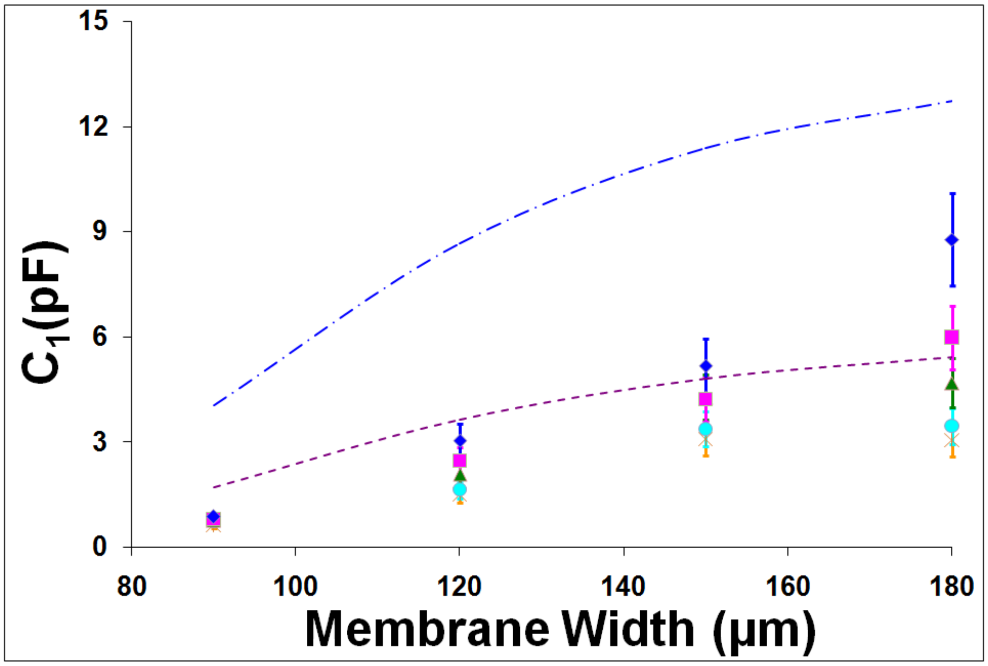

Figure 7-3: Motional capacitance (C_1) as a function of membrane dimensions. See Figure 7-2 for the legends.

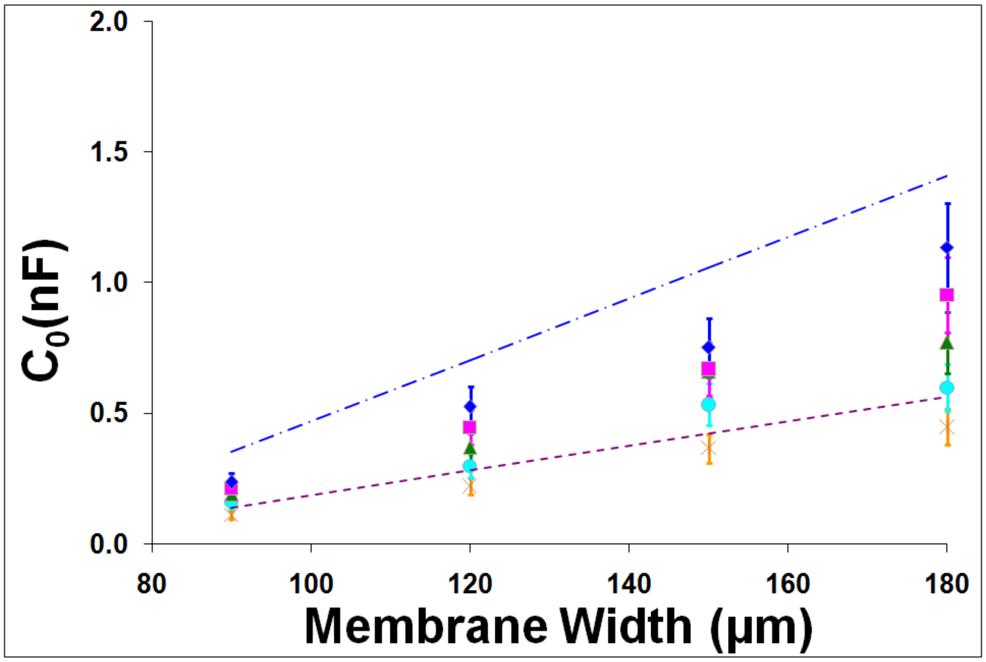

Figure 7-4: Parallel capacitance (C_0) as a function of membrane dimensions after considering parasitic capacitance. See Figure 7-2 for the legends.

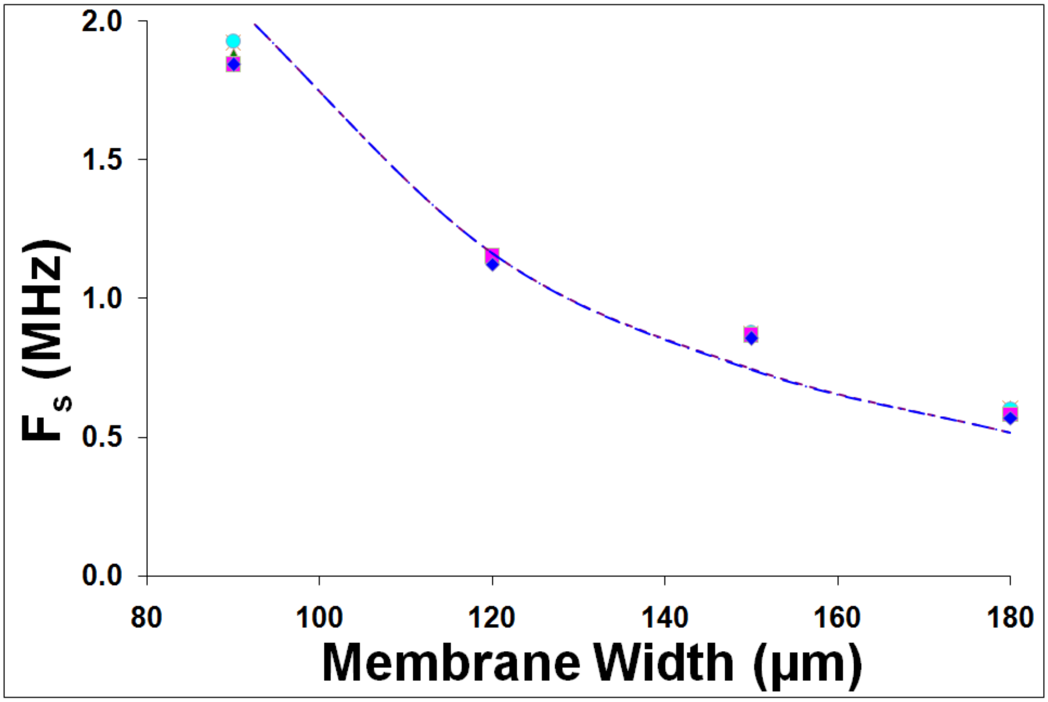

Figure 7-5: Resonance frequency (f_s) as a function of membrane dimensions. Figure 7-2 for the legends.

For the effective coupling coefficient $\left(k_{eff}^2\right)$ shown in Figure 7-6, the calculations slightly overestimated the experimentally measured values for the membranes with W less than 150µm, while there was agreement for widths above this value. As mentioned earlier, the experimentally measured k_{eff}^2 increased with the width up to around $W=150$µm and then started to decrease. This behavior was also observed in the predictions, although the predicted maximum k_{eff}^2 was observed to occur at the width of around $W=120$µm. Furthermore, k_{eff}^2 had dependence on membrane length which was difference from f_s where no dependence on length was found. This length dependence on k_{eff}^2 was presented by the calculation as well.

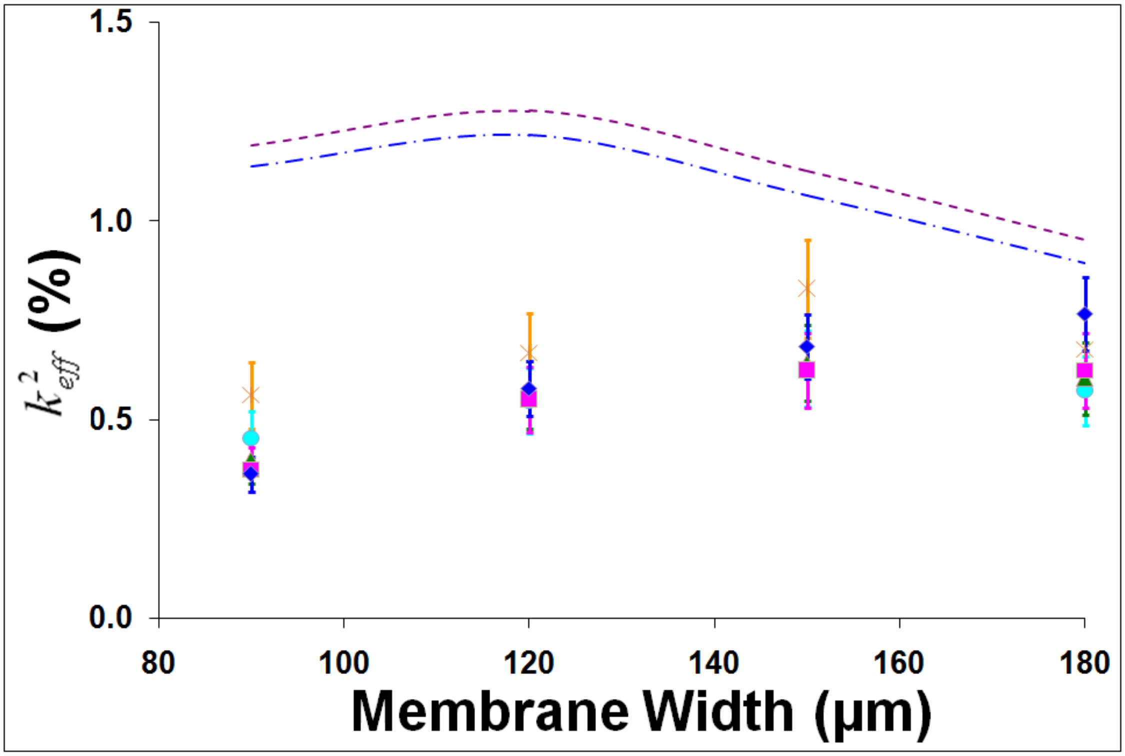

Figure 7-6: Effective coupling coefficient (k_{eff}^2) as a function of membrane dimensions after considering parasitic capacitance. Figure 7-2 for the legends.

7.4 Optimization of Design Parameters Using Two-Dimensional Model

Once the developed two-dimensional plate model is validated, we can now use this model to predict the performance of pMUTs to find better design parameters. This was done in two steps. First, the size of the membrane was varied while the top electrode coverage area was constant in percentage with respect to the membrane area. In other words, the size of the electrode was proportionally increased as the size of the membrane was increased. Secondly, the membrane size was kept constant and the electrode coverage was varied. In both cases, our main interests were on the resonance frequency and k_{eff}^2. Therefore, the values for electric circuit components were not presented for optimization process.

For the first case, membrane size was varied from 100µm to 2000µm by increment of 50µm for each step in x and y directions independently. The electrode was covered $0.3W \le x \le (W - 0.3W)$ and $0.3L \le y \le (L - 0.3L)$ where W and L were explained in Figure 7-1. All other conditions such as layer thicknesses and material properties were the same as explained in the previous section for the validation of the model. The calculated resonance frequencies as a function of membrane size were shown in Figure 7-7. The results are reasonable compared to the experimental data and expectable because increase of membrane size leads to the increase of the compliance of the structure and thus reduction of the fundamental frequency. Due to this reason, resonance frequency was suddenly increased when the size of the membrane was roughly smaller than 250 by 250µm. Figure 7-8 shows the k_{eff}^2 while membrane size was varied. It presents that k_{eff}^2 is higher with square membrane compared to rectangular membrane with high aspect ratios. Based on these results, we will further investigate only square membranes for the second step, i.e. the membrane size was kept constant and the electrode coverage was varied.

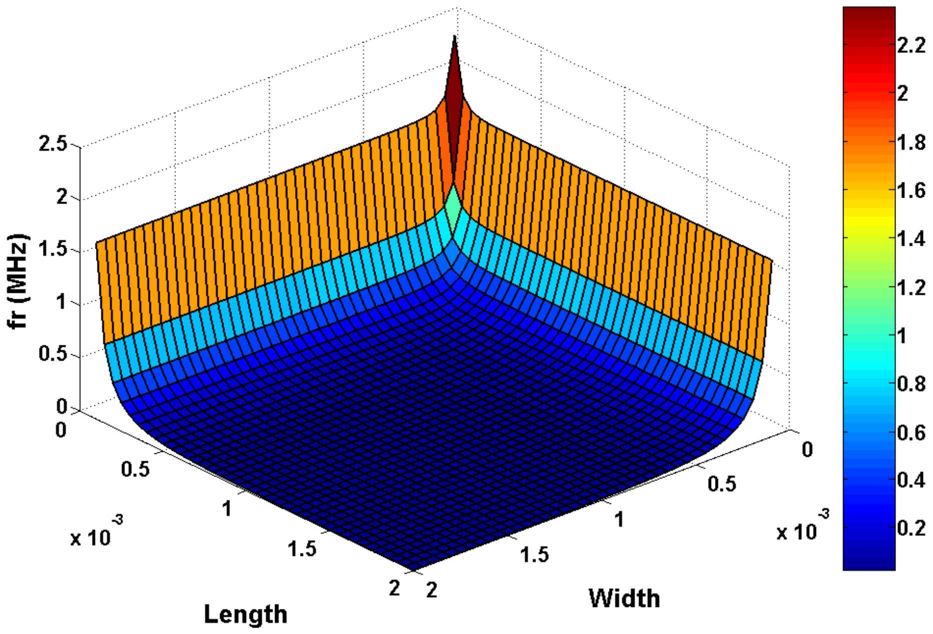

Figure 7-7: Calculated frequency (f_s) while membrane size was varied.

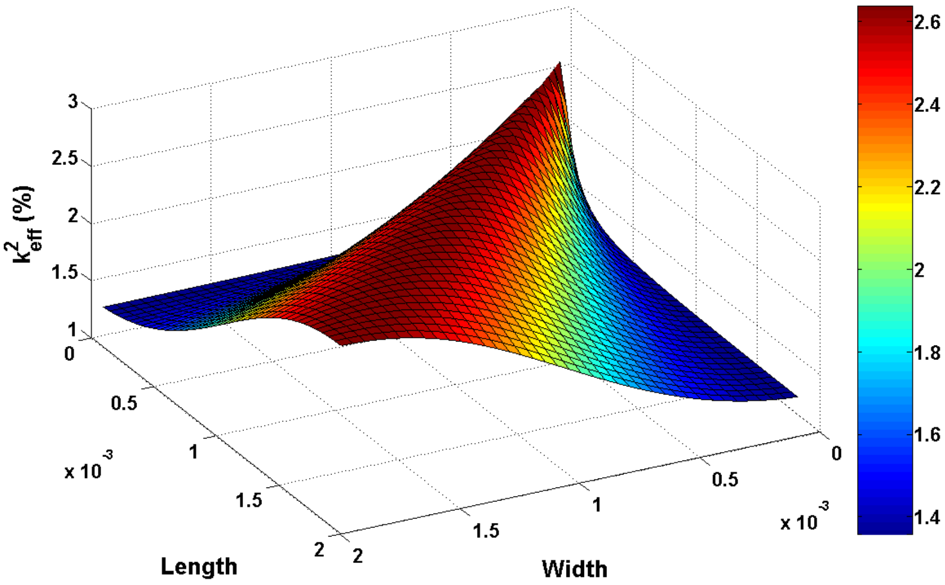

Figure 7-8: Calculated effective coupling coefficient (k^2_{eff}) while membrane size was varied.

Two different membrane sizes were used for optimization of top electrode area. Membrane sizes used in this case were 100 by 100µm and 500 by 500µm. The area covered by the top electrode in x and y directions from the center of the membrane was calculated by $(b-a)/W$ and $(d-c)/L$ where a, b, c, d, W, and L were introduced in Figure 7-1. Because of the clamped boundary conditions were used in this study, the calculation was not conducted for the case when electrode covers the entire membrane to avoid k_{eff}^2 being zero. The calculated resonance frequencies were 2.37 MHz and 94.8 KHz for 100 by 100µm and 500 by 500µm membranes, respectively. The maximum predicted k_{eff}^2 was 2.908% in both cases and it was shown that the theoretically calculated k_{eff}^2 are only function of electrode coverage as shown in Figure 7-9. From Figure 7-9, it was found that k_{eff}^2 was maximized when the electrode covered about 48.9% in both x and y directions. In other words, k_{eff}^2 was maximized when the electrode covers about 23.9% of the square membrane from the center. Therefore, the relative ratios between the membrane and top electrode area mainly controlled k_{eff}^2 instead of the membrane size.

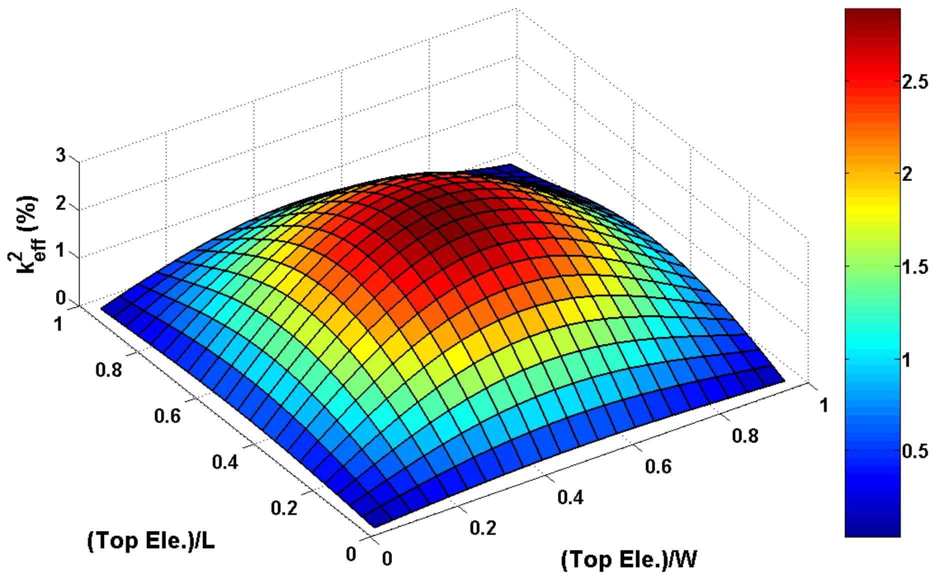

Figure 7-9: Calculated effective coupling coefficient (k^2_{eff}) as a function of electrode coverage for both 100µm by 100µm and 500µm by 500µm membranes.

7.5 Development of Graphical User Interface

For many practical engineers, using numerical or analytical tools in source code file format is not easy at the first time and it requires some time to be trained to use. Many times, computational work for special purposes is done in a programming language that is not easy to understand if one doesn't have programming background. Because of this kind of problems, engineers often hesitate to use a source code if he/she is not familiar with the programming language which was used to develop the source code. An alternative to this problem is providing a user friendly computational tool that can do the required engineering calculations or simulations and easy to use.

A FE model and two analytical solutions were introduced in Chapters 5, 6, and 7. Those numerical and analytical tools were used to model resonance frequency, mode shape, electromechanical coupling effect, etc. of pMUTs. However, those tools can potentially be used for other engineering purposes such as analysis of laminated composite plate, piezoelectric energy devices, simulation of MEMS sensors and actuators, etc. for engineers in other fields. For this reason, development of user friendly computational tools is beneficial for engineers who don't have strong computer programming background. A graphical user interface (GUI) is a common tool to develop user friendly software. Therefore, a GUI interface has been developed and it is in the process to upgrade.

The GUI introduced in this section is based on the two-dimensional composite plate theory and MATLAB 7.0 (R14) is used as a tool to develop. The GUI has four main files; FIG file which contains a complete description of the GUI layout and the components of the GUI such as push buttons, menus, axes, and so on [88], a main M-files for GUI, and two sub-functions to do analytical calculations based on the two-dimensional composite plate theory. A FIG file for the developed GUI is shown in Figure 7-10. With this GUI, user can select number of layers in membrane type transducer, material properties, size of membrane, top electrode coverage, etc. The size of membrane and the electrode coverage can be varied as shown in Figure 7-7, Figure 7-8, and Figure 7-9 so that many different cases can be solved as a time. This program can definitely help engineers in the design process for membrane type ultrasound transducer, piezoelectric energy harvesting devices, or composite plate.

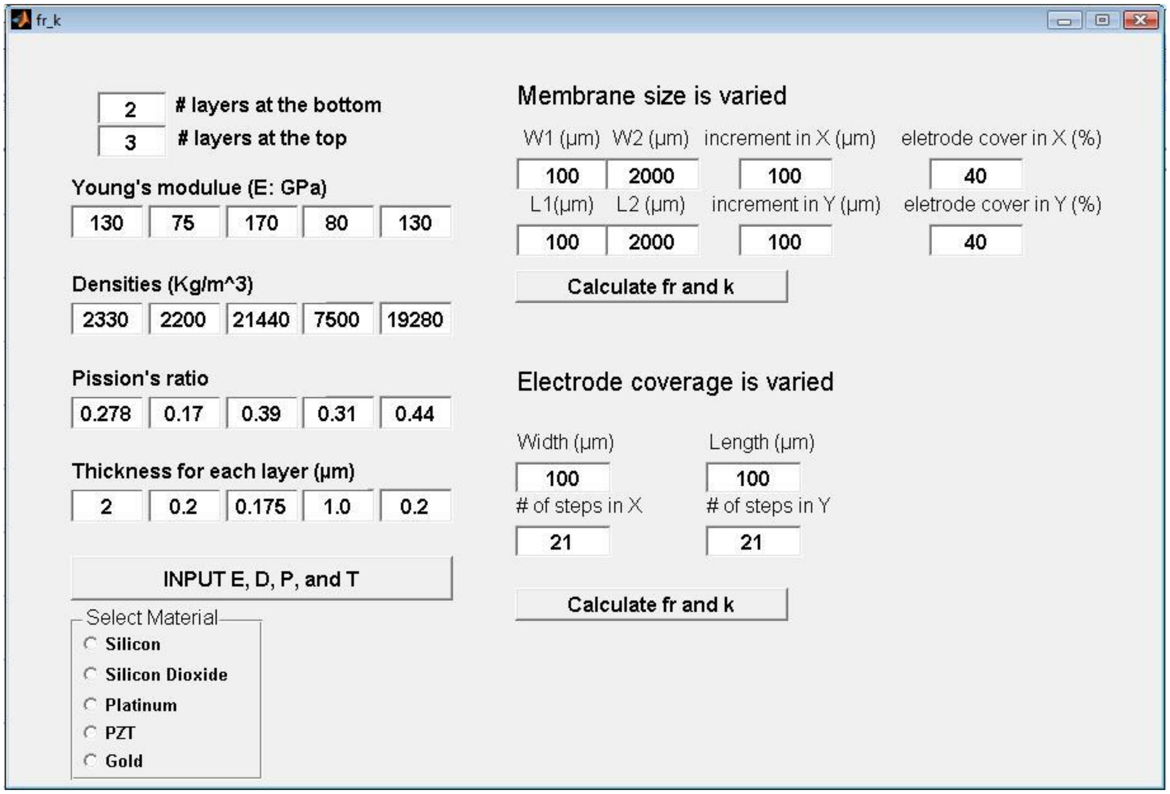

2 # layers at the bottom
3 # layers at the top

Young's modulue (E: GPa): 130 | 75 | 170 | 80 | 130

Densities (Kg/m^3): 2330 | 2200 | 21440 | 7500 | 19280

Pission's ratio: 0.278 | 0.17 | 0.39 | 0.31 | 0.44

Thickness for each layer (µm): 2 | 0.2 | 0.175 | 1.0 | 0.2

Membrane size is varied

W1 (µm): 100
W2 (µm): 2000
increment in X (µm): 100
eletrode cover in X (%): 40
L1(µm): 100
L2 (µm): 2000
increment in Y (µm): 100
eletrode cover in Y (%): 40

Electrode coverage is varied

Width (µm): 100
Length (µm): 100
# of steps in X: 21
# of steps in Y: 21

Figure 7-10: GUI to help the optimization of pMUTs design.

7.6 Conclusions

In this chapter, a two-dimensional composite plate model was developed for optimization of pMUTs. In the experimental side, the resonant frequencies were observed to decrease with the width of the membrane, but have no appreciable length dependence. It was well presented by the developed two-dimensional electromechanical model. Effective coupling coefficients were measured to increase with the width up to around 150µm and then decrease with considering parasitic capacitance. In the calculations, effective coupling coefficient started to decrease from around 130µm. It was found that resonance frequency was mainly controlled by the size of a membrane. Both the membrane size and electrode coverage have influence on effective coupling coefficient. However, it was shown that electrode coverage has a dominant effect on the effective coupling coefficient. Although the model presented in this study was a simple two-dimensional composite plate model for electromechanical coupling system, it did seem to provide both good qualitative and quantitative prediction on the performance of pMUTs. The model was also used to optimize the size of the membrane and the electrode coverage. The size dependence of the coupling coefficient was found to result mainly from the relative ratios between the electrode and membrane sizes rather than the membrane size itself. A GUI is also developed based on two-dimensional composite plate model.

CHAPTER 8

8 Conclusions and Recommendations

8.1 Conclusions

In this study, single element K_{31} type pMUT transducers have been fabricated and characterized. A prototype of 2D array transducer using the single element transducer as the building block has also been engineered. In addition, analytical models consisting a one dimensional composite beam and a two dimensional composite plate model and a finite element code based on a combination of the equivalent single-layer theory and the classical laminated plate theory (CLPT) have also been developed to analyze and model the performance of fabricated single element pMUTs.

For the pMUTs with large length to width aspect ratios, it was found that the resonant frequencies decreased from 2MHz to 600KHz as the widths of the membrane increased from 90µm to 180µm, but showed no appreciable length dependence. Effective coupling coefficients (k_{eff}^2) was found to increase with width up to 150µm and then decrease. The peak value of k_{eff}^2 was found to be around 0.826%.

The measured resonance frequencies matched quite well with finite element calculations and analytical models. With the inclusion of the residual stress, the 1D composite beam model was found to also yield reasonable prediction for the k_{eff}^2. The finite element code does not have the capability to predict k_{eff}^2 at this point. Based on the prediction of the 2D composite plate model, both the membrane size and electrode coverage have significant influence on k_{eff}^2. The maximum predicted k_{eff}^2 was 2.908% which occurred when the electrode covered about 48.9% in both x and y directions for a square membrane, or about 23.9% of the membrane area covered from the center of the membrane.

8.2 Recommendations

Recommendations are suggested for future work to improve the device performance and the prediction capability using FE model and analytical models. Some of the suggestions can be done by the current facilities with minimal modifications and some other suggestions may require new equipment or major modifications.

8.2.1 Recommendations for Experimental Work

- Pulse-echo test: The possible method to characterize array type pMUTs is an acoustic test such as pulse-echo test using pulser/receiver or hydrophone. An example of pulser/receiver is '5900PR' from OLYMPUS and this test is also called pulse-echo test. An ultrasound transducer or array transducers is activated by pulse signal to generate ultrasound wave and the reflected wave can be detected by the same or different ultrasonic transducer. A schematic view of pulse-echo test setup is shown in Figure 8-1(a). Hydrophone can be used to detect ultrasound wave generated from a transducer as shown in Figure 8-1(b). One possible capsule hydrophone to be used is 'HGL-0200' from Onda Corp.

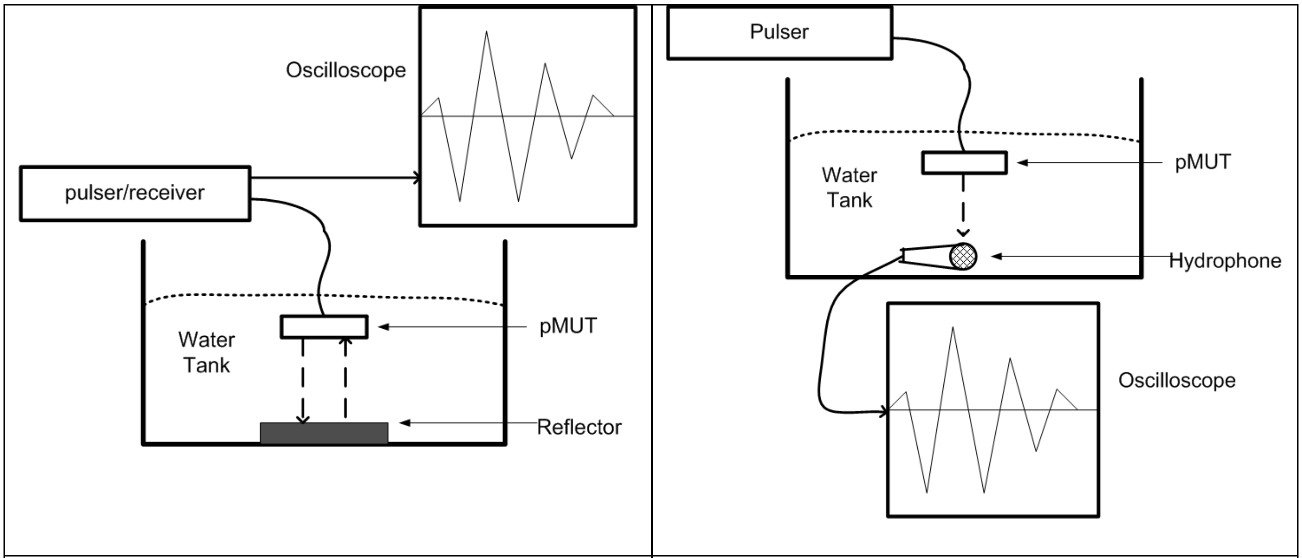

(a): Acoustic test with pulser/receiver.

(b): Acoustic test with hydrophone.

Figure 8-1: Schematic views of acoustic test setups.

- Housing: Prior to the acoustic test, pMUTs should be placed in housing for immersed acoustic test. A schematic view of housing is given in Figure 8-2. Metallic or plastic pipes are the most common housing material and epoxy can be used for backing material. Wear plate is needed in a conventional ultrasound transducers to protect the transducer and to transform acoustic wave from the transducer to the medium. The top electrode will be grounded for the safety of patients and housing will be connected to the top electrode if a metallic housing is used. The bottom electrode is positively charged and the wire comes out through the housing. The acoustic test is in preparation and the details of the work to do will be presented in the Future Work.

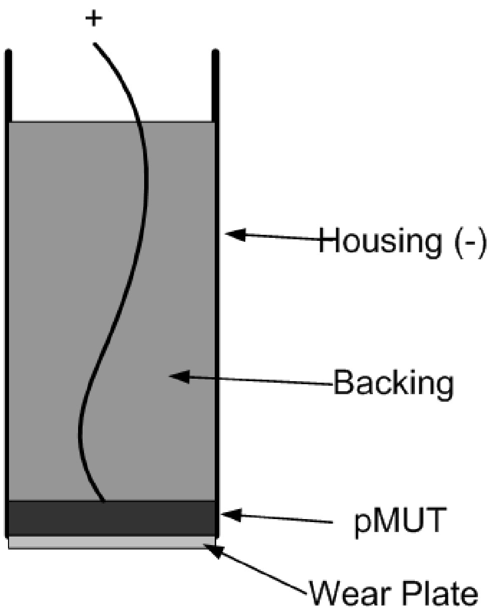

Figure 8-2: Schematic view of transducer housing.

- Control of silicon layer thickness: The thickness of silicon layer is controlled by the boron diffusion time. Since the diffusion of boron on silicon wafer is not perfectly uniform because of the gas flow inside the furnace, the sizes and the thicknesses of the membranes, which were designed to be the same, are not always consistent. It is also not easy to get the membrane thickness as one wants. This problem can be solved if silicon-on-insulator (SOI) wafers are used with deep reactive ion etching (DRIE).
- Compact design: By using SOI wafers with DRIE, the number of pMUTs in a constant area will also be increased. This can also reduce the size of the array or increase the number of elements per unit area.
- Using vacuum packet: All the experimental measurements were done in the air and it is expected that there will be significant damping effect caused by the air.

It is one of the main reasons why the effective coupling coefficient is lower than that from the calculations with the current pMUTs. To overcome the air damping effect, it is suggested to measure the impedance in vacuum and use vacuum packet instead of air packet.

- Size of electrode pad and non-conductive layer between the pad and PZT layers: To apply electric power to the top electrode, connection leads and electrode pads were used and the electrode pads were placed outside of the membrane to avoid breaking the membrane by direct contact. To make possible to contact the electric pad using probe station, the size of the pad should be bigger than certain size (about 200µm by 200µm). For a small membrane, for example 90µm by 860µm membrane and 30µm by 800µm electrode, the size of the pad is much bigger than the electrode size. There is more electrical energy that is lost on the pad and lead than the electrode. To avoid loss of electrical energy, the pad and lead should be much smaller than the electrode or there should a non-conductive layer between the pad and PZT layers.

8.2.2 Recommendations for Modeling Work

- Integration of residual stress in FE model: Residual stress is not used during the FE calculations and it is expected to affect the mechanical behavior of a structure. Quantitative discrepancies between the experimental results and FE calculations could be reduced after integration of residual stress.
- Modeling of electrical part in FE model: Only the mechanical responses of thin film membrane structures are considered in the current FE model. The electrical

response and its coupling with mechanical responses of the structure need to be integrated to make it better tool for pMUTs development.

- Damping effect: Damping effect is not considered in both FE model and analytical solutions. It is expected that there are air damping, material damping, material friction, etc. in pMUTs. To improve the predicative capability of FE model and analytical solutions, damping effect should be considered in the calculations.

References

1. Richard L. Goldberg, Stephen W. Smith, Jack G. Mottley, and K. Whittaker Ferrara. Ultrasound. [book auth.] Joseph D. Bronzino. *The Biomedical Engineering Handbook.* s.l. : CRC Press, 2000, VII.

2. *Ultrasonic transducers and arrays.* K. Kirk Shung, and Michael Zipparo. s.l. : IEEE, 1996, Engineering in medicine and biology, Vol. 15, pp. 20-30.

3. Shung, K. Kirk. *Diagnostic ultrasound.* Boca Raton : CRC Press, 2006. 0824740963.

4. *Quantitative 3-D diagnostic ultrasound imaging using a modified transducer array and an automated image tracking technique.* John A. Hossack, Thilaka S. Sumanaweera, Sandy Napel, and Jun S. Ha. 8, s.l. : IEEE, 2002, Transaction on Ultrasonics, Ferroelectrics, and Frequency Control, Vol. 49, pp. 1029-1038.

5. *3-D ultrasound imaging: A review.* Aaron Fenster, and Donal B. Downey. s.l. : IEEE, 1996, Engineering in medicine and biology, pp. 41-51.

6. *Three-dimensional ultrasound imaging.* Aaron Fenster, Donal B. Downey, and H. Neale Cardinal. s.l. : Institute of physics publishing, 2001, Physics in medicine and biology, Vol. 46, pp. R67-R99.

7. *Real-time three-dimensional echocardiography: An overview.* Panza, Julio A. 2001, The international journal of cardiovascular imaging, Vol. 17, pp. 227-235.

8. Medata. Three-dimensional Ultrasound - The state of the art. [Online] www.medata.cz/Biomedic/Bio_inf.pdf.

9. *Infant cerebral ventricle volume: A comparison of 3-D ultrasound and magnetic resonance imaging.* John H. Gilmore, Guido Gerig, Barbara Specter, H. Cecil Charles, Joseph S.

Wilber, Barbara S. Hertzberg, and Mark A. Kliewer. 8, s.l. : Elsevier, 2001, Ultrasound in Medicine and Biology, Vol. 27, pp. 1143-1146.

10. Medison. [Online] www.medison.com/eng/index.asp.

11. *Fetal weight estimation from lengths and volumes found by three-dimensional ultrasonic measurements.* James F. Brinkley, W. Desmond McCallum, Saundra K. Muramatsu, and Donna Yee Liu. 4, 1984, Journal of ultrasound in medicine, Vol. 3, pp. 163-168.

12. *Progress in two dimensional arrays for real-time volumetric.* Light E D, Davidson R E, Fiering J O, Hruschka P R, and Smith S W. 1998, Ultras Imag , Vol. 20, pp. 1-15.

13. *Two dimensional array for 3D imaging.* Smith SW, Lee W, Light ED, Yen JT, Wolf P, and Idriss S. 2002, IEEE Ultras Symp Proc, pp. 1509-1517.

14. Peter J. Shull, and Bernard R. Tittmann. Ultrasound. [book auth.] Peter J. Shull. *Nondestructive evaluation: Theory, techniques, and applications.* New York : Marcel Dekker, Inc., 2002.

15. center, NDT resource. Transducer modeling. [Online] http://www.ndt-ed.org/EducationResources/CommunityCollege/Ultrasonics/EquipmentTrans/transducermodeling.htm.

16. Ikeda, Takuro. *Fundamentals of Piezoelectricity.* New York : Oxford University press, 1996. 0198563396.

17. Stephen Beeby, Graham Ensell, Michael Kraft, and Neil White. *MEMS mechanical sensors.* London : Artech House, INC., 2004. 1580535364.

18. Lawrence E. Kinsler, Austin R. Frey, Alan B. Coppens, and James V. Sanders. *Fundamentals of acoustics.* New York : John Wiley & Sons, Inc., 2000. 0471847895.

19. Panametria. Technical Notes. [Online] www.panametria.cz/PDF/NDT/transducer_technotes.pdf.

20. *Capacitive micromachined ultrasonic transducers: Theory and Technology.* A. Ergun, G. Yaralioglu, and B. T. Khuri-Yakub. 2003, Journal of Aerospace Engineering, Vol. 16, pp. 76-84.

21. *Surface Micromachined Capacitive Ultrasonic Transducers.* I. Ladabaum, X. Jin, H. T. Soh, A. Atalar, and B. T. Khuri-Yakub. 3, 1998, IEEE Trans. Ultrason., Ferroelect., Freq. Contr., Vol. 45, pp. 678-690.

22. *Micromachined High Frequency Ferroelectric Sonar Transducers.* J. J. Bernstein, Stephen L. Finberg, Kenneth Houston, Lance C. Niles, H. Daniel Chen, L. Eric Cross, Kewen K, Li, and K. Udayakumar. 5, 1997, IEEE Trans. Ultrason., Ferroelect., Freq. Contr., Vol. 44, pp. 960-969.

23. *The constituent equations of piezoelectric heterogeneous bimorphs.* J. G. Smits, and W. Choi,. 3, 1991, IEEE Trans. Ultrason., Ferroelectc., Freq. Contr., Vol. 38, pp. 256-270.

24. *Modeling and optimal design of piezoelectric cantilever microactuators.* D. L. DeVoe, and A. P. Pisano. 3, 1997, Journal of micorelectromechanical systems, Vol. 6, pp. 266-270.

25. *Working equations for piezoelectric actuators and sensors.* Weinberg, M. S. s.l. : 8, 1999, Journal of micorelectromechanical systems, Vol. 4, pp. 529-533.

26. *Piezoelectrically actuated flextensional micromachined ultrasound transducers I: Theory.* G. Percin, and B. T. Khuri-Yakub. 5, 2002, IEEE Trans. Ultrason., Ferroelectc., Freq. Contr., Vol. 49, pp. 573-584.

27. *Plate equations for piezoelectrically actuated flexural mode ultrasound transducers.* Percin, G. 1, 2003, IEEE Trans. Ultrason., Ferroelectc., Freq. Contr., Vol. 50, pp. 81-88.

28. *Optimization of electromechanical coupling for a thin-film PZT membrane: I. Modeling.* J. Cho, M. Anderson, R. Richards, D. Bahr, and C. Richards. 2005, Journal of Micromechanics and Microengineering, Vol. 15, pp. 1797-1803.

29. *Simulation and characterization of piezoelectric micromachined ultrasonic transducers (pMUTs) based on PZT/SOI membranes.* Jacek Baborowski, N.L., Paul Muralt, Daniel Schmitt. 3, s.l. : Imperial College Press, 2003, International Journal of Computational Engineering Science, Vol. 4, pp. 471-475.

30. *Developments of piezoelectric micromachined ultrasonic transducers* . F. Akasheh, T. Myers, J. D. Fraser, S. Bose, and A. Bandyopadhyay. 2004, Sensors and Actuators A, Vol. 111, pp. 275-287.

31. *Piezoelectric micromachined ultrasonic transducers: Modeling the influence of structural parameters on device performance.* F. Akasheh, J. Fraser, S. Bose, and A. Bandyopadhyay. 2005, IEEE Trans. Ultrason., Ferroelectc., Freq. Contr., Vol. 52, pp. 455-468.

32. Prasad, Eswar. AVT-086 COURSE PROGRAM. [Online] [Cited: Feburary 7, 2007.] http://www.ae.metu.edu.tr/~yyaman/avt086/Prasad/Eswar_Prasad_3.pdf.

33. Wilson, Oscar Bryan. *An introduction to the theory and design of sonar transducers.* Monterey : Peninsula Publishing, 1989. 0932146228.

34. Barsoum, Michel W. *Fundamentals of ceramics.* s.l. : McGraw-Hill Companies, 1996. 0070055216.

35. Huber, J. E. *Ferroelectrics: models and applications.* s.l. : University of Cambridge, 1998. Ph. D. Dissertation.

36. KG, Physik Instrumente (PI) GmbH & Co. Fundamentals of Piezoelectricity. [Online] [Cited: Feburary 7, 2007.] http://www.physikinstrumente.com/tutorial/4_15.html.

37. Myers, Todd Benjamin. *Development of PZT driven flexural mode pMUTs.* Master thesis : Washington State University, 2002.

38. *Fabrication and characterization of ferroelectric Pb(ZrxTi1–x)O3 thin films by metalorganic chemical vapor deposition.* Han Sang Song, Tae Song Kim, Chang Eun Kim, and Hyung Jin Jung. 2, s.l. : Materials Research Society, 1999, Journal of Materials Research, Vol. 14, pp. 487-493.

39. *Metalorganic chemical vapor deposition of ferroelectric Pb(Zr,Ti)O3 thin films.* Chien H. Peng, and Seshu B. Desu. 7, 1994, Journal of the American Ceramic Society, Vol. 77, pp. 1799-1812.

40. *Ion-beam deposition of thin films of ferroelectric lead zirconate titanate (PZT).* R. N. Castellano, and L. G. Feinstein. 6, 1979, Journal of Applied Physics, Vol. 50, pp. 4406-4411.

41. *Preparation and properties of ferroelectric PLZT thin films by rf sputtering.* M. Ishida, H. Matsunami, and T. Tanaka. 3, 1977, Journal of Applied Physics, Vol. 48, pp. 951-953.

42. *Piezoelectric thin film devices.* Sayer, M. s.l. : IEEE, 1991. Ultrasonic Symposium. pp. 595-603.

43. *rf planar magnetron sputtering and characterization of ferroelectric Pb(Zr,Ti)O3 films.* S. B. Krupanidhi, N. Maffei, M. Sayer, and K. El-Assal. 11, 1983, Journal of Applied Physics, Vol. 54, pp. 6601-6609.

44. Leclerc, Brian. *Process optimization for Sol-Gel PZT films.* Kingston : Queen's University, 1999. Ph. D. Dissertation.

45. *PZT thin films produced by oxide precursors and crystallized by conventional and RTA process.* E. B. Araujo, and J. A. Eiras. 2001, Journal of the European Ceramic Society, Vol. 21, pp. 1513-1516.

46. *Pulsed laser deposition and ferroelectric characterization of bismuth titanate films.* H. Buhay, S. Sinharoy, W. H. Kasner, and M. H. Francombe. 14, s.l. : American Institute of Physics, 1991, Applied Physics Letters, Vol. 58.

47. Martinez, Julia V. *Fabrication, materials, and characterization for efficient MEMS power generation.* s.l. : Washington State University, 2004. Master thesis.

48. *Sol gel processing of thick PZT films.* Guanghua Yi, and Michael Sayer. Greenville, SC : s.n., 1992. Proceedings of the Eighth IEEE International Symposium on Applications of Ferroelectrics. pp. 289-292.

49. Setter, N. *Piezoelectric Materials in Devices.* Lausanne : EPFL-LC, 2002. 2970034603.

50. Gad-el-Hak, Mohamed. *MEMS: Introduction and fundamentals.* Second. s.l. : CRC Press, 2006. 0849391377.

51. *There's plety of room at the bottom.* Feynman, Richard P. 1, s.l. : IEEE, 1992, Journal of Microelectromechanical systems, Vol. 1.

52. *Infinitesimal machinery.* Feynman, Richard. 1, s.l. : IEEE, 1993, Journal of microelectromechanical systems, Vol. 2, pp. 4-14.

53. *Microelectromechanical systems (MEMS): fabrication, design, and applications.* Judy, Jack W. s.l. : Institute of physics publishing, 2001, Smart materials and structures, Vol. 10, pp. 1115-1134.

54. Hsu, Tai-Ran. *MEMS & microsystmes design and manufacture.* s.l. : McGraw-Hill, 2001. p. 20. 0072393912.

55. Kovacs, Gregory T.A. *Micromachined Transducers sourcebook.* s.l. : McGraw-Hill, 1998. 0072907223.

56. *Silicon as a mechanical material.* Petersen, Kurt E. 5, May 1982, Proceedings of the IEEE, Vol. 70, pp. 420-457.

57. Madou, Marc J. *The MEMS handbook.* [ed.] Mohamed Gad-el-Hak. s.l. : CRC Press, 2002. 0849300770.

58. *Micromachined Ultrasonic Transducers (MUTs).* I. Ladabaum, B. T. Khuri-Yakub, D. Spoliansky, and M. I. Haller. 1995. IEEE Ultrason. Symp. Vol. 1, pp. 501-504.

59. *Coherent-Array imaging using phased subarrays. Part I: basic principles.* Jeremy A. Johnson, Mustafa Karaman, and Butrus T. Khuri-Yakub. 1, s.l. : IEEE, 2005, Transaction on Ultrasonics, Ferroelectrics, and Frequency Control, Vol. 52, pp. 37-49.

60. *Coherent array imaging using phased subarrays. Part II: simulations and experimental results.* Jeremy A. Johnson, Ö mer Oralkan., Sanli Ergun, Utkan Demirci, Mustafa Karaman, Butrus T. Khuri-Yakub. 1, s.l. : IEEE, 2005, Transaction on Ultrasonics, Ferroelectrics, and Frequency Control, Vol. 52, pp. 51-64.

61. *Forward-viewing cMUT arrays for medical imaging.* Utkan Demirci, Arif S. Ergun, Ö mer Oralkan, Mustafa Karaman, and Butrus T. Khuri-Yakub. 7, s.l. : IEEE, 2004, Transaction on Ultrasonics, Ferroelectrics, and Frequency Control, Vol. 51, pp. 886-894.

62. *Volumetric ultrasound imaging using 2D CMUT arrays.* Ö mer Oralkan, Arif S. Ergun, Ching-Hsiang Cheng, Jeremy A. Johnson, Mustafa Karaman, Thomas H. Lee, and Butrus T. Khuri-Yakub. 11, s.l. : IEEE, 2003, Transaction on Ultrasonics, Ferroelectrics, and Frequency Control, Vol. 50, pp. 1581-1594.

63. *Micromachined utrasound transducers with improved coupling factors from a CMOS compatible process.* Peter C. Eccardt, Kurt Niederer. s.l. : Elsevier, 2000, Ultrasonics, Vol. 38, pp. 774-780.

64. *Volumentric ultrasound imaging using 2-D CMUT arrays.* O. Oralkan, A. Sanh Ergun, C-H Cheng, J. A. Johnson, M. Karaman, T. H. Lee, and B. T. Khuri-Yakub. 2003, IEEE Trans. Ultrason., Ferroelectc., Freq. Contr., Vol. 50, pp. 1581-1594.

65. *Piezoelectric actuation of PZT thin-film diaphragms at static and resonant conditions.* P. Muralt, A. Kholkin, M. Kohli, and T. Maeder. 1996, Sensors and Actuators A, Vol. 53, pp. 398-404.

66. *Micromachined ultrasonic transducers and acoustic sensors based on piezoelectric thin films.* P. Muralt, and J. Baborowski. 2004, Journal of electroceramics, Vol. 12, pp. 101-108.

67. *Layered lead zirconate titanate and lanthanum-doped lead zirconate titanate ceramic thin films.* Todd Myers, Parag Banerjee, Susmita Bose, and Amit Bandyopadhyay. s.l. : Materials Research Society, 2002, Journal of Materials Research, Vol. 17, pp. 2379-2385.

68. www.ansys.com. [Online] ANSYS Inc.

69. www.comsol.com. [Online] COMSOL Inc.

70. www.abaqus.com. [Online] ABAQUS Inc.

71. www.intellisensesoftware.com. [Online] IntelliSense Software Corp.

72. www.cfdrc.com. [Online] CFD Research Corp.

73. www.conventor.com. [Online] Coventor Inc.

74. Guangyao Jia, and Marc J. Madou. MEMS Fabrication. [book auth.] Mohamed Gad-el-Hak. *MEMS: Design and Fabrication.* Boca Raton : CRC Press, 2006.

75. Buchanan. *Ceramic Materials for Electronics, Marcel Dekker, Inc., New York, NY, 2004.* s.l. : Marcel Dekker, Inc.

76. *Layered lead zirconate titanate and lanthanum-doped lead zirconate titanate ceramic thin films.* T. Myers, P. Banerjee, S. Bose, and A. Bandyopadhyay. 2002, Journal of Materials Research, Vol. 17, pp. 2379-2385.

77. IEEE. *IEEE Standard on piezoelectricity.* 1988.

78. *On laminated composite plates with integrated sensors and actuators.* Reddy, J. N. 1999, Engineering Structures, Vol. 21, pp. 568-593.

79. Reddy, J. N. *Mechanics of laminated composite plates and shells: Theory and Analysis .* Boca Raton : CRC Press, 2004. 0849315921.

80. *Advances in piezoelectric finite element modeling of adaptive structural elements: a survey.* Benjeddou, A. 2000, Computers and Structures, Vol. 76, pp. 347-363.

81. *A finite-element model for piezoelectric composite laminates.* K. Y. Lam, X. Q. Peng, G. R. Liu, and J. N. Reddy. 1997, Smart Mater. Struct., Vol. 6, pp. 583-591.

82. *The generation of inter-element-compatible stiffness and mass matrices by the use of interpolation formulas.* F. K. Bogner, R. L. Fox, and L. A. Schmit, Jr. 1965. Proceeding of 1st Conference on Matrix Methods in Structural Mechanics. pp. 397-443.

83. *Effect of shear deformation on vibration of antisymmetric angle-ply laminated rectangular plates.* C. W. Bert, and T. L. C. Chen. 1978, International Journal of Solids and Structures, Vol. 14, pp. 465-473.

84. *Free vibration of antisymmetric angle-ply laminated plates including various boundary conditions.* Khdeir, A. A. 1988, Journal of Sound and Vibration, Vol. 122, pp. 377-388.

85. Qatu, M. S. *Vibration of Laminated Shells and Plates.* 2004 : Academic Press. 0080442714.

86. Kennedy, M. S. *Mechanical property determination of thin films for PZT MEMS applications.* s.l. : Washington State University, 2003. Master thesis.

87. *PZT coated membrane structures for micromachined ultrasonic transducers.* J. Baborowski, P. Muralt, N. Ledermann, S. Petitgrand, A. Bosseboeuf, N. Setter, and Ph. Gaucher. s.l. : IEEE, 2002. Proceedings of International Symposium on Application of Ferroelectric. pp. 483-486.

88. *Finite element analysis of piezoelectric thin film membrane structures.* Hongsoo Choi, Jow-Lian Ding, Amit Bandyopadhyay, and Susmita Bose. s.l. : IEEE, 2007, IEEE Trans. Ultrason. Ferroelect. Freq. Contr., Vol. In press.

89. *Influence of top electrode design on pMUTs performance.* Hongsoo Choi, A. Dalakoti, Susmita Bose, and Amit Bandyopadhyay. 2007, Sensors and Actuators A, Vol. 135, pp. 613-619.

90. Goodier, S. P. Timoshenko and J. N. *Theory of Elasticity.* 3rd. New York : McGraw-Hill, 1970. 0070858055.

91. *Theory and analysis of electrode size optimization for capacitive microfabricated ultrasonic transducers.* Ayhan Bozkurt, Igal Ladabaum, Abdullah Atalar, and Butrus T. Khuri-Yakub. s.l. : IEEE, 1999, IEEE Trans. Ultrason. Ferroelect. Freq. Contr., Vol. 46, pp. 1364-1374.

92. *Energy analysis of a piezoelectric body under nonuniform deformation.* Aronov, Boris. s.l. : Acoustical Society of America, 2003, J. Acoust. Soc. Am., Vol. 114, pp. 792-800.

93. *The influence of residual stress on the frequency of ultrasonic transducers with composite membrane structures.* Lee S, Kim J-M, and Shin Y-E. 2006, J. Mech. Sci. & Tech. (KSME Int. J.) , Vol. 20, pp. 76-84.

94. The MathWorks, Inc. *MATLAB help menu on GUI FIG-Files and M-Files.*